Improved Inverse Jiles-Atherton Hysteresis Model for Investigating Controlled Switching of Three-Phase Five-Limb Parallel-Operated HVDC Converter Transformers

By

Chun Fang

A Thesis submitted to the Faculty of Graduate Studies of
The University of Manitoba
in partial fulfillment of the requirements of the degree of
MASTER OF SCIENCE

Department of Electrical and Computer Engineering
Faculty of Engineering
University of Manitoba
Winnipeg, Manitoba

July 2017

Abstract

Ferromagnetic characteristics and magnetic coupling are two crucial aspects when investigating controlled switching transient phenomenon of three-phase five-limb power transformers. Classic Jiles-Atherton (J-A) hysteresis model is popular in engineering applications but model parameters identification remains a difficult undertaking. This thesis explored novel techniques to improve overall accuracy and stability of inverse J-A model. A comprehensive process using a constrained multi-objective particle swarm optimization (PSO) was developed to extract and optimize parameters from published measurements of M3 grade grain-oriented electrical steel. A new methodology was proposed to define a variable that substitutes constant J-A model parameter which substantially improved its precision on minor and major hysteresis loops and magnetization curve simultaneously. This modified model was incorporated into a duality based hybrid transformer model in PSCAD/EMTDC with a computational efficient solution algorithm. Finally, an extensive systematic analysis was conducted to evaluate feasibility and performance of controlled switching three-phase five-limb parallel-operated transformers.

Acknowledgments

To my advisor Dr. Athula Rajapakse, I am truly grateful for your continuous guidance, motivation, inspiration, and encouragement during this project, as well as your invaluable suggestions and advices during my final thesis review and defense. It has been a great privilege to work under your supervision with liberty on research interest direction myself.

I wish to express my sincere gratitude to my co-advisor, Dr. David Jacobson, for your mentorship, commitment, and inspiring discussions that urged my knowledge horizon. Equally, I would like to extend my appreciation to Dr. Udaya Annakkage for sharing your insights and knowledge on variable parameter selection for Jiles-Atherton hysteresis model improvement. I wish to express my appreciation to the Advisory and Examining Committee members for your suggestions and feedbacks on improving my thesis.

I'm deeply indebted to Mr. Pei Wang at System Planning, for your endorsement, valuable guidance and fruitful discussions on controlled switching theories and HVDC control and protection principles throughout my thesis work. I would like to acknowledge and thank Dr. Waruna Chandrasena on sharing perspectives on Jiles-Atherton hysteresis theory.

I am particularly grateful for the mentorship, guidance, support provided by Dr. Rohitha Prashad Jayasinghe from HVDC Research Centre. You have been extremely patient and generous with your expertise and insights on duality based transformer model and other PSCAD/EMTDC related questions. I would also like to recognize and sincerely thank Mr. Juan Carlos Garcia on duality transformer development and helpful discussions.

Certainly, I wish to thank Dr. Dharshana Muthumuni for your endorsement and support on the transformer model initiatives at the beginning of my research endeavor.

I wish to express my sincere thanks to Dr. Hui Ding, Dr. YueFeng Liang, and Dr. Ming Yu at RTDS Technologies on helpful discussions regarding existing three-phase transformer models for electromagnetic transient programs and Jiles-Atherton hysteresis implementation consideration in such environment.

Special recognitions must be made to the administrative staff at the Department of Electrical and Computer Engineering, especially to Ms. Amy Dario, on explaining the academic process and making everything easier for me during the course of my research.

Last but most importantly, to my dear beloved family – this is devoted to all of you.

Chun Fang

July 2017

Dedication

To my dear beloved parents, for raising me, for giving me your unconditional and truly selfless love, for teaching me about care, admiration, fairness, and integrity, for picking me up when I'm down, for encouraging me pursuing any endeavors and adventures, especially this one.

And to my wonderful Vivian, for being a source of continuous supports, countless inspirations, and for all of your love.

Also to my beautiful Chloe, for being a ray of sunshine and a breeze of joy in my life.

Contents

List of Tables

List of Figures

List of Symbols

t	Time (s)
f	Frequency (Hz)
f_0	Power system nominal frequency (50Hz or 60Hz)
Φ	Magnetic flux (Wb)
B	Magnetic induction or magnetic flux density (T or Wb/m^2)
H	Magnetic field strength or magnetic field intensity (A/m)
M	Magnetization (A/m)
M_{rev}	Reversible magnetization (A/m)
M_{irr}	Irreversible magnetization (A/m)
χ	Magnetic susceptibility
μ_0	Permeability constant of vacuum ($4\pi\times10^{-7}$ H/m)
μ_r	Relative permeability
c	Domain flexing parameter
α	Inter-domain coupling parameter
k	Domain pinning parameter
M_s	Saturation magnetization constant (A/m)
M_{an}	Anhysteretic magnetization (A/m)
a_1, a_2, a_3	Annakkage anhysteretic function coefficient
H_e	Effective magnetic field strength (A/m)
B_e	Effective magnetic induction (T)

δ	Directional indicator
δ_M	Conditional parameter
P_{total}	Total ferromagnetic core loss
$P_{hysteretic}$	Static hysteresis core loss
$P_{classical\ eddy}$	Frequency dependent core loss of classic eddy current
$P_{excess\ eddy}$	Frequency dependent core loss of excess eddy current
$H_{dynamic}$	Total magnetic field strength
H_{hyst}	Static hysteresis magnetic field strength
H_{eddy}	Frequency dependent magnetic field strength by classic eddy current
H_{excess}	Frequency dependent magnetic field strength by eddy current
k_1, k_2	Classic and excess eddy current coefficients
k_{eff}	Variable pinning parameter
k_s	Static pinning parameter
pk_1, pk_2	Constants of variable pinning parameter k
v_i^j	PSO particle velocity
v_{max}	PSO particle maximum velocity limit
v_{min}	PSO particle minimum velocity limit
w	PSO inertia weight
w_{start}	PSO inertia weight starting value
w_{end}	PSO inertia weight end value
n	PSO iteration index

c_1, c_2	PSO particle cognitive and social acceleration constants
N_{pop}	PSO total population size
B_{meas}, H_{meas}	Published measurements of magnetic induction and field strength
B_{cal}, H_{cal}	Calculated magnetic induction and field strength by J-A model
$W_{BHcurve}$	B-H Magnetization curve fitness weight contribution factor
W_{HystBH}	B-H Hysteresis loops fitness weight contribution factor
$W_{HystLoss}$	Areas of B-H Hysteresis loops fitness weight contribution factor
V_{LN}	Line to neutral voltage peak magnitude (kV)
i	Current (kA)
N	Number of transformer winding turns
ω	Power system nominal angular speed (rad/s)
L	Inductance
$\Re$	Magnetic reluctance
Δt	Simulation time step
ΔH_{max}	Maximum incremental magnetic strength
Q	Jiles-Atherton iterative numerical solution index
l	Flux path length

List of Abbreviations

AC	**A**lternating **C**urrent
ATP	**A**lternative **T**ransients **P**rogram
CB	**C**ircuit **B**reaker
CS	**C**ontrolled **S**witching
DC	**D**irect **C**urrent
DG	**D**istributed **G**eneration
DR	**D**omain **R**efined
DSM	**D**irect **S**earch **M**ethod
EMT	**E**lectromagnetic **T**ransient
EMTDC	**E**lectromagnetic **T**ransients including **DC**
EMTP	**E**lectromagnetic **T**ransients **P**rogram
FAT	**F**actory **A**cceptance **T**est
FEM	**F**inite **E**lement **M**ethod
GA	**G**enetic **A**lgorithm
GIC	**G**eomagnetic **I**nduced **C**urrent
GOES	**G**rain **O**riented **E**lectrical **S**teel
Hi-B	**H**igh **M**agnetic **I**nduction
HVDC	**H**igh **V**oltage **D**irect **C**urrent
J-A	**J**iles-**A**therton Ferromagnetic Hysteresis Model
KCL	**K**irchhoff's **C**urrent **L**aw

KVL	**K**irchhoff's **V**oltage **L**aw
LCC	**L**ine **C**ommutated **C**onverter
MEEC	**M**agnetic **E**lectric **E**quivalent **C**ircuit
MMF	**M**agneto**m**otive **F**orce
ODEs	**O**rdinary **D**ifferential **E**quations
OLTC	**O**n-**L**oad **T**ap **C**hanger
PIR	**P**re-**I**nsertion **R**esistor
PSCAD	**P**ower **S**ystem **C**omputer **A**ided **D**esign
PSO	**P**article **S**warm **O**ptimization
RMS	**R**oot **M**ean **S**quare
RTDS	**R**eal **T**ime **D**igital **S**imulator
Si-Fe	**S**ilicon **I**ron Alloy (Electrical Steel Alloy)
UMEC	**U**nified **M**agnetic **E**lectrical **C**ircuit
TOV	**T**emporary **O**ver**v**oltage
VG	Converter **V**alve **G**roup
YNd1	W**Y**E **N**eutral-Grounded & **D**ELTA-Lagging 30 Degrees
YNy0	W**Y**E **N**eutral-Grounded & W**Y**E-Ungrounded

List of Appendices

Chapter 1

Introduction

In this chapter, background and detrimental system impacts of inrush current transients due to ferromagnetic core saturation during unloaded transformer energization are recounted, with a special attention to LCC HVDC operations. Conceptual review of conventional inrush current mitigation practices and current state of the art controlled switching technique accounting remanence fluxes is presented. Uncertainties of controlled switching technique on a parallel-operated three-phase five-limb converter transformer pair switched by a single AC circuit breaker are elaborated. For inrush transient studies, proper modelling requirements and challenges of core topology and magnetic characteristics representation of a five-limb transformer are discussed. Following these background discussions and literature reviews, this chapter explains research motivations and objectives, and concludes with an overall thesis organization.

1.1 Background

In a landscape of stringent regulatory requirements, liberation of electricity markets, increasing penetration of distributed generation (DG), and overall customer satisfaction, electric utilities are mandated to design, plan and operate power systems to uphold commitment and compliance with reliability, adequacy, and security in an economically viable manner. Power transformers are a vital and integral part to a reliable continuity of electric energy generation, transmission and distribution, with majority of delivered power moving through them at various stages. Similar to all critical assets, aging power transformers are subject to an increased risk of failure [1]. This imposes great challenges due to substantial capital investment, extensive procurement lead time (in excess of one year or longer for large power transformers), availability of production capability, and transportation difficulty (greater for three-phase units), hence making them a vulnerable component in power grids [1]. Besides aging, operating environment and practice can compromise service life of a power transformer. Loss of a large power transformer can potentially cause long disruption to a large service area outlet, so replacement units or a lifecycle management program should be strategically implemented [2].

Despite being part of regular switching operations, unloaded power transformers energization with improper remedies can generate large harmonic rich inrush current transients. It causes adverse power quality degradation, protection relay misoperation, weakly damped temporary transient overvoltages (TOV) stressing surge arresters and other station equipment, delayed power restoration following a blackout, severe RMS voltage depression, transformer insulation and mechanical cumulative damages [3]. This

phenomenon is especially onerous if occurring near Line Commutated Converter (LCC) HVDC converter stations and is shown to provoke unfavorable valve group commutation failures and substantial power transfer loss [4], [5]

1.2 Inrush Current Transients of Unloaded Transformer Energization

1.2.1 Phenomenon Origin

Power transformer cores are assembled from thin laminations of 3% to 5% silicon infused grain oriented electrical steel (GOES) with a non-linear permeability and history dependent behavior called magnetic hysteresis [6]. Under nominal sinusoidal voltages, transformer core remains linear and highly permeable to flux conduction and produces small non-sinusoidal magnetizing current due to hysteresis. As voltage magnitude increases, core permeability diminishes substantially beyond its saturation state where any subtle flux increase would result in significant rise of magnetizing current alternatively known as inrush current.

When a transformer is disconnected from excitation voltage, the magnetizing current traces hysteresis characteristic to zero and transformer core retains a residual magnetization commonly termed remanence flux or residual flux [6]. As per the constant flux linkage theorem, the magnetic flux in an inductive circuit like a transformer core cannot change suddenly [6]. Therefore, transformer core flux must start from the remanence flux point in a subsequent energization rather than zero or other arbitrary values, which if neglecting

losses could produce a flux up to 3.0 p.u. with a 2.0 p.u. flux asymmetry. Due to core losses, the maximum remanence flux surveyed by CIGRE can reach up to 0.8 p.u. on actual power transformers and generally remains stable after de-energization [5], [7]. This translates into a core flux up to 2.8 p.u. with a 1.8 p.u. flux asymmetry, which can push the transformer core deeply into saturation as illustrated in Figure 1.1.

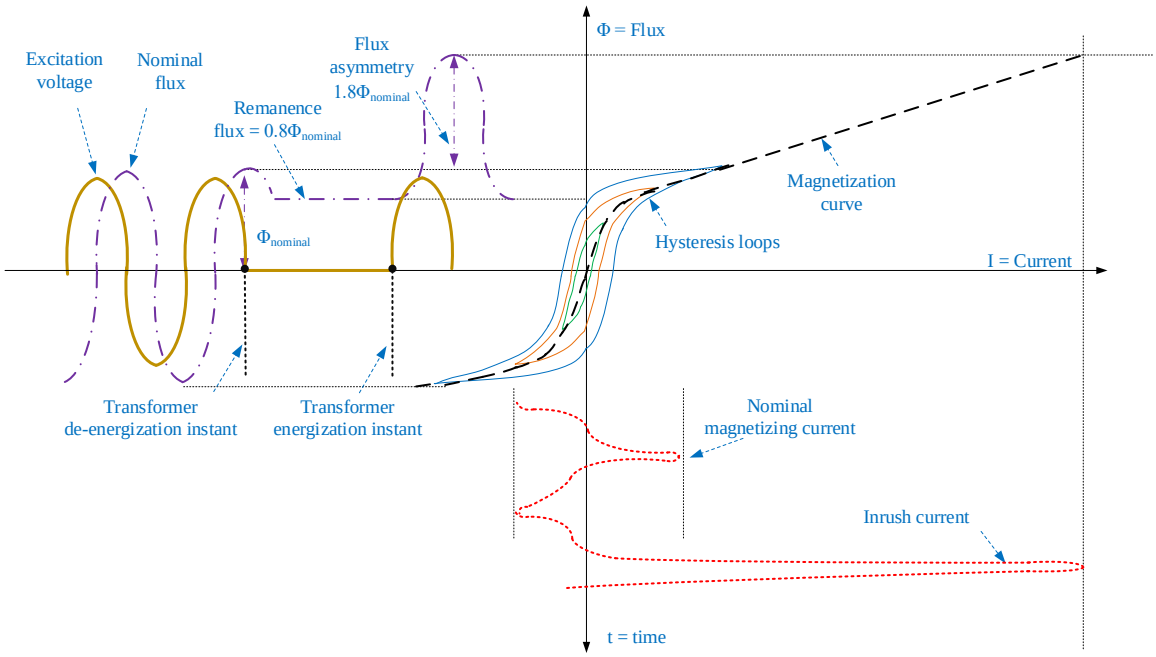

Figure 1.1 Conceptual illustration of flux asymmetry and of inrush current phenomena

Random power transformer energization at instants unfavorable to remanence flux on transformer core could yield large flux asymmetries and saturation of one or more wound cores, which ultimately gives rise to large inrush currents. As part of intrinsic property of ferromagnetic material used in transformer core construction, remanence flux is retained upon de-energization and is influenced by core material characteristics, winding capacitance, breaker current chopping and other capacitances connected [8].

1.2.2 Adverse System Impacts and Interactions

Transformer switchings are normally planned and scheduled operating events. Any energization transients are attenuated predominately by the series impedance of the source power system [5]. When energizing LCC HVDC converter transformers in a weak system with small degree of damping, large inrush currents manifest as severe RMS voltage depression. This can severely distort the bus voltages critical to LCC HVDC commutation process and provoke inadvertent valve group (VG) commutation failures [4], [9]. Unlike voltage sags resulting from fault transients, which can be detected and rectified in cycles, voltage depression due to inrush currents can sustain up to several seconds or longer [5]. In addition, HVDC AC filter banks together with relatively weak network condition can form low frequency parallel resonance that can be excited by inrush current and generate long lasting harmonic resonant temporary overvoltage (TOV) [10]. Exposure to prolonged TOV can cause excessive surge arrester energy dissipation and insulation dielectric stress on other station equipment.

Transformer protective relays could mal-operate by improperly coordinated overcurrent and/or differential elements due to high inrush current transients and inadvertently trip healthy transformer units. Conventionally, these elements are restrained by additional harmonic based elements with a setting of second harmonic to nominal frequency ratio about 0.15 to 0.20 (15 to 20 %) though waveform based (“dwell-time”) restraint algorithms could also be implemented [11]. Both approaches target the asymmetry characteristics of the dominating second harmonic content of inrush currents [11]. However, newer power transformer designs with lower saturation flux and narrower hysteresis loops with a higher remanence level of improved core materials are more

susceptible to a phenomenon called ultra-saturation [12]. This extremely deep saturation renders inrush current free or low of second harmonic and jeopardize security of these conventional restraining algorithms [13].

Part of normal switching operations, inrush currents during power transformer energization could gradually deteriorate mechanical and dielectric integrity of transformer winding coils [14]. Study by three-dimensional (3D) finite element method (FEM) has shown that given large unbalanced excitation inrush currents with longer duration and higher occurrence than short circuit currents can create axial forces always much larger than those obtained by short circuit current [15].

1.2.3 Industry Practices and Remedial Techniques

Conventional mitigations like pre-insertion resistors (PIR) and staggered synchronizing closing on AC circuit breakers have been widely utilized but may offer limited inrush reduction capability [5]. If on-load tap changer (OLTC) is available, it is also capable of inrush current reduction to certain extent [5].

Circuit breakers equipped with optimally selected pre-insertion resistors have been commonly employed in converter transformer energization in LCC HVDC schemes to alleviate RMS voltage depression [9], and to curb harmonic overvoltage issues [10], [16]. However, off-the-shelf modern circuit breakers rated less than 500 kV are no longer available with PIR and special orders of these units for new breakers or replacements are prohibitively expensive [5]. Total maintenance cost during the entire service life span of PIR is another major factor [17]. Retrofitting existing breakers entails extended outages and possibly costly foundation works.

Staggered synchronizing closing technique controls the opening process of circuit breaker poles in a particular sequence. The goal is to establish a consistent disposition of remanence flux pattern in the de-energized transformer core then to issue closing orders to breaker poles accordingly in the subsequent transformer energization switching [5]. During transformer energization, source voltage has a prospect to induce flux on transformer wound cores [8]. The underlying principle of this technique is to minimize any core flux asymmetry by targeting the instants when prospective fluxes are equal to the remanence fluxes [8]. The success of this technique requires stable, repeatable closing characteristics of circuit breakers with independent poles and relatively small pole scatter [5], [7]. Nonetheless, protection initiated tripping would prevail breaker opening operation and render this technique ineffective. Under these circumstances, breakers would be ordered to close at instants that produce zero prospective fluxes. This action would still produce possible up to 1.8 p.u. fluxes and exerts the core deeply into saturation and large inrush currents. For HVDC scheme fed by a weak AC system like New Zealand HVDC links, instead a hybrid scheme of staggered synchronizing closing technique and PIR is installed to assert sufficient inrush regulation [18].

Another practice commonly adopted by utilities is to deliberately re-position OLTC so that the maximum possible winding turns on the energizing voltage side are used. Reference [19] has illustrated analytically that tap position of OLTC can reduce inrush current by lowering the prospective flux peak magnitude. This strategy is viable only if OLTC is installed on the transformer winding to be energized, which is generally true in HVDC applications. OLTC on converter transformers is designed to span over large (up to 50% possible) winding turns in LCC HVDC scheme. But following a protection initiated

AC breaker tripping, transformer core flux asymmetry could still reach an excessive level of 1.8 p.u.

1.2.4 State of The Art: Controlled Switching (CS) Technique with Remanence Flux Consideration

The current state of the art controlled switching technique that is capable of remanence flux estimation and optimal inrush current reduction on unloaded AC power transformers energization has steadily gained attention and endorsement by breaker manufacturers and utilities [7]. Transformer core remanence fluxes are estimated during de-energization at all times, either normal or protection tripping, and used to predict optimal closing instants in the subsequent energization [8]. These optimal closing instants are calculated by ensuring the prospective fluxes are equal to the remanence fluxes on transformer wound cores [8]. However, this technique is feasible on three-phase transformers with a three-limb core or with a delta winding connection, which ensures a phenomenon known as core flux equalization and fluxes of main wound limbs summing to zero [8]. Breaker characteristics and other factors can be taken into account by effective compensation algorithms [7].

1.3 Quest on Controlled Switching Five-Limb Parallel-operated HVDC Converter Transformers

Theory of controlled switching strategies accounting for remanence flux has been proven effective on energization of single unloaded power transformer with a three-limb core or with a delta winding connection [20], [21], [22], [23], [24]. However, uncertainties

still remain unsettled on a 12-pulse HVDC converter transformer pair with a five-limb core owing to insufficient works published on this application. For a comprehensive analysis, a proper transformer model must be considered in electromagnetic transient (EMT) programs. Accurately representations of a topologically correct core capturing magnetic couplings and overall ferromagnetic characteristics of GOES for core assembly in both unsaturated and heavily saturated regions are equally crucial.

Analysis of controlled switching parallel-operated converter transformer pair without considering the magnetic coupling effect between branches of five-limb cores would be flawed. A comparative investigation on three-phase transformers modeling with and without magnetic coupling between phases have confirmed the importance of magnetic coupling, and demonstrated that large errors would be introduced without it [25]. But there are only limited number of three-phase transformer models with suitable core topology and ferromagnetic hysteresis representation that are available for such studies in EMT programs [26]. For hysteresis representation, parameter identification of the popular Jiles-Atherton (J-A) model has remained a discouraging challenge, which is further complicated by inconsistent model equations often reported in the literatures.

1.3.1 Ferromagnetic Hysteresis Models

Hysteresis has been acknowledged as an intrinsic physical attribute of ferromagnetic materials and an accurate mathematical representation of its magnetic behaviors has long been contested in low to mid-frequency phenomenon, such as inrush current analysis [20], [27], [28], ferroresonance condition [29], [30], and geomagnetically induced current (GIC) study [31], where saturation and hysteresis have a profound effect.

1.3.2 Classic Ferromagnetic Hysteresis Models

In general, modeling approaches to magnetic hysteresis are classified as curve fitting model, physical based model, and macroscopic mathematical model [32]. Considerable progress in understanding and modelling of ferromagnetic hysteresis has been accomplished in the past decades. Of various magnetic hysteresis models proposed and published, many of these efforts are based on curve fitting which ignore the underlying physics [32]. Other energy based micromagnetic methods are computationally prohibitive and impractical, but only a few, as discussed in [32], truly capture the underlying physical mechanisms relating microstructures and macroscopic properties. Besides Rayleigh Loop, Chan-Vladirimescu model and Hodgdon model, four magnetization hysteresis models of Stoner–Wolhfarth model, the Globus model, Preisach model, and Jiles-Atherton (J-A) model are now considered classic, of which a bibliographical review is given in [33] by Leon and Semlyen.

Among various magnetic hysteresis models, J-A hysteresis model has been regarded the most suitable and practical in engineering applications and in time domain simulation programs. It is recognized for a proven validity in depicting ferromagnetic materials, remanence retention, physically significant parameters that can be identified and optimized using quasi-static hysteresis measurements [33]. Also, consideration of energy dissipation from the magnetic domain wall displacement and ability to incorporate frequency dependent losses, along with a favorable computational efficiency as summarized in Table 1.1 outshine other classic models [33].

Table 1.1 Classic hysteresis models overview

Model / Characteristics	Stoner-Wolhfarth extended	Globus modified	Preisach	Jiles-Atherton
Mechanism	Rotation	Wall motion	Not specified	Not specified
Anisotropy	Uniaxial	Multi-axis	Not specified	Multi-axis
Interaction	Yes	No	Moving model	Yes
Pinning	Yes	Yes	Not specified	Yes
Texture	Anisotropic or isotropic	Uniaxial (180° walls)	Not Specified	Isotropic
Wall energy	No	Yes	No	No
Reversibility	Yes	Yes	Additional model	Additional model
Minor Loops	Yes	- (N/A)	Yes	Approximation
Demagnetization	- (N/A)	- (N/A)	Yes	Yes
Anhysteretic	Yes	Yes	Yes	Yes
Parameters (Measurable Parameters *)	M_s* k_u* $\bar{\eta}*$ σ α p	M_s* $\gamma*$ $R*$ $f*$	M_s* $\bar{h}c$ σ_i σ_c α	M_s* $c*$ $a*$ $\alpha*$ $k*$
Grains	Single domain	Bi-domain	Not specified	Multi-domain
Computational time (fewer "+" better)	+++	+	++++	++
Materials	Hard magnetic materials	Soft ferrites	-magnetic recording - thin films	-Bulk materials - medium ferrites

Note: (N/A) Not Available

1.3.3 Classic J-A Hysteresis Model in Engineering Applications

J-A theory of ferromagnetism, a macroscopic concept introduced in Jiles and Atherton's landmark papers [34], [35], has been previously implemented in many engineering applications to correctly predict the hysteretic characteristics of ferromagnetic materials when subjected to external excitations. In [36], a good agreement was obtained between calculated quasi-static (rate-independent) and dynamic (rate-dependent) major hysteresis loops and measurement of non-oriented silicon iron using classic J-A model and its generalized form. Reference [37] illustrated that a modified J-A model accurately predicts both major and minor hysteresis loops in the rolling and transverse directions of GOES laminations. GOES is a ferromagnetically soft material commonly used in the construction of power transformer core and electric machines. Other publications have applied this model for the magnetic core behavior of a three-phase three-limb power transformer [27] and single-phase power transformers [20], [38] and successfully validated simulated inrush currents against measurements.

1.3.4 Key J-A Model Formulation Variances in Literatures

One of the key formulas in J-A hysteresis mathematical system is the expression of differential susceptibility, which can be manipulated and incorporated in EMT environment with a discrete time solution. As reviewed in [39], the first such expression has been introduced by original authors D. C. Jiles and D. L. Atherton in [35] but a slight altered form has then appeared in their landmark papers [40], [41]. Several other variances of the differential susceptibility have been published in many literatures, for instances [42],

[43], [44], [45]. Such inconsistencies have resulted in great misinterpretations and confusions.

1.3.5 Existing J-A Model Parameters Identification Techniques

Jiles and Atherton proposed an estimation method relying on measured incremental susceptibilities at several characteristic points on the $M - H$ plane and developed a series of nonlinear equations iteratively solved to recover values of model parameters, but this approach suffered from some major drawbacks that render it less effective [39].

Alternatively, an increasing number of artificial intelligence methods have gained popularity in literature. These approaches explore the notion that transforms the number of model parameters into corresponding level of dimensions in search space and evaluates the agreement of calculated and measured quantities by properly conceived fitness functions [39]. A comparative investigation has demonstrated that PSO is well capable of identifying J-A model parameters for both non-oriented and oriented electrical steels and is superior in performance than other intelligent techniques such as genetic algorithm (GA) and direct search method (DSM) [45].

Behavior of hysteresis loops at different exerting field and magnetization curve are important for an overall accurate representation of a ferromagnetic core characteristics. Extensive literature reviews conclude that majority of model parameters are identified based on a single hysteresis loop and repeatedly excluded magnetization curve characteristics.

1.3.6 Bibliographic Survey of EMT Transformer Models

Representations of winding connections and ferromagnetic core behaviors are two aspects essential to a low- and mid-frequency three-phase power transformer model in electromagnetic transient simulations [26]. Based on winding electrical interfaces and transformer core representation philosophies, these transformer models can be mainly categorized as terminal, topological and hybrid approaches [46]. A comprehensive bibliographic review of these approaches is given by references [26], [46], [47].

Mathematical models of both self and mutual inductance matrixes, for instance the classical single-phase multiple-winding components in PSCAD/EMTDC and BCTRAN model in EMTP programs, are good example of terminal based approach [47]. However, these models fail to adequately describe the magnetic coupling, magnetic hysteresis and core losses and instead use piece-wise single-valued nonlinear saturation characteristic.

In comparison, topological approaches are created on geometry and topology of the transformer core either by directly embedding its companion magnetic circuits into a connection admittance matrix through a multi-port Norton equivalent like UMEC model in PSCAD/EMTDC, or by replacing its magnetic circuits with a dual electric equivalent like Dual model in EMTP-ATP [26], [46], [47]. Existing UMEC model with single-valued saturation characteristic is released in PSCAD [48]. Reference [49] has successfully incorporated and validated frequency-dependent J-A hysteresis model in single UMEC transformer model, but extension of such technique to a three-phase five-limb model is not currently available.

On the contrary, duality based topological method originated from Colin Cherry's principle of deducing an equivalent electric circuit for its companion magnetic circuit using

analogous relations and constituting laws in these two domains [46], [47], [50]. It is demonstrated that the J-A hysteresis can be directly incorporated in the duality based three-phase transformer with three-limb or five-limb cores [26]. This approach is theorized on classical hypothesis that transformer core can be discretized into lumped saturable magnetic reluctances, linear leakage, and air flux inductances but is limited to a maximum of three windings [50].

Lastly, the Hybrid approaches consolidate the strengths of mathematical leakage inductance matrix and topologically correct core models where the two are connected by a fictitious thin winding [51], [52]. The leakage inductance matrix describes winding connections, and duality principle derived core model represents magnetic interaction and permits both singled-valued piece-wise nonlinear saturation and easy incorporation of hysteresis [26]. The TOPMAG in EMTP-RV, HYBRID in EMTP-ATP, and MEEC component in PSCAD are variant examples of this modelling philosophy.

1.4 Motivation and Objectives

Controlled switching technique that takes into account power transformers remanence fluxes has been steadily gaining attention in power industry as an effective and economic inrush mitigation method. Related studies and applications on single-phase transformers, three-phase units with three-limb cores or with delta winding connections have been extensively investigated and published [7]. However, systematic analysis regarding the feasibility and performance of this technique on parallel-operated three-phase five-limb converter transformers with practical considerations has not been published at the time of this research work. For 12-pulase converter transformers with YNy0 and YNd1 vector

configurations, a single delta winding is shared by two five-limb core transformers and is presented on the valve side. To investigate this issue, only a few transformer models are available in EMT programs capable of accurate representation of core interaction and hysteresis behaviors. Also, the J-A hysteresis model used to describe the ferromagnetic hysteresis has shown uncertainties in some of its key mathematical formulations and has deterred general users with model parameter identifications.

With the above discussion, the following specific objectives are defined:

1. Review and investigation of static Jiles-Atherton ferromagnetic hysteresis model mathematical system that no frequency-dependency is considered. Accordingly, illustrative derivation of the correct key model expressions with an alternative inverse form that can be more readily incorporated into EMT environment.
2. Development of a new process that can facilitate identification and optimization of J-A model parameters using published measurements of a collection of static hysteresis loops and magnetization curve simultaneously.
3. Validation of J-A model calculation against the published measurements and implementation of model modifications for improved overall agreements.
4. Identification of frequency-dependent eddy current parameters and extension of the static J-A model to the dynamic one including such frequency-dependence.
5. Incorporation of dynamic J-A model in EMT program with a more computational efficient solution algorithm.
6. Development of a representative controlled switching controller capable of several control strategies in EMT program.

7. Feasibility and performance evaluation of controlled switching energization of parallel-operated five-limb converter transformers using systematic analysis with practical considerations for a LCC HVDC system.

1.5 Thesis Overview

This introduction chapter provides pertinent background and literature review and defines the motivation and key objectives of this research. The remaining discussions of this thesis are presented and organized by the following structure.

Chapter 2 reviews the magnetization process in ferromagnetic materials and J-A theory before embarking onto the illustrative derivation of an inversely formulated static J-A model formulations. Frequency-dependent core losses due to eddy currents is then added to the static J-A model using the loss separation principle.

In Chapter 3, a novel identification process has been proposed for J-A model parameters based on a constrained multi-objective Particle Swarm Optimization (PSO) technique. Published measurements of static hysteresis loops and magnetization curve of a M3 grade domain remained (DR) grain oriented electrical steel (GOES) are considered for validation purpose. Limitation of classic J-A model that fails to accurately describe magnetic characteristics on both minor and major loops is revealed. A new methodology based on the proposed PSO technique is developed to simultaneously improve precision of classic J-A model calculations on hysteresis loops and magnetization curve.

In chapter 4, the modified inverse J-A model with frequency-dependence has been incorporated into a three-phase five-limb duality based hybrid model in PSCAD/EMTDC. The calculated hysteresis loops in PSCAD has been validated against measured quantities

at 50 Hz. A new computational efficient numerical solution algorithm has been developed for the modified J-A model. The underlying principle of controlled switching technique of unloaded power transformers has been illustrated relied on which a controller model has been developed in PSCAD.

In chapter 5, an extensive systematic analysis of three-phase five-limb parallel-operated converter transformer pair energization at different opening and closing instants has been evaluated with and without mitigations. Feasibility of controlled switching in such application and interaction of the single delta winding connection and five-limb transformer core during the controlled switching process have been investigated. Performance of controlled switching technique with remanence flux estimation has been compared against that of a typical off-the-shelf breaker pre-insertion resistor using three-dimensional illustrations and statistical analysis. Impacts of breaker pole scatter and HVDC converter transformer OLTC operation under normal and protection initiated scenarios have been investigated.

Finally, chapter 6 presents major conclusions, a summary of main contributions and suggestions for future research.

Chapter 2

Inverse J-A Magnetization Model for Ferromagnetic Hysteresis

2.1 Introduction

In this chapter, derivation of an inversely formulated Jiles-Atherton (J-A) model, expressed as a function with respect to the variation of magnetic induction B, is illustrated. This exercise is primarily intended to reconcile inconsistencies often seen in J-A model formulations published in literature. The concept of core loss separation for incorporating the classical and anomalous or excess eddy current losses is then discussed to generalise J-A hysteresis with frequency dependent description. It is essential to appreciate the underlying physical theory that associates microscopic magnetic structures, macroscopic behavior, and related mathematical representation. Before embarking on the mathematical system of J-A model, a quick review is devoted to magnetization process and J-A hysteresis theory at the onset of this chapter.

2.2 J-A Theory of Ferromagnetic Hysteresis

2.2.1 Description of Magnetization Process

In a ferromagnetic material, a phenomenon that magnetization retraces different paths when being exerted by an external alternating magnetic field is denoted hysteresis [34]. It is attributed to the presence of magnetic domains that are atomic structures composed of several internal magnetic fields situated in the same direction, and confined by transition boundaries known as domain walls as visualized in Figure 2.1 [53].

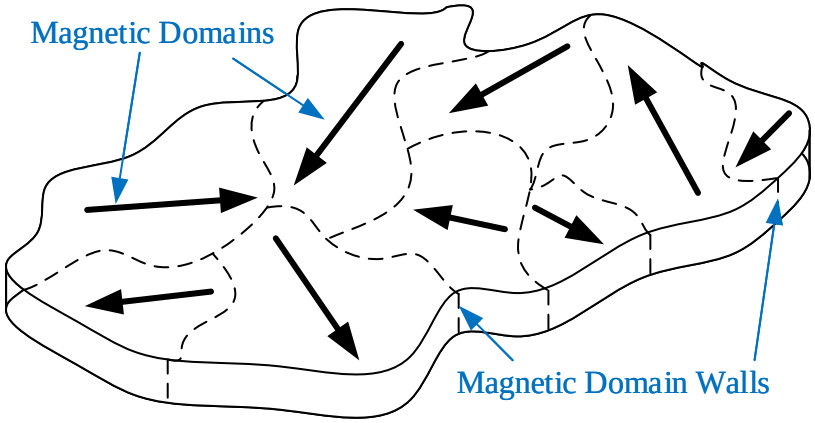

Figure 2.1 Magnetic domains and magnetic walls visualization

For ferromagnetic materials, the existence of internal magnetic fields originates from magnetic moments created by spinning of unpaired electrons and persists even upon removal an external magnetic field [53]. In paramagnetic materials, unpaired electrons react in response to external magnetic fields but their alignments become defused due to thermal energy randomization, for which reason its magnetization cannot be retained in the absence of external magnetic field [53]. On the contrary, diamagnetic substances

encompass only paired electrons with a net spin of zero, so they are inactive to the attraction of externally applied magnetic field [53].

A complete magnetization cycle evolves the following states [35], [54], [55]:

1. Starting from a completely demagnetized state, magnetic domains in ferromagnetic materials are randomly oriented and the net average magnetization is zero.
2. When externally exposed to an increasing magnetic field, domains progressively align in the direction of field influence where favorably oriented domains expand at the sacrifice of poorly inclined neighbor domains. The growth of domains at low magnetic field is associated with reversible elastic motions of domain wall pinned by defect and impurity sites within the material. But as the field becomes sufficiently strong this behavior is resulted from irreversible displacements of domain walls to new pinning sites. A visualization of both reversible and irreversible magnetic domain wall movements is depicted in Figure 2.2 [35].

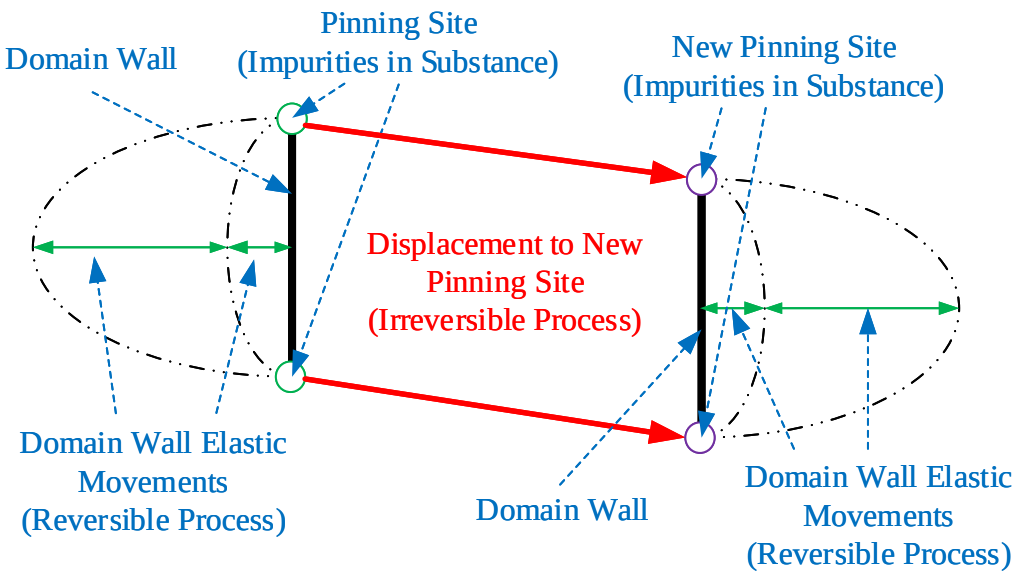

Figure 2.2 Reversible and irreversible domain wall motions visualization

3. If applied field keeps increasing, eventually one single domain emerges as all smaller domains unanimously rearranged with crystallographic easy axis direction closest to the external field. Now material is technically magnetically saturated
4. As the field increases even further, magnetic domain moment rotates and become in parallel to the external field which is a reversible process. Beyond this state, magnetic induction B rises disproportionally to any sublet increase of magnetic field intensity H.
5. Upon a decrease of field strength H, magnetic domain moment reverses it rotation and its axis again becomes inclined to direction of applied field.
6. When the field diminishes to zero, alignment of magnetic domains is disrupted and a considerable level of magnetization is retained. This phenomenon is designated as remanence flux, or otherwise known as residual flux.
7. As the applied field reverses its direction, material is again split up into magnetic domains with different orientations. If the field keeps increasing in the reverse direction, domains gradually and eventually surrender to other domains until reaching an equilibrium state of zero total average magnetization. The magnetic field required here is called coercive field – an intrinsic property used to distinguish the “soft” and “hard” ferromagnetic materials.

Figure 2.3 illustrates a complete evolution of magnetization process beginning in a demagnetized state, moving into saturation and back to a zero-magnetization state [54].

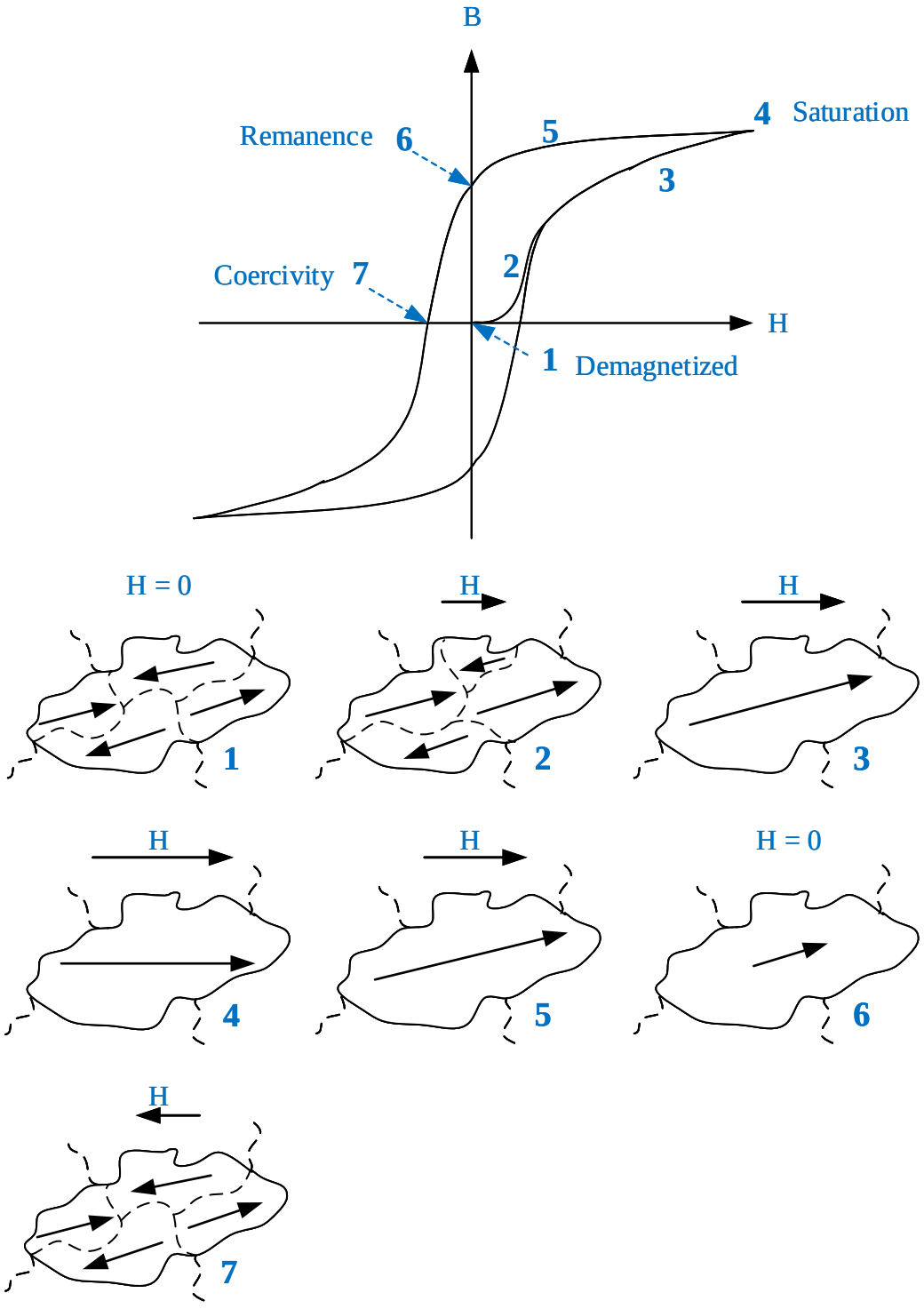

Figure 2.3 Magnetization process and magnetic domain evolution

In terms of energy conservation, magnetization process can be perceived as energy transfer from the external magnetic field to internal magnetic domains where a portion of transferred energy is stored and recovered during reversible process but the remaining is dissipated through irreversible process by domain wall displacements [35].

2.2.2 Jiles-Atherton Hysteresis Theory

The Jiles-Atherton theory, originally postulated in [34] and further explained in [35], enables simple macroscopic formulations to quantitatively describe the microscopic physical phenomena of ferromagnetic materials, without undue knowledge of spatial distribution of domains. The concepts of reversible and irreversible magnetization based on magnetic domain walls motions were proposed. Exposition of interaction between magnetic field H and domain magnetization M by a mean field was given [35]. Irreversible magnetization process refers to energy required to overcome pinning effects [35]. Therefore, in a perfect material free of imperfection, a single-valued ideal magnetization curve called anhysteretic magnetization M_{an}, would occur and describe a completely reversible M-H relationship at a global equilibrium of lowest-energy state in this theory [56].

One of the fundamental hypothesis of J-A theory is the decomposition of magnetization into reversible M_{rev} and irreversible M_{irr} components as illustrated in Figure 2.4, representing flexible domain wall bending action and displacements respectively [56] [57]. On the ascending part of hysteresis loop, magnetization M is weaker than anhysteretic magnetization M_{an} so magnetic domain walls experience a force that tends to increase M;

whereas on the descending part M is greater than M_{an} and domain walls experience a force that tends to reduce M [35].

A series of ordinary differential equations (ODEs) that constitute differential magnetic susceptibility, reversible and irreversible susceptibilities, and an arbitrary anhysteretic magnetization function were derived to characterize hysteresis loops [35].

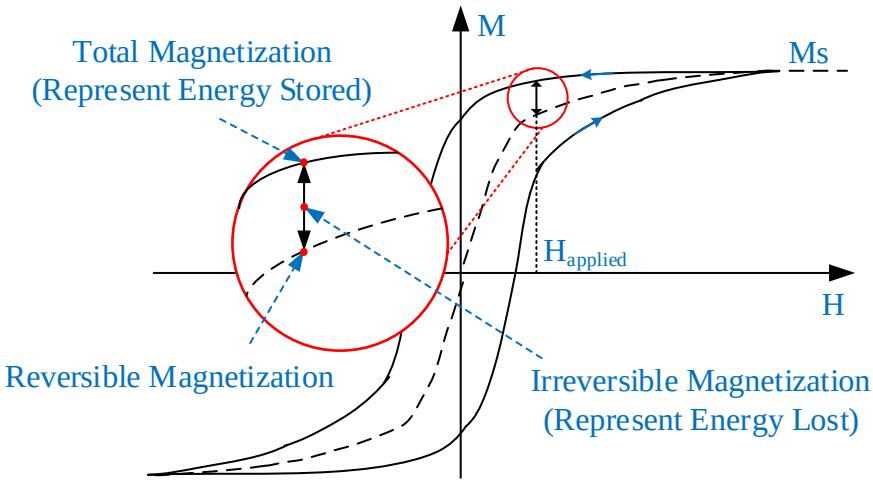

(a) Magnetization M - Magnetic Field Strength H Plane

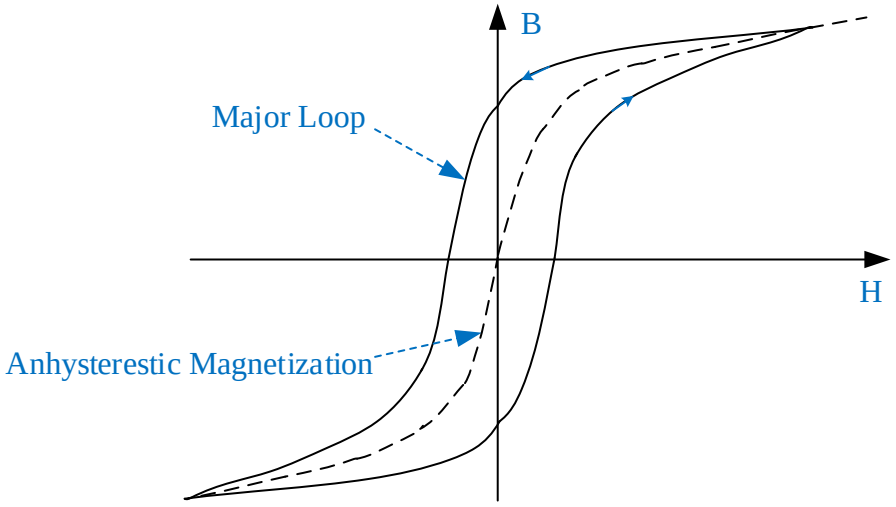

(b) Magnetic Induction B - Magnetic Field Strength H Plane

Figure 2.4 J-A Theory: reversible, irreversible and anhysteretic magnetizations

2.2.3 Mathematical System and Inverse J-A Model

In a ferromagnetic material, magnetization M relates to magnetic field strength H by

$$M = \chi \mathrm{H} \tag{2.1}$$

where χ is the susceptibility, an intrinsic physical property which specifies the degree of magnetization reaction to an applied magnetic field.

The magnetic induction B, also known as magnetic field density, can be expressed by H and M in forms of

$$\begin{aligned} B &= \mu_0(H + M) \\ &= \mu_0(1 + \chi)H \\ &= \mu_0\mu_r H \\ &= \mu H \end{aligned} \tag{2.2}$$

with μ_0 the magnetic permeability constant of vacuum ($4\pi\times10^{-7} H/m$),

μ_r the relative magnetic permeability of a material with respect to μ_0,

μ the magnetic permeability, respectively.

In general, most materials possess permeability close to μ_0, but in the case of ferromagnetic materials, like iron and its silicon-iron (Si-Fe) alloys, these values greatly surpass[1] μ_0 and exhibit nonlinearity and hysteresis [55]. Large power transformer cores are prevalently constructed from thin laminations of Si-Fe steel, typically about 3% silicon composition, to produce higher magnetic flux per winding turn thus a higher induced voltage per turn with a relatively small field increase in the desired unsaturated region [6].

[1] When observed below the Curie temperature of a given ferromagnetic material; otherwise the material undergoes structure disorientation and significantly alters its magnetic properties [21].

Silicon is a substance mixed in the alloy to raise resistivity as a mean to curb eddy current losses and to maintain material stability as it ages during its service life span [6].

According to the classic J-A theory [35], average magnetization in a ferromagnetic material is essentially comprised of reversible and irreversible components, namely M_{rev} and M_{irr}, and is given by

$$M = M_{rev} + M_{irr} \tag{2.3}$$

M_{rev} is related to the global equilibrium state of anhysteretic magnetization M_{an} by domain flexing parameter c, which ranges from 0 to 1 depending on the reversibility of magnetic domain wall motions in the ferromagnetic material [41].

$$M_{rev} = c(M_{an} - M_{irr}) \tag{2.4}$$

Analogous to the Weiss mean field concept, effective magnetic field H_e has been adopted in J-A theory and is written as

$$H_e = H + \alpha M \tag{2.5}$$

where α signifies the inter-domain coupling interaction based on average mean field hypothesis and is determined experimentally [34], [41].

The classic J-A model formulation has evolved since its original debut to reflect more physical behaviors, but various key mathematical expressions published over the years revealed inconsistencies and thus caused misinterpretations. With a close examination, references [58] and [59] concluded this uncertainty can be attributed to the expression for H_e given in Equation (2.6), which was used interchangeably with Equation (2.5) by some authors with no clear explanation or justification.

$$H_e = H + \alpha M_{irr} \tag{2.6}$$

In this thesis, the correct expression for effective magnetic field in accordance with J-A theory, given in Equation (2.5), is considered this onward [59]. When modeling a power transformer in an EMT environment, it is beneficial to express J-A model formulas with respect to magnetic induction B - a quantity readily calculated by transformer winding voltages in time domain simulations. For this reason, derivation of an inverse J-A model formulation continues below.

Substituting M_{rev} in (2.3) by (2.4), M is expressed by

$$M = (1 - c)M_{irr} + cM_{an} \tag{2.7}$$

and M_{irr} is then written as

$$M_{irr} = \frac{M - cM_{an}}{1 - c} \tag{2.8}$$

In the original J-A model, $M_{an}$was described by a modified Langevin function, but in present work alternative expressions in (2.9) and (2.10) has been adopted. It offers higher degrees of freedom and accuracy in defining the overall curve shape [43]

$$M_{an} = M_s \cdot \frac{a_1 \cdot H_e + {H_e}^b}{a_3 + a_2 \cdot H_e + {H_e}^b} \tag{2.9}$$

complemented by a derivative form with respect to H_e by

$$\frac{dM_{an}}{dH_e} = M_s \cdot \frac{a_1 \cdot a_3 + b \cdot a_3 \cdot {H_e}^{(b-1)} + (b-1) \cdot (a_2 - a_1) \cdot {H_e}^b}{(a_3 + a_2 \cdot H_e + {H_e}^b)^2} \tag{2.10}$$

where coefficient M_s denotes the saturation magnetization, an intrinsic property of a given magnetic material, and coefficients $a_1,\ a_2,\ a_3$, and b determines the shape of anhysteretic function and must satisfy$a_2 > a_1 > 0,\ a_3 > 0$, and $b^2 \geq 1.0$.

Differentiating (2.7) with respect to effective magnetic induction B_e

$$\begin{aligned} \frac{dM}{dB_e} &= \frac{dM}{dB}\frac{dB}{dB_e} \\ &= (1-c)\frac{dM_{irr}}{dB_e} + c\frac{dM_{an}}{dB_e} \end{aligned} \tag{2.11}$$

where effective magnetic induction B_e is defined by [60]

$$\begin{aligned} B_e &= \mu_0 H_e \\ &= \mu_0(H + \alpha M) \\ &= B + \mu_0(\alpha - 1)M \end{aligned} \tag{2.12}$$

and derivative of magnetic induction with respect effective magnetic induction $dB/(dB_e)$ is given by

$$\frac{dB}{dB_e} = 1 + \mu_0(1-\alpha)\frac{dM}{dB_e} \tag{2.13}$$

Now substitute (2.13) into the first equal expression on the right-hand side of (2.11) and expand

$$\frac{dM}{dB_e} = \frac{dM}{dB}\left(1 + \mu_0(1-\alpha)\frac{dM}{dB_e}\right) \tag{2.14}$$

[2] In this work, $b = 2$ is considered [43]

then factorize term dM/dB_e and simplify

$$\frac{dM}{dB_e} = \frac{\frac{dM}{dB}}{1 - \mu_0(1-\alpha)\frac{dM}{dB}} \tag{2.15}$$

Regarding the second equal expression on the right-hand side of (2.11), irreversible magnetization susceptibility is defined in [41] as

$$\frac{dM_{irr}}{dH_e} = \frac{M_{an} - M_{irr}}{\frac{k\delta}{\mu_0}} \tag{2.16}$$

where δ is a directional parameter indicating increasing and decreasing magnetic fields and is determined by [56]

$$\delta = \begin{cases} 1 & if\ \frac{dH}{dt} > 0\ (increasing\ field) \\ -1 & if\ \frac{dH}{dt} < 0\ (decreasing\ field) \end{cases} \tag{2.17}$$

In the EMT time domain simulation environment, δ is calculated by the derivative of magnetic intensity H or magnetic induction B with respect to simulation time step Δt.

Substitute the derivative term in (2.16) using relationship in (2.12) and yield

$$\begin{aligned} \frac{dM_{irr}}{dB_e} &= \frac{dM_{irr}}{dH_e}\frac{dH_e}{dB_e} \\ &= \frac{M_{an} - M_{irr}}{k\delta} \end{aligned} \tag{2.18}$$

then replace M_{irr} by (2.8) and express dM_{irr}/dB_e by (2.18)

$$\frac{dM_{irr}}{dB_e} = \frac{M_{an} - \dfrac{M - cM_{an}}{1-c}}{k\delta} \tag{2.19}$$

The remaining term dM_{an}/dB_e in (2.11) is related to (2.10) by

$$\frac{dM_{an}}{dB_e} = \frac{dM_{an}}{dH_e}\frac{1}{\mu_0} \tag{2.20}$$

Now substitute equations (2.15), (2.19), and (2.20) into (2.11) for terms dM/dB_e , dM_{irr}/dB_e and dM_{an}/dB_e respectively, and manipulate

$$\begin{aligned}\frac{dM}{dB_e} &= \frac{\dfrac{dM}{dB}}{1-\mu_0(1-\alpha)\dfrac{dM}{dB}} \\ &= (1-c)\frac{M_{an} - \dfrac{M - cM_{an}}{1-c}}{k\delta} + c\frac{dM_{an}}{dH_e}\frac{1}{\mu_0}\end{aligned} \tag{2.21}$$

Finally equate the two expressions in (2.21) and factorize term dM/dB

$$\frac{dM}{dB} = \frac{\dfrac{(M_{an}-M)}{k\delta} + \dfrac{c}{\mu_0}\dfrac{dM_{an}}{dH_e}}{1+\mu_0(1-\alpha)\left(\dfrac{(M_{an}-M)}{k\delta} + \dfrac{c}{\mu_0}\dfrac{dM_{an}}{dH_e}\right)} \tag{2.22}$$

Unlike the differential susceptibility dM/dH postulated in the originally J-A model this inverse differential relationship of M and B induction can be directly incorporated in power transformer models in EMT programs where flux and flux density values are readily calculated from winding voltages . The original J-A model may still be favored in current transformer models, with either a ferromagnetic core or ferrite core material, where magnetic field quantities are more directly accessible. Inverse J-A formulation is deemed

an alternative expression, and model parameters along with their identification processes remain valid for both inverse and original direct models [60].

Original J-A model is prone to produce non-physical negative differential susceptibility dM/dH values, especially near the tip reversal points when the total magnetization crosses the anhysteretic magnetization on the ascending part and conversely in the descending portion [43]. Under these conditions the domain walls remain pinned; therefore dM_{irr}/dH must be zero and the magnetization is mostly reversible until magnetization traverses anhysteretic magnetization in these regions [41].

To effectively suppress these non-physical behaviors, reference [42] has introduced a new conditional parameter δ_M defined by

$$\delta_M = \begin{cases} 0 & if\ sign(H) \cdot sign(M_{an} - M) \leq\ 0\ (non\text{-}physical) \\ 1 & otherwise \end{cases} \tag{2.23}$$

where *sign*(.) function is given by

$$sign(x) = \begin{cases} 1, & if\ x \geq 0 \\ -1, & otherwise \end{cases} \tag{2.24}$$

Incorporating the new conditional parameter in (2.22) and

if $\delta_M = 1$

$$\frac{dM}{dB} = \frac{\delta_M \frac{(M_{an} - M)}{k\delta} + \frac{c}{\mu_0}\frac{dM_{an}}{dH_e}}{1 + \mu_0(1-\alpha)\left(\delta_M \frac{(M_{an} - M)}{k\delta} + \frac{c}{\mu_0}\frac{dM_{an}}{dH_e}\right)} \tag{2.25}$$

otherwise if $\delta_M = 0$

$$\frac{dM}{dB} = \frac{\frac{c}{\mu_0}\frac{dM_{an}}{dH_e}}{1 + (1-\alpha)c\frac{dM_{an}}{dH_e}} \tag{2.26}$$

Original authors had described a practical procedure to numerically estimate various model parameters α, c, and k using a small collection of experimental quantities that characterize material intrinsic magnetic properties, namely origin, loop tip, remanence, and coercivity points [41]. Nevertheless, deliberate tunings of these parameters were performed for better fitness over the entire range of measured hysteresis loop [41].

In the next chapter, a comprehensive intelligent procedure is introduced for J-A model parameters identification using published hysteresis loops and magnetization curve data. A novel constrained multi-objective optimization technique is proposed to simultaneously optimize J-A model parameters [41] and Annakkage anhysteretic form factor parameters [43] by a collection hysteresis loops with different magnetic induction peaks. For improved overall fitness, a new J-A model with variable parameters is defined and validated.

Solutions of these differential equations together with the choice of Annakkage anhysteretic function can be discretized and implemented in transient simulators to predict the evolution and trajectory of a quasi-static hysteresis, free of frequency / rate dependent loss components. Incorporation of frequency dependent losses is discussed in the next section and a full dynamic J-A model is then completed.

2.3 Frequency-Dependent Core Losses

The quasi-static J-A model reviewed in the preceding section represents only the frequency-independent hysteresis loss of a ferromagnetic material. Effects of hysteresis in electrically conducting media at different frequencies are manifested by classical and excess or anomalous eddy current losses and are discussed below.

2.3.1 Separation Principle of Losses

The conceptual simplification of separation of losses in soft ferromagnetic materials decomposes the average core power loss into hysteresis and dynamic contributions based on physical mechanism dictating these phenomena [61]. The total power loss is written as

$$\begin{aligned} P_{total} &= P_{hysteresis} + P_{dynamic} \\ &= P_{hysteresis} + P_{classical\ eddy} + P_{excess\ eddy} \end{aligned} \tag{2.27}$$

where $P_{hysteresis}$ correspond to the area enclosed by hysteresis cycle invariant to the magnetization rate, $P_{classcial\ eddy}$ arises as induced currents circulating through internal resistance dissipating heat in a varying magnetic field, and $P_{excess\ eddy}$ makes up a significant loss disparity of measured losses and theoretically calculated sum of hysteresis and classical eddy current losses, which is caused by irregular magnetic flux patterns different from the continuous forms assumed in classical eddy current calculation [62], [61], [63].

Separation of losses is hypothesized on the principle that characteristics time scales of hysteresis loss and eddy losses processes do not statistically overlap [63]. Conceptual

illustration in Figure 2.5 show how these losses change with respect to frequency in grain-oriented electric steels [55].

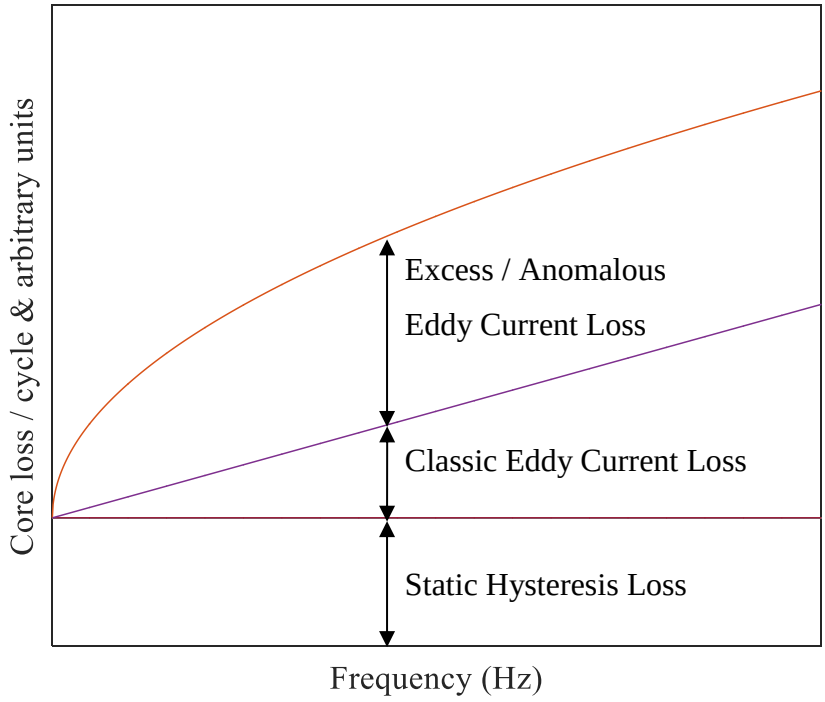

Figure 2.5 Conceptual illustration of core losses of GOES with frequency

2.3.2 Dynamic J-A Model with Rate-Dependent Core Losses

Frequency-dependent magnetization process of a ferromagnetic hysteresis, also referred to as dynamic hysteresis, widens the width of sigmoid wave shape [63]. This translates to a larger enclosed area that translates to a higher loss due to flux variation.

To incorporate frequency dependence behavior in the static J-A model, as explained by Bertotti the loss components can be mathematically represented by separate magnetic fields of quasi-static and dynamic parts by Equation (2.28) [55]

$$H_{dynamic} = H_{hyst} + H_{eddy} + H_{excess} \tag{2.28}$$

where the frequency independent hysteresis field H_{hyst} is calculated by static J-A model, and H_{eddy} and H_{excess} fields induced by classical eddy and excess eddy currents are related to the rate of flux density in the following expressions

$$H_{eddy} = k_1 \frac{dB}{dt} \tag{2.29}$$

$$H_{excess\ eddy} = k_2 \sqrt{\left|\frac{dB}{dt}\right|} \cdot sign\left(\frac{dB}{dt}\right) \tag{2.30}$$

with k_1 and k_2 the geometry and material relevant coefficients that can be estimated and adjusted for classical eddy and excess eddy currents [49]. Figure 2.6 illustrates frequency dependence effects of hysteresis loops for a grain-oriented electrical steel (GOES) specimen [31].

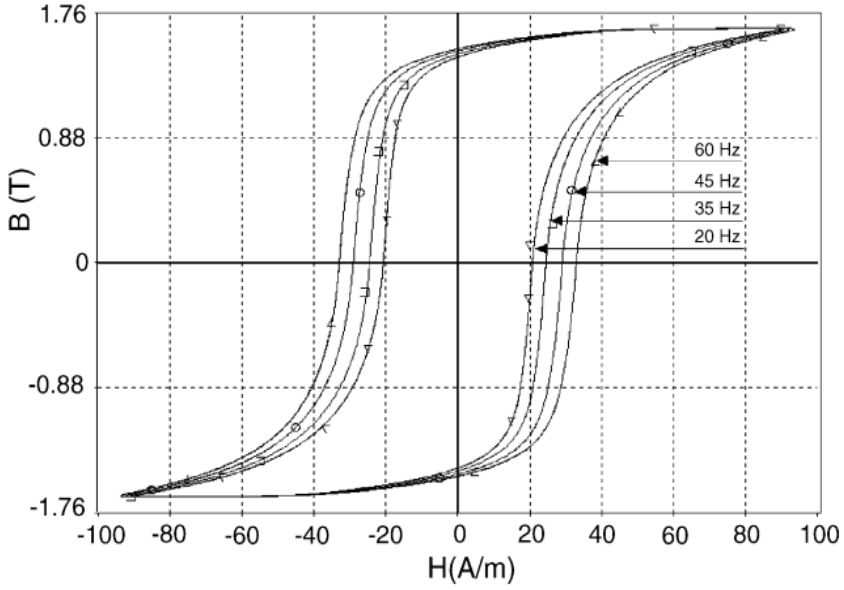

Figure 2.6 Frequency dependent effects on hysteresis loops of a GOES specimen [31]

2.4 Concluding Remarks

This chapter gave a careful review of Jiles-Atherton hysteresis theory and mathematical model of ferromagnetic materials and illustrated the derivation of an inverse J-A model expressed in terms of magnetic induction B. The J-A hysteresis model, due largely to its physical significant representation and accurate prediction of hysteresis characteristics, remained a popular choice in many engineering applications. An inconsistency in the original Jiles and Atherton papers caused misconceptions of J-A model and led to various forms of key equations often seen in literatures. Discussion on inverse J-A model brought clarifications on this issue and provided an illustrative derivation of faithful mathematical model in accordance to original J-A theory. Additional measures were introduced in this model to suppress non-physical solutions inherent in the original J-A model and to enhance its numerical stability. For power transformer modelling in a transient simulator like PSCAD/EMTDC, an inverse J-A model benefits from the fact its key variable – incremental magnetic induction ΔB can be directly calculated from transformer winding voltage thus meriting potential computation efficiency. Loss separation principle was reviewed to account for the frequency dependent effects of classical eddy and excess eddy currents, which together with static hysteresis calculated by J-A model could enable a more accurate representation of core losses in a power transformer model.

Chapter 3

J-A Model Parameters Identification by Multi-Objective PSO

3.1 Introduction

J-A hysteresis parameters extraction and identification processes have remained a difficult undertaking despite large popularity and continuous efforts. The challenge is attributed to the considerable complexity and high nonlinearity of the ordinary differential equations (ODEs) in J-A model, which require iterative solutions that often yields non-physical solutions and numerical divergence due to poorly defined parameters

In this chapter, a novel constrained multi-objective Particle Swarm Optimization (PSO) procedure has been proposed to identify J-A model parameters for a collection of hysteresis loops at various excitation peaks and magnetization curve simultaneously. An extensive literature review reveals that previous endeavours employed optimization or other numerical techniques on individual hysteresis loop and disregarded magnetization curve characteristics. The new process presented in this work facilitates simultaneous optimization on minor and major hysteresis loops, and utilizes the magnetization curve in determining Annakkage anhysteretic function parameters. Constraints on search

boundaries defined material physical properties and mathematical conditions have been imposed to overcome the aforementioned challenge and improve convergence rate in PSO. Published measurements of AK Steel M3 grade domain refined (DR) grain-oriented electrical steel (GOES) specimen is selected for validating this new procedure.

Initial simultaneous optimization attempts reveal that the existing J-A model with constant parameters exhibits limitations to fully fit measurements and visible departures have been observed when comparing calculated and measured quantities. Based on close inspection and parametric sensitivity analysis, a modified J-A model with a variable pinning parameter is proposed. Accordingly, a new methodology with the constrained multi-objective PSO embedded is introduced to define and optimize the modified J-A model parameters and demonstrates a substantially improved fitness of calculated and measured values.

3.2 Particle Swarm Optimization (PSO)

3.2.1 Concept

Particle swarm optimization (PSO) is a biological population based computation intelligence technique conceptualized on the stochastic and dynamic social behavior of each particle, the interaction among particles and collective movement of entire swam population [64], [65].

PSO offers an easy implementation and versatility in wide spectrum of applications, and has demonstrated a robust and consistent performance on nonlinear and multi-dimensional problems [45]. Adaptation of mechanisms such as velocity and inertia

maximizes both global and local exploration abilities while the cognitive and social attributes well balance the convergence speed and particle trajectories, thus making PSO an excellent tool for complex optimization paradigms [66].

3.2.2 Governing Principles and Mechanisms

In a complex multi-dimensional search space defined by a non-trivial optimization problem, particles are initially dispersed randomly at locations that each represents a possible solution and is arbitrarily assigned a velocity [66]. In every iteration also known as generation, particles are scrutinized by a group of fitness functions with the objective to locate the optima. Iteratively, particles record their personal best positions and promote the most prominent one as a new global optimum position of the entire swarm. Velocity and position of each particle are adjusted cognitively based on its proximity to the new global best position identified so far and are corrected to remain in the desired search boundary [64]. Progressively, individual particles traverse in search spaces while the entire swarm coherently aligns and rapidly approaches a global optimal position within the assigned maximum iterations [65].

3.3 Parameters Identification by Constrained Multi-Objective PSO

3.3.1 Published Data Selection, Preparation and Refinement

Technical specifications of converter power transformer stipulate strict requirements on permissible core and power losses, dimension consideration for transportation along with other considerations for LCC HVDC applications. In fulfillment of these conflicting design criteria, transformer designers need judiciously select an efficient and cost-effective core material to control the power loss, temperature rise and transformer size [6]. The 23mm M3 grade domain refined[3] (DR) high magnetic induction (Hi-B) grain oriented electrical steel (GOES) that offers both efficiency and economical merit is a logical choice for HVDC applications and hence considered forward.

GOES suppliers often publish measurements of magnetic hysteresis loops and magnetization curve recorded by the Epstein frame at very low frequencies [6]. This is why they are commonly referred to as dc hysteresis loops and dc magnetization curve respectively so that prior magnetization history and frequency related eddy current losses are eradicated and minimized [53]. In this work, catalogue measurements of a 23 mm M3 grade DR GOES specimen published by AK Steel have been extracted using a tool called GRABIT or similar programs in MATLAB [67], [68]. For improved resolution and

[3] Domain refinement entails a laser scribing treatment or similar process to enhance core loss characteristics [33]

preparation, these extracted data are further interpolated, resampled at a higher rate, and reconstructed into monotonic data series in MATLAB.

Hysteresis progression relies on history, so series of magnetic field strength H monotonically increasing from the origin to measured maximums of respective magnetic loop tips are artificially inserted to the measured data. This simple enhancement allows the calculated magnetic induction B to reach measured maximum targets. Contributions of these data are discarded and only a single complete hysteresis loop per cycle is included in the final fitness evaluation against measurements.

Figure 3.1 illustrated a collection of published measurements of quasi-static hysteresis loops with 1.0, 1.3, 1.5 and 1.7 T peak magnitudes and magnetization curve of AK Steel 23mm M3 grade DR GOES [67].

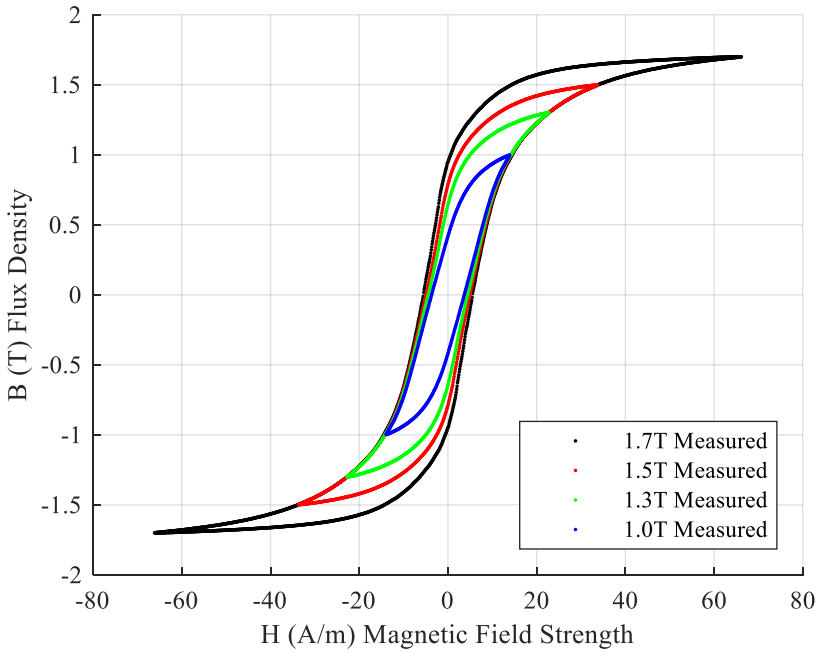

(a) Extracted static B-H hysteresis loops measurements

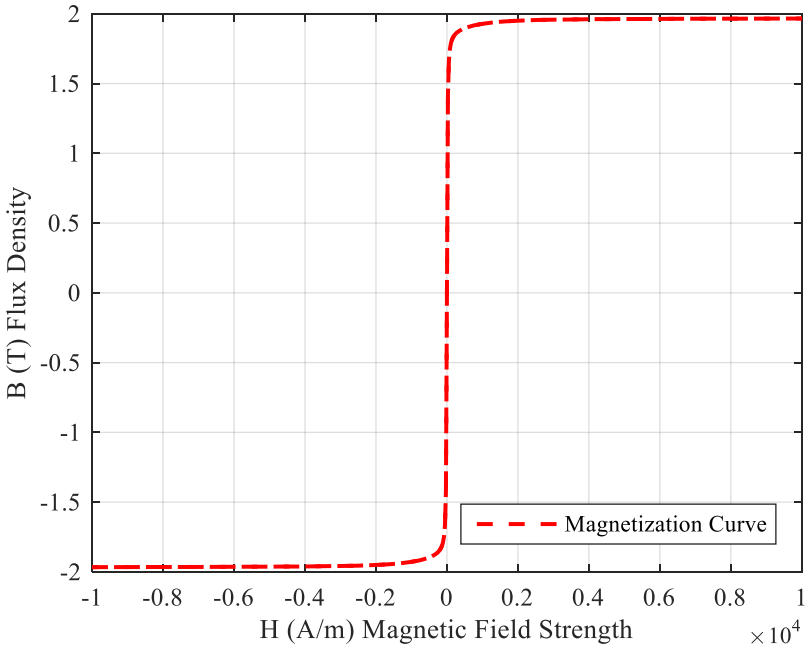

(b) Extracted static B-H magnetization curve measurements

Figure 3.1 Extracted measurements of AK Steel 23mm M3 Grade DR GOES

3.3.2 Restrained Initialization in PSO

In MATLAB, each particle i is erratically initialized with a set of seven positions that represent possible solutions in corresponding search spaces of J-A model parameters, namely $\alpha, c, k, \& M_s$ for magnetic domain related mechanisms and $a_1, a_2, \& a_3$ for Annakkage anhysteretic magnetization function. Particles are assigned a velocity and personal best history attributes that enables its explorability in the multi-dimensional search spaces. Together these seven positions constitute a family of potential solutions to J-A hysteresis model. Scalability of PSO is realized by sizing the swarm population.

In this work, PSO particle positions are arbitrarily populated using a uniform distribution and bounded by parameter search ranges summarized in Table 3.1. The range considered for parameter M_s respects the theoretical maximum saturation magnetization of pure iron and accounts for a decreased saturation magnetization effect in the presence of silicon substance infused in Si-Fe electrical steels [6], [56], [69]. Boundaries of remaining model parameters are empirically decided based on assessments of a few preliminary executions. These constraints encourage a faster convergence and act as secondary prevention measure of non-physical solutions [45].

Table 3.1 J-A model parameters search boundaries in PSO

Parameter	**Search Range**
$\boldsymbol{a}$	$[10^{-7}; 10^{-4}]$
$\boldsymbol{c}$	$[10^{-1}; 0.99]$
$\boldsymbol{k}$	$[1; 10^{2}]$
$\boldsymbol{M_s}$	$[1.68\times10^{6}; 1.72\times10^{6}]$
$\boldsymbol{a_1}$	$[10^{3}; 10^{5}]$
$\boldsymbol{a_2}$	$[10^{3}; 10^{5}]$
$\boldsymbol{a_3}$	$[10^{3}; 10^{6}]$

With no constrictions, arbitrarily populated solutions can be ill-defined which yield poor or unphysical predictions bearing no resemblances of hysteresis sigmoid wave shape at all. PSO algorithm does not have elimination or reproduction mechanisms equivalent to the mutation and crossover operators in the genetic algorithm (GA) to replace bad outlier

particles once they are formed [60]. To address this nuisance, a constrained initialization process has been conceived so that the fitness of each particle is calculated and scrutinized by a relaxed fitness threshold at beginning. New particles are created if the initial fitness of their predecessors exceeded the fitness threshold until the desired population size is reached. Conditions of Annakkage anhysteretic magnetization function coefficients $a_2 > a_1 > 0$ & $a_3 > 0$ are also enforced in initialization stage. This initialization initiative is believed to improve convergence speed on J-A model identification since particles are less likely to search in unpromising areas and are encouraged to converge in limited iterations [70]. Figure 3.2 gives a conceptual visualization of the constrained PSO initialization process.

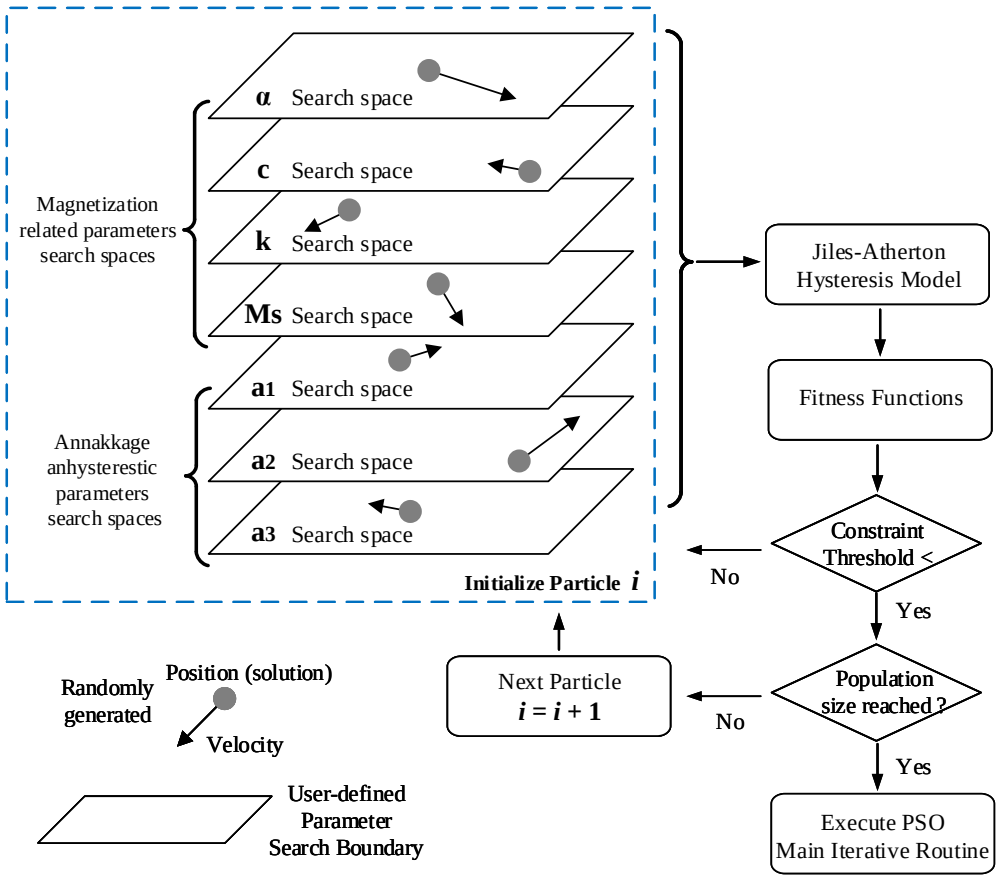

Figure 3.2 Restrained initialization of J-A model parameters in PSO

3.3.3 Particle Movement Structure and Rules

In each iteration, PSO assesses particles fitness and updates personal best $pbest$ position discovered in the current generation and endorses the one that produces the finest fitness of the whole swarm as the global best $gbest$. Prior to the next iteration, velocities in multi-dimension of particles are modified based on a joint consideration of individual tendency to continue its existing direction, knowledge of current individual personal best position and current global best position. The particle's movement and position change are dictated by the cognitive and social components described by the following governing principles [45], [64], [71], [72].

$$v_i^j(n+1) = w(t)\cdot v_i^j(t) + c_1\cdot rand(\,)\cdot\left(pbest^j(n) - x_i^j(n)\right) \quad + \; c_2 \cdot rand(\,)\cdot\left(gbest^j(t) - x_i^j(t)\right) \tag{3.1}$$

$$w(n+1) = \frac{N_{pop} - t}{N_{pop}}(w_{start} - w_{end}) + w_{end} \tag{3.2}$$

$$v_i^j(n+1) = min\left(\max\left(v_i^j(n+1), v_{min}^j\right), v_{max}^j\right) \tag{3.3}$$

$$x_i^j(n+1) = x_i^j(n) + v_i^j(n+1) \tag{3.4}$$

where x_i^j, v_i^j are the jth dimension position and velocity of particle i at present iteration n, $rand(\,)$ is a uniformly distributed random number function with an interval of [0, 1], terms w, c_1, c_2 are the inertia weight, cognitive and social acceleration constants respectively, w_{start}, w_{end} are the desired inertia weight adjusted in total N_{pop} iterations,

and v_{min}^{j}, v_{max}^{j} are clamping velocity limits defined as a portion of parameter search ranges specified in Table 3.1. These PSO system variables listed in Table 3.2 are typical values and refined empirically by trial and error [73]. Effects of different inertia weights *w*, acceleration constants c_1 and c_2, and common inertia adjustment strategies on the convergence trajectories have been analyzed in references [74], [75].

Table 3.2 Key PSO algorithm parameters

Variable	Value
$\boldsymbol{c_1}$	2.0
$\boldsymbol{c_2}$	2.0
$\boldsymbol{w_{start}}$	1.0
$\boldsymbol{w_{end}}$	0.5
$\boldsymbol{v_{max}^{j}}$	15% of permissible boundary range
$\boldsymbol{v_{min}^{j}}$	$-v_{max}^{j}$
$\boldsymbol{N_{pop}}$	50

Equation (3.1) describes how experience of individual and group exploration and exploitation is acquired by particles [64]. An inertia weight *w* plays an important role of balancing the local and global search in such a way that a bigger inertia weight *w* means less dependence on initial population hence a higher ability to exploit in new areas, and reversely a smaller value urges particle to explore locally near best positions [73]. Accordingly, Equation (3.2) linearly decreases inertia weight *w* in generations so that the

algorithm starts with a high exploitation ability to rapidly cover majority of search space and locate a promising position, then refine searches by local area exploration as the swarm statistically dwindles to a global optima at the end [45], [73]. Excessive particle velocities are regulated by Equation (3.3) to a maximum to prevent overflow and divergence issues [65], [73]. In addition, occurrences of particle trajectory trespassing pre-defined search boundaries are prohibited and rectified by clamping them to their boundary values and reverting the velocity direction. Likewise, anhysteretic coefficients $a_2 < a_1$ violations are corrected by swapping values of the two parameters. A new generation of particles is then updated in Equation (3.6) for the next iteration.

3.3.4 Multi-objective Fitness Function

Fitness functions are designed to evaluate the quality and performance of each particle's positions in multi-dimension for optimal J-A model parameters. They minimize the overall disparity between calculated and measured values in both unsaturated and heavily saturated regions. During power transformer switching, accurate hysteresis description is imperative in remanence flux prediction during a de-energizing event; whereas correct representation of magnetization curve is equally vital in determining inrush current in the subsequent energization.

With the sampled hysteresis loops and magnetization curve data, it is an intuitive choice to compare magnetization induction B and field intensity H calculated by J-A model with the corresponding measured quantities. Additionally, enclosed areas per cycle by hysteresis loops are included as a part of the fitness criteria as it is shown to further enhance the

convergence [45]. Data points on different hysteresis loops and magnetization curve carry uneven weights toward the fitness evaluation. For instance, fitness contribution B on a major hysteresis loop with a higher peak magnitude outweighs that of a minor loop. Similarly, field intensity H values on the magnetization curve far exceed that of hysteresis loops. Therefore, all quantities are normalized by measured maximums respectively to equalize individual dominance in fitness evaluation [76].

Equations (3.5), (3.6) and (3.7) translate fitness objectives into mathematical expressions for magnetization curve known also as B-H curve, hysteresis loops and enclosed areas that signify the static hysteresis loss. Fitness of magnetization curve only participates once while the later two executes four times for the four measured magnetic hysteresis loops. But only one single complete evolution per cycle of each calculated hysteresis loop by J-A model is compared to corresponding measured quantities.

$$fitness_{BHCurve} = \frac{1}{N_{data} \cdot \max(B_{meas})} \cdot \sum_{i=1}^{N_{pop}} \sum_{m=1}^{N_{data}} |B_{meas}^{m}(i) - B_{cal}^{m}(i)| + \frac{1}{N_{data} \cdot \max(H_{meas})} \cdot \sum_{i=1}^{N_{pop}} \sum_{m=1}^{N_{data}} |H_{meas}^{m}(i) - H_{cal}^{m}(i)| \tag{3.5}$$

where $fitness_{BHCurve}$ is the fitness index for the measured and calculated B-H curve, variables B_{meas}, H_{meas} and B_{cal}, H_{cal} are respectively the measured and calculated flux densities and intensities on B-H curve, N_{pop} denotes the size of PSO population, and N_{data} designates the size of each measurement.

$$fitness_{HystBH} = \sum_{q=1}^{N_{loop}} \left(\frac{1}{N_{data} \cdot \max(B_{meas})} \cdot \sum_{i=1}^{N_{pop}} \sum_{m=1}^{N_{data}} |B_{meas}^{m}(i) - B_{cal}^{m}(i)| + \frac{1}{N_{data} \cdot \max(H_{meas})} \cdot \sum_{i=1}^{N_{pop}} \sum_{m=1}^{N_{data}} |H_{meas}^{m}(i) - H_{cal}^{m}(i)| \right) \tag{3.6}$$

where $fitness_{HystBH}$ is the fitness index of measured and calculated hysteresis quantities N_{loop} is the number of measured hysteresis loops.

$$fitness_{HystLoss} = \sum_{q=1}^{N_{loop}} \frac{|Area_{meas}(q) - Area_{cal}(q)|}{Area_{meas}(q)} \tag{3.7}$$

where $fitness_{HystLoss}$ is the fitness index of enclosed areas for the measured and calculated hysteresis loop per cycle. These areas are numerically estimated by iterative trapezoidal integrations in MATLAB. Normalization is also applied by scaling calculated and measured quantities by respective measured maximum area.

In fact, each fitness function member is conceived to fulfill a single objective and individual global optima - not necessary a unanimously collaborated one for all evaluation criteria. Accordingly, a universal global best is constructed in (3.8) to harmonize the compelling force of individual global best and to create a virtual cohesive global best

$$Fitness = W_{BHCurve} \cdot fitness_{BHCurve} + W_{HystBH} \cdot fitness_{HystBH} + W_{HystLoss} \cdot fitness_{HystLoss} \tag{3.8}$$

where $W_{BHCurve}$, W_{HystBH}, and $W_{HystLoss}$ are weighting factors of respective fitness objectives and are determined empirically with values of 5, 10 and 5. Figure 3.3 illustrates

the concept of abovementioned individual fitness objectives and the universal fitness function in PSO.

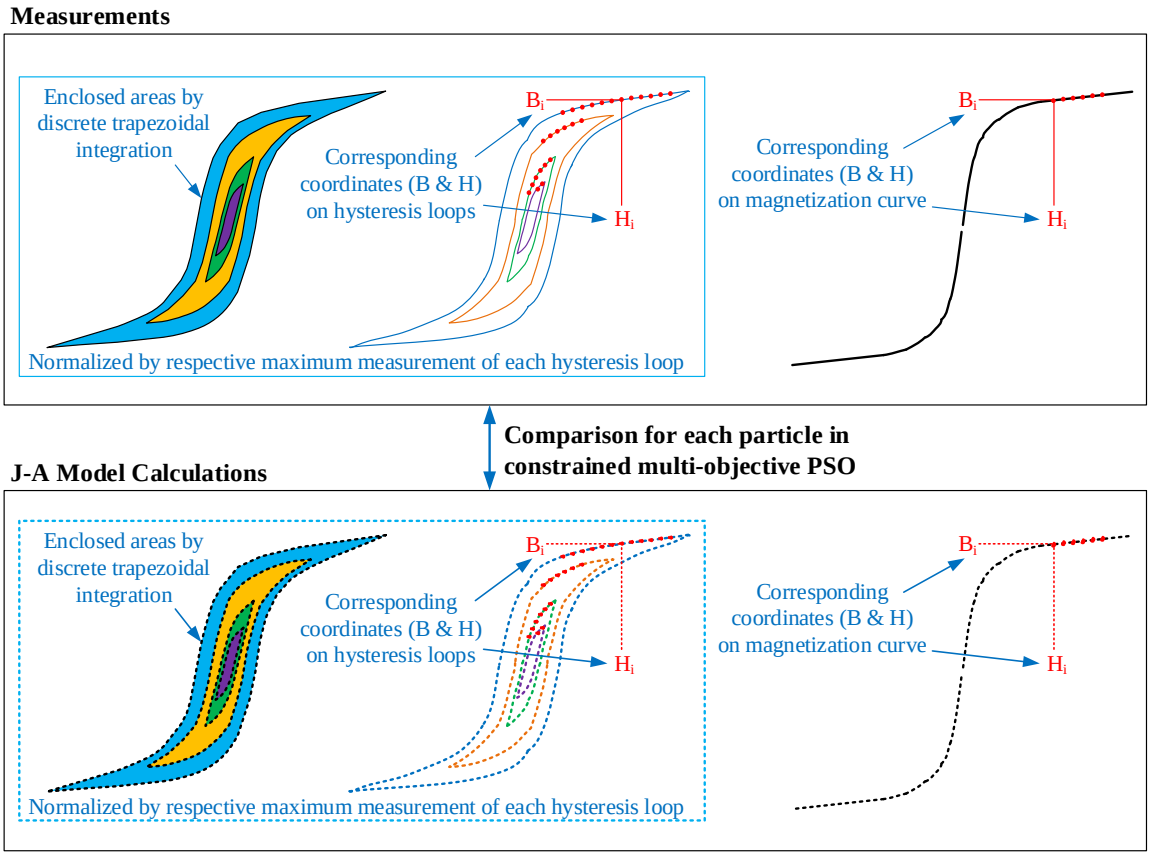

Figure 3.3 Qualitative illustration of PSO multi-objective fitness functions

3.3.5 Simultaneous Static J-A Model Parameters Identification

Before commencing a more complex optimization on magnetization curve and simultaneously all fours measured hysteresis loops, it is prudent to first demonstrate model parameters identification using PSO with magnetization curve and a single hysteresis loop. Figure 3.4 outlines a complete identification procedure capable for both individual separate and simultaneous optimization.

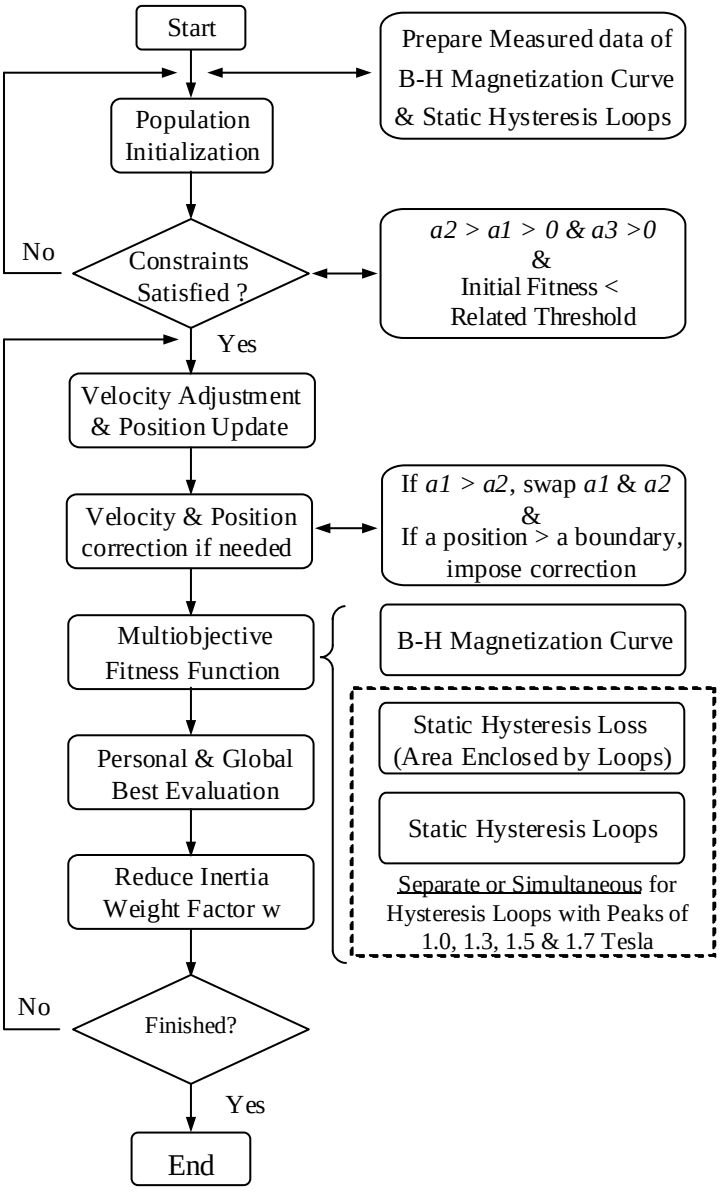

Figure 3.4 Multi-objective PSO procedure for J-A model parameters identification

In the case of separate hysteresis loop optimization, a population size of 1000 particles and 25 iterations are considered in the constrained multi-objective PSO algorithm. Comparisons of measured and calculated quantities in Figure 3.5 to Figure 3.8 show satisfactory agreements and validate the effectiveness of the proposed optimization procedure for the combination of a single hysteresis loop and magnetization curve.

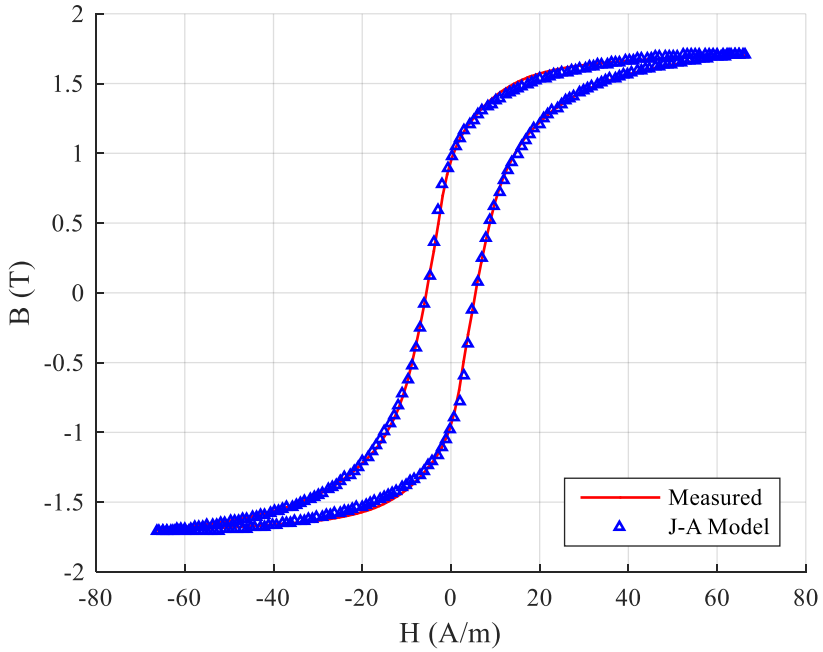

(a) 1.7 T static magnetic hysteresis loop

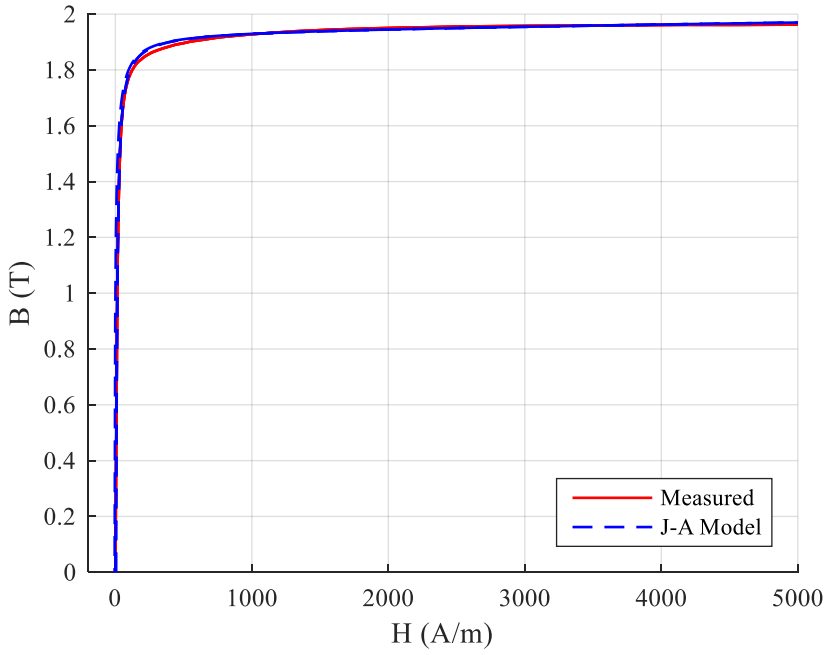

α	c	k	M_s	a_1	a_2	a_3
5.22×10^{-6}	0.21	9.94	1.69×10^{6}	2.44×10^{4}	2.67×10^{4}	2.28×10^{5}

(b) Static magnetization curve & identified J-A model parameters

Figure 3.5 Measured & calculated single 1.7 T hysteresis loop and B-H curve

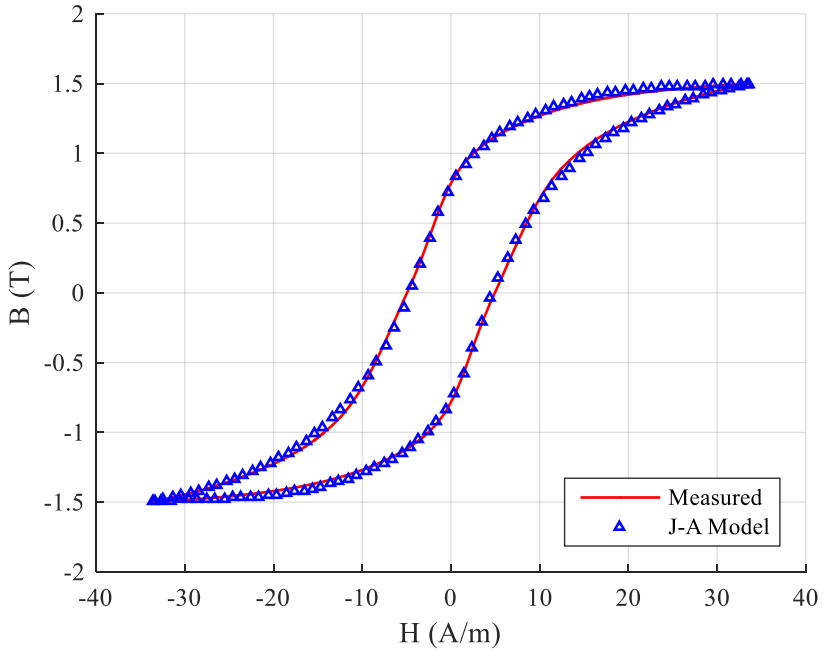

(a) 1.5 T static magnetic hysteresis loop

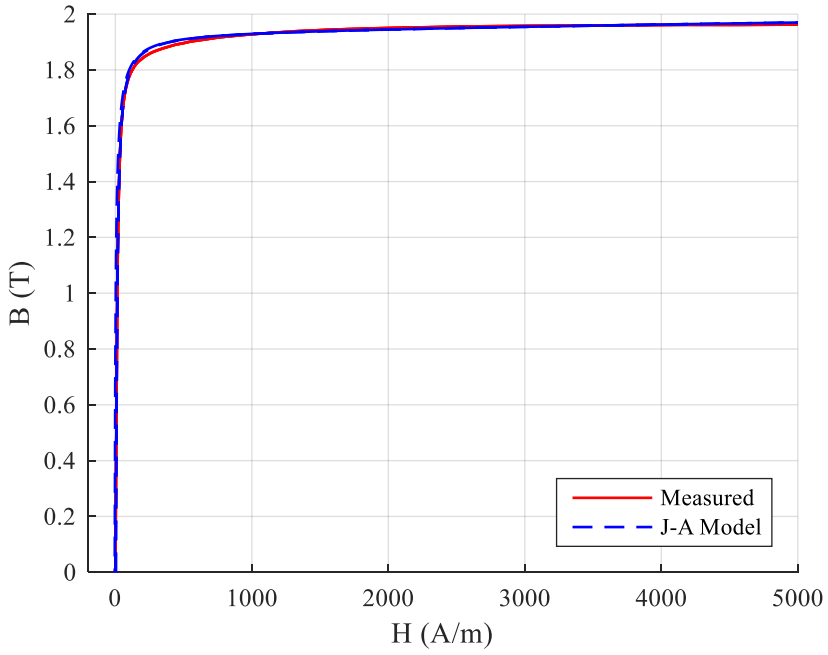

α	c	k	M_s	a_1	a_2	a_3
4.32×10^{-6}	0.28	9.17	1.693×10^{6}	5.1×10^{4}	5.59×10^{4}	5.25×10^{5}

(b) Static magnetization curve & identified J-A model parameters

Figure 3.6 Measured & calculated single 1.5 T hysteresis loop and B-H curve

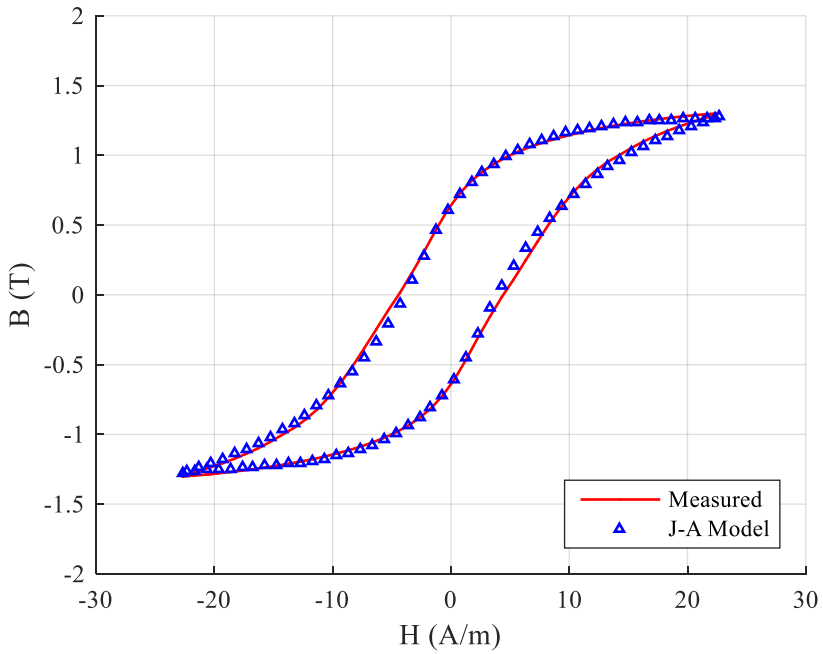

(a) 1.3 T static magnetic hysteresis loop

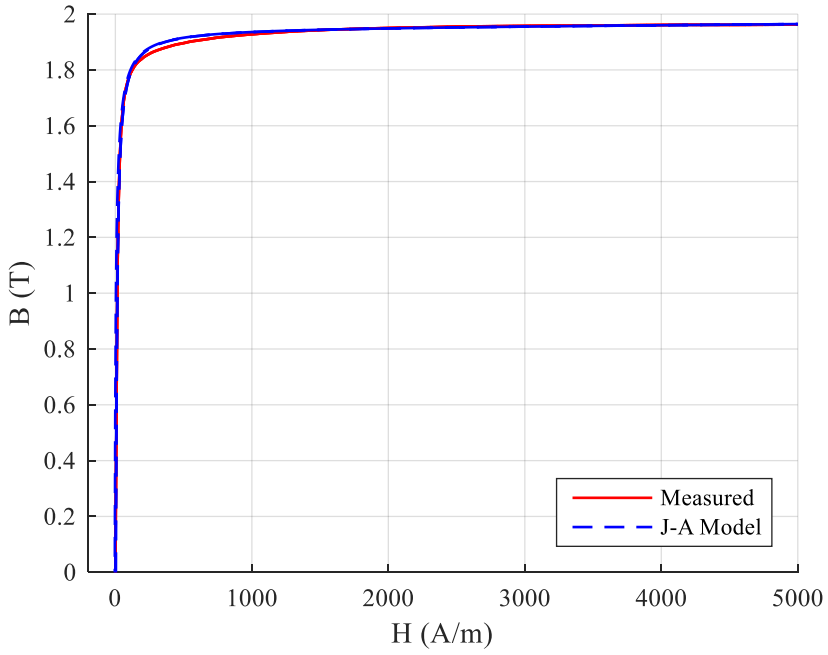

α	c	k	M_s	a_1	a_2	a_3
3.55×10^{-6}	0.28	8.16	1.695×10^{6}	7.63×10^{4}	8.33×10^{4}	8.49×10^{5}

(b) Static magnetization curve & identified J-A model parameters

Figure 3.7 Measured & calculated single 1.3 T hysteresis loop and B-H curve

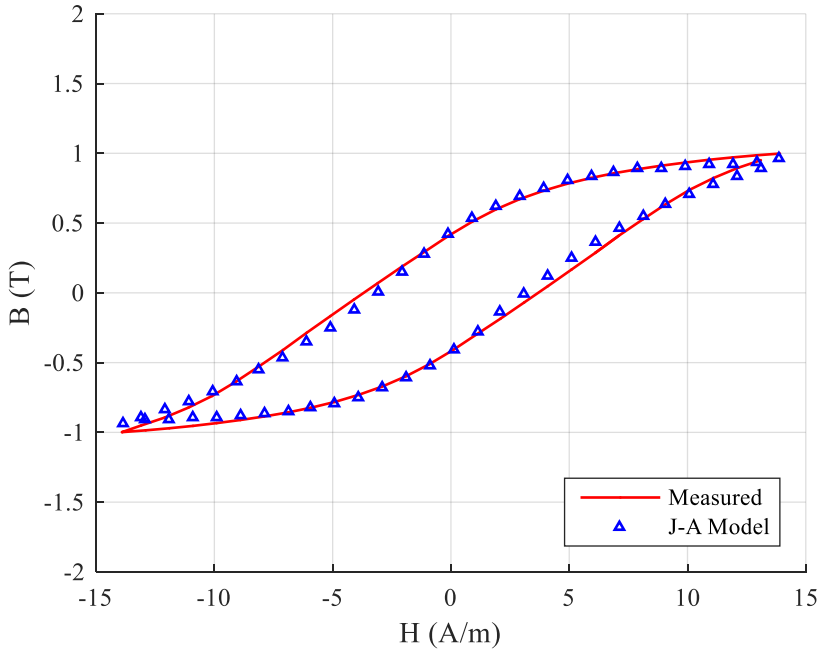

(a) 1.0 T Static Magnetic Hysteresis Loop

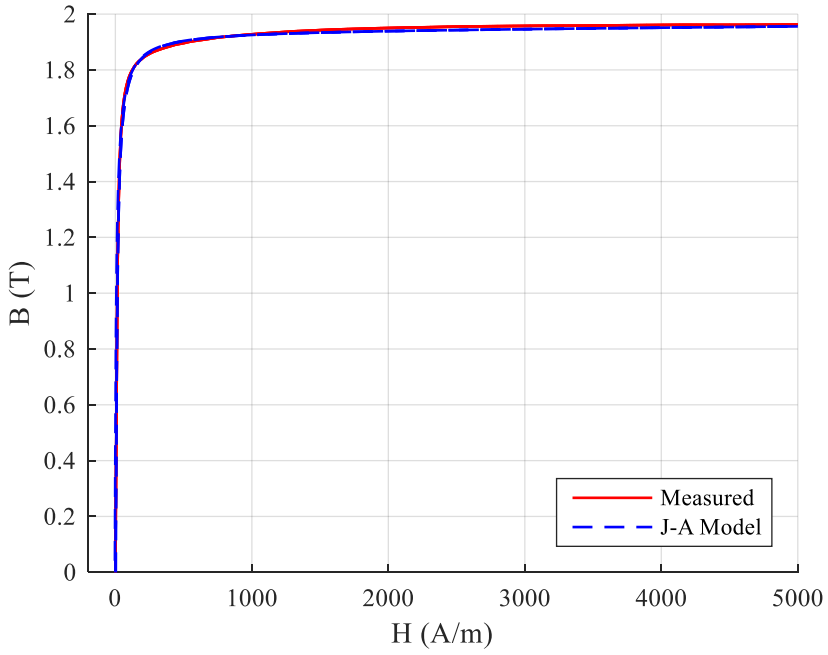

α	c	k	M_s	a_1	a_2	a_3
1.35×10^{-6}	0.22	6.12	1.696×10^{6}	6.56×10^{4}	7.23×10^{4}	7.58×10^{5}

(b) Static magnetization curve & identified J-A model parameters

Figure 3.8 Measured & calculated single 1.0 T hysteresis loop and B-H curve

Aforementioned J-A model parameters identified by the constrained PSO of each single hysteresis loop and magnetization curve have been reproduced in for readers' convenience. Variances of these parameters for different hysteresis loops imply there are more than one possible set of solutions while maintaining a good agreement on the magnetization curve. A slight difference of calculated and measured is noticed near the knee point on the magnetization curve. This could be further improved by a modified five-parameter Annakkage anhysterestic function as given in Appendix A.1, which offers an even higher degree of freedom but is not further explored as a trade-off of complexity and proficiency.

Table 3.3 Summary of optimal J-A model parameters for single B-H loop and curve

	Identified J-A model parameters by constrained multi-objective PSO						
B-H curve &	$\boldsymbol{\alpha}$	$\boldsymbol{c}$	$\boldsymbol{k}$	$\boldsymbol{M_s}$	$\boldsymbol{a_1}$	$\boldsymbol{a_2}$	$\boldsymbol{a_3}$
1.7 T B-H loop	5.22×10^{-6}	0.21	9.94	1.69×10^{6}	2.44×10^{4}	2.67×10^{4}	2.28×10^{5}
1.5 T B-H loop	4.32×10^{-6}	0.28	9.17	1.693×10^{6}	5.1×10^{4}	5.59×10^{4}	5.25×10^{5}
1.3 T B-H loop	3.55×10^{-6}	0.28	8.16	1.695×10^{6}	7.63×10^{4}	8.33×10^{4}	8.49×10^{5}
1.0 T B-H loop	1.35×10^{-6}	0.22	6.12	1.696×10^{6}	6.56×10^{4}	7.23×10^{4}	7.58×10^{5}

It is also observed that J-A model parameters optimized for a single hysteresis loop and magnetization curve shows limited predictions for other loops. For illustration, large deviations, especially near B axis intercept points for remanence fluxes, arise in Figure 3.9 as the field intensity H magnitude decreases when applying the model parameters optimized for 1.7 T hysteresis loop on other three loops. As a result, error would be

introduced in remanence flux prediction. This articulates the necessity of simultaneous optimization including measured data for an overall fitness.

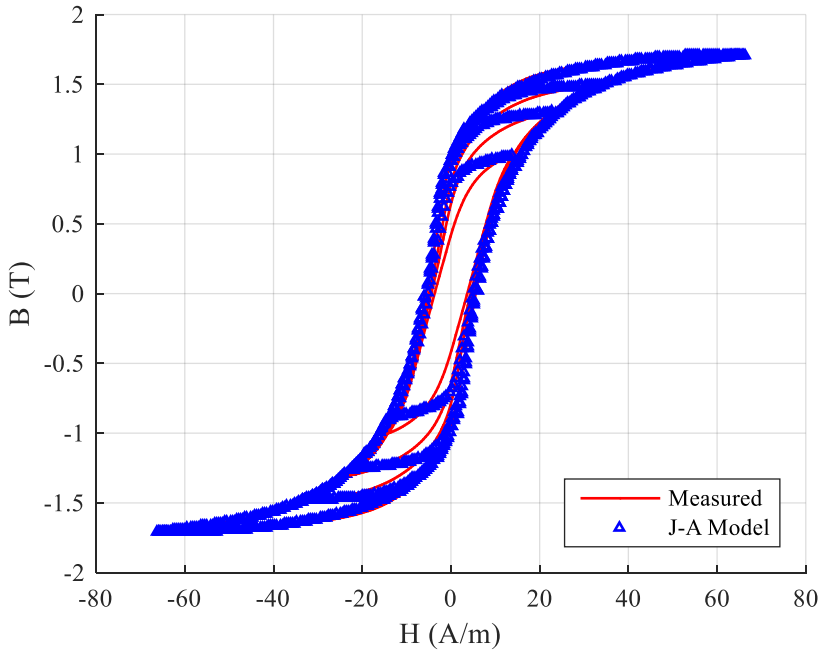

Figure 3.9 Overall fitting by parameters optimized for single 1.7T hysteresis loop

For the simultaneous optimization of all four magnetic hysteresis loops, the population size and number of iterations have been increased to 5000 and 50 respectively given the higher level of complexity involved. Figure 3.10 shows a visible discrepancy between measured and calculated values on the 1.7 T major loop, though minor loops and B-H magnetization curve exhibit good accuracy. A close inspection of Figure 3.9 and Figure 3.10 reveals that calculated B and H values well agree with measured quantities when H is positive and rising in the first quadrant or negative and reducing in the fourth quadrant, but deviate on the reverse directions for positive and reducing H and conversely negative and rising H. This observation of hysteresis loop width difference resonates with remarks made

in reference [43] but here discrepancies manifest on the opposite sides of hysteresis loops. Nonetheless, this limitation can result in inaccurate remanence fluxes calculation and inevitable error for studies like transformer energization where remanence flux is critical. It is even more onerous for HVDC converter transformers whose fluxes can vary widely due to large on-load tap changer operating range.

Hysteresis loop width is mainly dictated by the pinning parameter k [41]. It is therefore necessary to adjust k and such notion is in accordance with J-A theory and parallel to publications [35], [43], [77], [78], [79], [80]. The pinning parameter reflects the impurities of a material and analysis of measured hysteresis loops confirm a lower value at a smaller field and a higher value at larger field, which is probably attribute to a greater participation of larger ferromagnetic domains in the process of magnetization generated by stronger magnetic fields [28], [79]. Therefore, it is recognized that J-A model parameters optimized for a single hysteresis loop are only valid for a limited range of the applied field which is a basic limitation of the original J-A model [81].

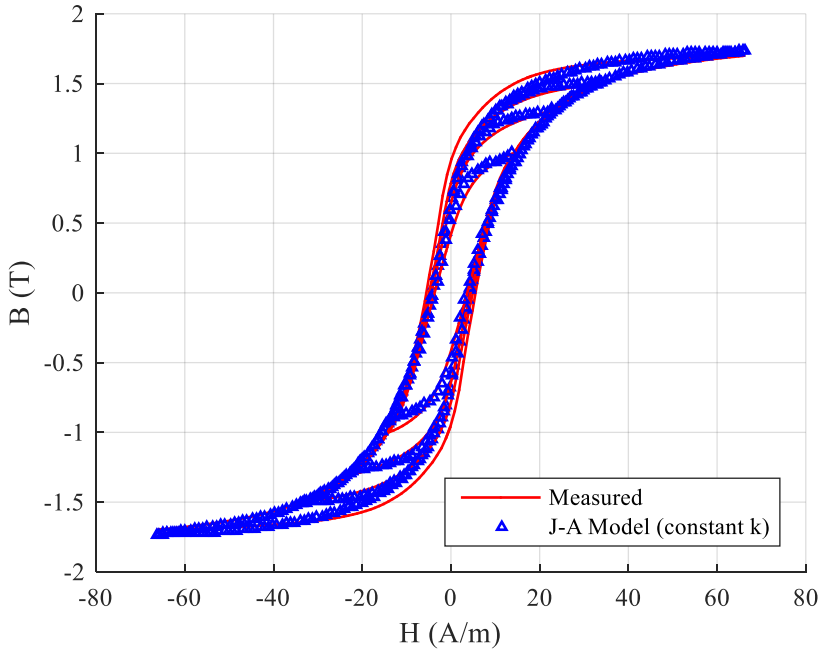

(a) Overall static magnetic hysteresis loops

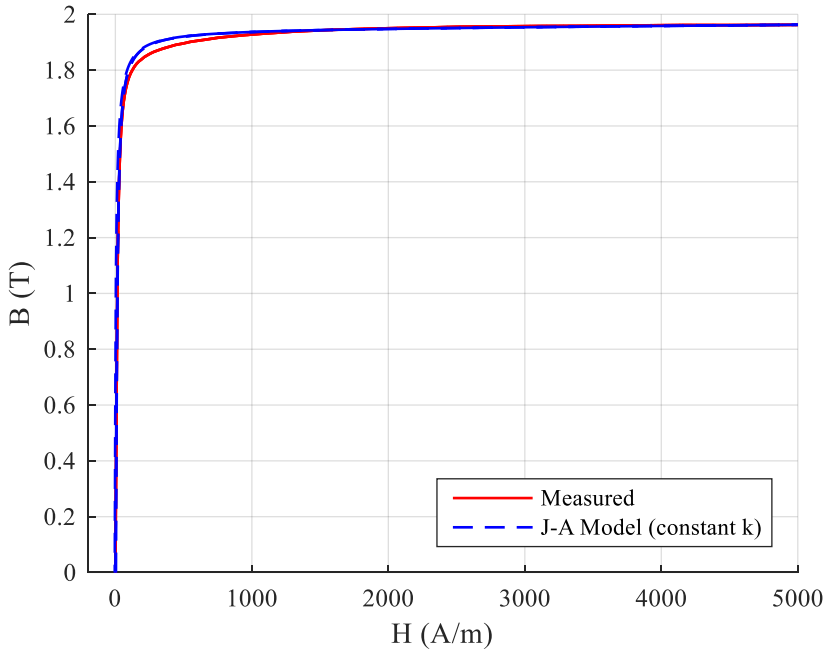

α	c	k	M_s	a_1	a_2	a_3
1.0×10^{-6}	0.3	7.8	1.69×10^{6}	2.44×10^{4}	2.67×10^{4}	2.28×10^{5}

(b) Overall static magnetization curve & identified J-A model parameters

Figure 3.10 Measured & simultaneously calculated B-H loops and curve fitness (classic J-A model & constant k)

To address this deficiency, several modifications of J-A model with variable pinning parameter k have been proposed. However, most of surveyed literature did not elaborate on a systematic derivation process of functions proposed for the variable pinning parameter k [43], [77], [78], [79], [80]. In the following section, a novel systematic process is developed for defining the pinning parameter as a function of magnetization level. The process utilizes the constrained multi-objective PSO technique developed earlier in this chapter.

3.4 Modification and Improvement of J-A Model

3.4.1 Variable Parameter and Function Definition

The variable pinning parameter k has been proposed in various literature as functions of magnetic induction B, or field intensity H, or magnetization have linear or exponential forms [43], [77], [78], [79], [80]. Magnetization M is a better candidate to associate such variations. This is because in contrast to the two former alternatives (B and H), M is more directly related to the internal dynamics and behavior of magnetic structures, and bounded by lower and upper limit values of zero and M_s respectively in a ferromagnetic material. Besides, a continuous function of M is desirable for modeling pinning parameter to prevent any potential numerical issues when implementing the proposed modifications in an EMT environment.

3.4.2 Modified J-A Model with Variable Pinning Parameter k

Variation of the pinning parameter k for each of the four measured hysteresis loops with respect to the change of magnetization M need to be captured so that a functional relation between the two quantities can be defined. This is accomplished by executing multi-objective PSO algorithm with parameters a, c and k purposely relaxed to travel in respective search spaces. Saturation magnetization M_s and anhysteretic function parameters a_1, a_2 and a_3 are temporarily restrained to previously identified values. Maximum degree of freedoms on the magnetic domain related parameters of a, c, k is granted with low interference from anhysteretic magnetization. Upon optimization of all four hysteresis loops separately, variation of pinning parameter k with the relative magnetization level M/M_s is obtained and plotted in Figure 3.11.

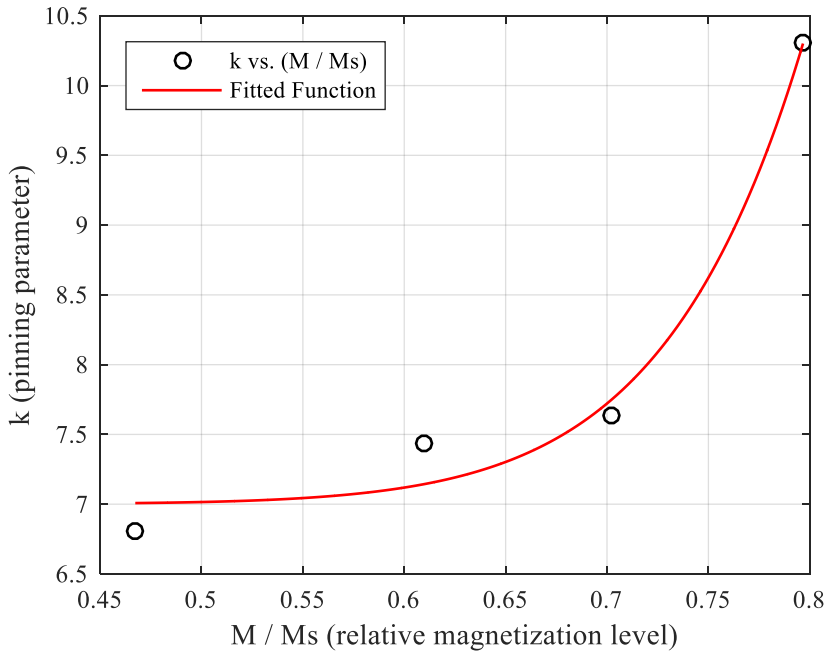

Figure 3.11 Variation of pinning parameter k with relative magnetization level M/M_s

Based on the observed data points, a power series function in Equation (3.9) is hypothesized to alter the hysteresis loop width, hence the loss for positive and decreasing or negative and increasing magnetization levels.

$$k_{eff} = k_s \left(1 + pk_1 \cdot \left(\frac{M}{M_s}\right)^{pk_2}\right) \tag{3.9}$$

where k_{eff} is the effective domain pinning parameter, k_s is a static pinning parameter at zero magnetization, pk_1 and pk_2 are two coefficients to adjust k_{eff} as magnetization M varies with respect to the saturation magnetization M_s of a material. The ratio of M/M_s is bounded to [0-1]. As discussed previously, the rise of domain pinning parameter is perceived as a more active involvement of domain structure at larger magnetization and the effective variable pinning parameter k_{eff} is used to substitute the constant value in the classical J-A model. The red curve in Figure 3.11 shows the fitting of k_{eff} in Equation (3.9) to the data points using a nonlinear curve fitting method.

3.4.3 New Methodology for Identification of Modified J-A Model

The data points in Figure 3.11 are obtained through optimization of pinning parameters for separate hysteresis loops while deliberately restraining anhysteretic function. Although Equation (3.9) defines a general expression of variable pinning parameter, the better approach is to include it in model parameter identification of modified J-A model as defined in the last section. This enables a comprehensive optimization and determines all parameters simultaneously for all four hysteresis loops and magnetization curve. A new

methodology with the constrained multi-objective PSO imbedded as the core algorithm has been envisioned in Figure 3.12 to facilitate this overall optimization.

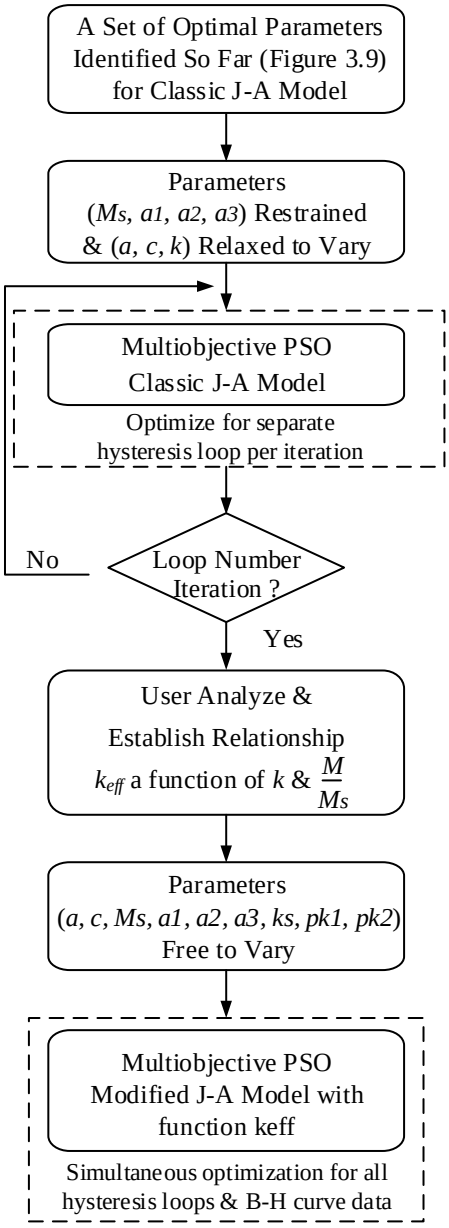

Figure 3.12 New optimization methodology for modified J-A model with variable *k*

It is demonstrated in Figure 3.13 that the modified J-A model with the variable pinning parameter *k* significantly improves the agreement of measured and calculated hysteresis loops and magnetization, thus validating the proposed modifications.

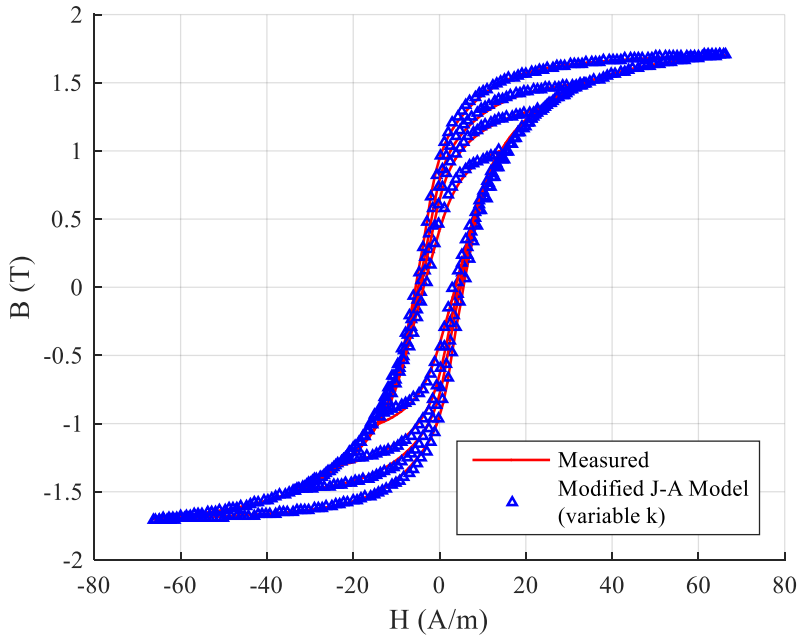

(a) Overall static magnetic hysteresis loops

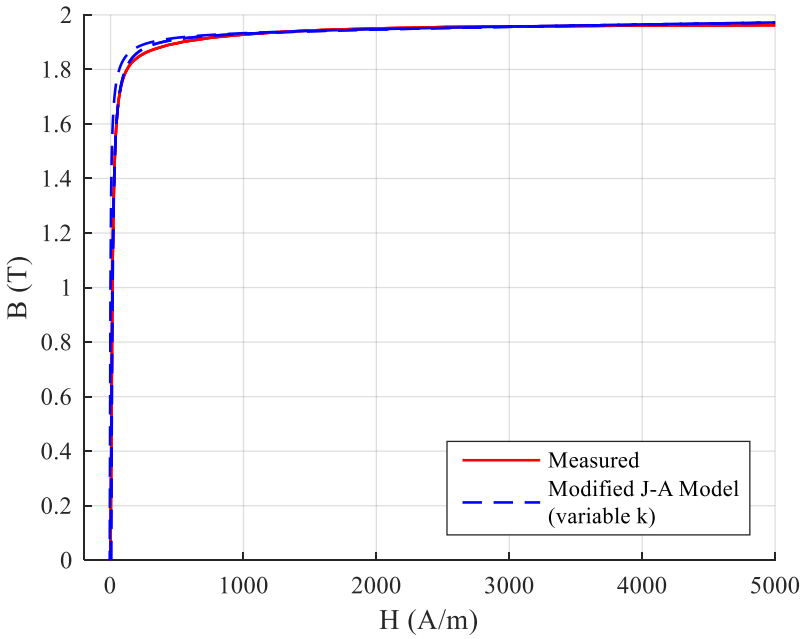

α	c	k_s	M_s	a_1	a_2	a_3	pk_1	pk_2
1×10^{-6}	0.3	7.8	1.69×10^{6}	2.43×10^{4}	2.67×10^{4}	2.28×10^{5}	31.67	4.77

(b) Static magnetization curve & identified modified J-A model parameters

Figure 3.13 Measured and calculated B-H loops (modified J-A model & variable k) with parameters obtained through simultaneous optimization

In Figure 3.14, measured and calculated hysteresis loops and magnetization curve are reproduced and directly compared for readers' convenience.

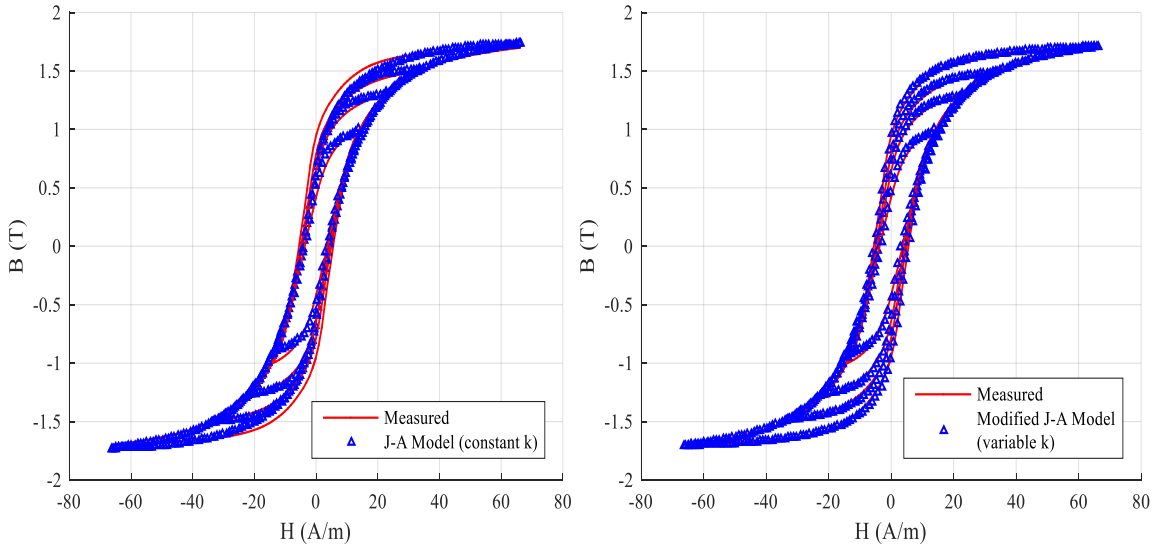

(a) Static hysteresis loops

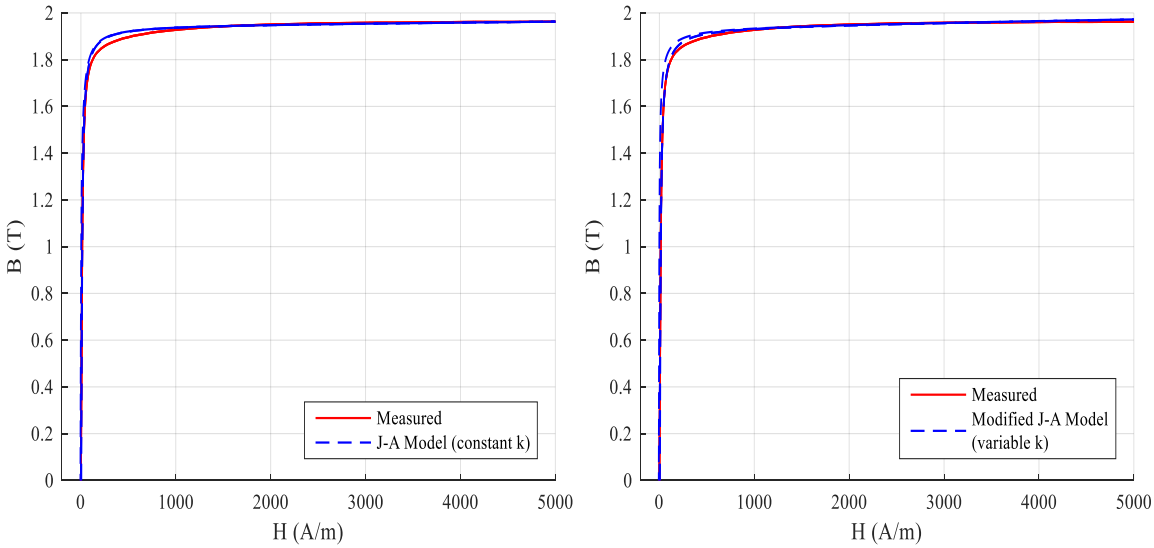

(b) Static magnetization curve & identified modified J-A model parameters

Figure 3.14 Comparison of simultaneously optimized B-H loops and curve for J-A model with constant parameters versus improved J-A model with variable pinning k

A population size of 5000 particles, each initialized with a group of nine positions for the modified J-A model, and 50 iterations have been considered for the constrained multi-objective PSO algorithm. With the above parameters, a satisfactory convergence was achieved on the universal fitness objectives. By the same philosophy, additional accuracy could be gained by replacing all magnetization related constant parameters with variable parameters and the anhysteretic magnetization function with five shape factor parameters instead of the existing three in J-A model. Although the newly developed procedure is fully capable of defining variable parameter functional relations and optimization, it should be argued that effectiveness and benefits of having these other modifications must not be at expenses of undue and excessive complexity and computation burden. Therefore, these efforts were not further preceded or explored in this work.

3.4.4 Dynamic J-A Model Core Loss Coefficients Identification

In general, geometry information and electrical properties are required to estimate k_1 and k_2 coefficients for classic and excess eddy current losses but typically fine tuning is further needed for improved accuracy [49]. In this work, only plots of frequency dependent hysteresis loops measurements at 1.0 T, 1.5 T and 1.7 T of a compatible 23mm M3 DR GOES have been made available for 50 Hz. No time domain waveforms can be extracted from these hysteresis loops, so it is appreciated that a trial and error approach has to be used for identifying the eddy losses related coefficients. This approach is further discussed in the next chapter when implementing dynamic J-A model in PSCAD/EMTDC program. If adequate time domain data is available, it is thought that additional fitness objective could be created for the identification of dynamic J-A model parameters.

3.5 Concluding Remarks

A constrained multi-objective PSO algorithm was developed and validated to successfully predict individual magnetic hysteresis loop and magnetization curve by evaluating calculated values and published measurements of a AK Steel 23mm M3 grade DR GOES. Measurements comprised of quasi-static hysteresis loops with peak magnetic flux density magnitudes of 1.0, 1.3, 1.5 and 1.7 T and magnetization curve. Properties such as a constrained initialization process, a dynamically adjusted inertia weight, correction mechanisms on outbound particles and condition violations of Annakkage anhysteretic function parameters were incorporated into a PSO. A collection of fitness objective functions was properly selected for magnetic description in both unsaturated and heavily saturated regions. This novel approach was shown to improve convergence rate and to effectively prevent ill-defined J-A model parameters as well as non-physical calculations. However, it was demonstrated that parameters optimized for a single hysteresis loop and magnetization curve was accurate in a rather limited range of applied fields which was recognized as a fundamental limitation of the original J-A model [81].

Comparison of measurement and J-A model calculation revealed visible discrepancy on the hysteresis loop width, which was an attribute mainly dictated by domain wall pinning parameter k. Accordingly, a new methodology utilizing the constrained multi-objective PSO algorithm was created to define a functional relation of the pinning parameter k with relative magnetization M/M_S. A new variable pinning parameter k_{eff} was introduced in a modified J-A model as a replacement of original constant parameter. An automated simultaneous optimization procedure of all four hysteresis loops and

magnetization curve was then executed for modified J-A model identifications. The modified J-A model with variable pinning parameter and well optimized parameters significantly improved the overall accuracy of hysteresis loops and magnetization curve, hence validating the proposed modifications.

A precise representation of ferromagnetic behavior in both unsaturated and heavily saturated regions is vital in remanence flux prediction of power transformer de-energization and inrush current calculation in a subsequent energization. Core losses coefficients identification by an empirical trial and error method will be discussed in the following chapter due to limitation of measured data available. In the next chapter, the modified frequency-dependent J-A model is incorporated in a magnetic-duality based five-limb converter transformer model on which an extensive analysis is later performed to assess the controlled switching strategies in PSCAD/EMTDC.

Chapter 4

Controlled Switching Studies: Theory and Improved Transformer Model

4.1 Introduction

In this chapter, underlying theory on how the knowledge of remanence flux can enable inrush current elimination of unloaded power transformer energization is first introduced, based on which a representative controller model is developed in PSCAD/EMTDC. The working principle of AC circuit breaker pre-insertion resistor on inrush current suppression is compared. To properly represent topological core and ferromagnetic characteristics, a new five-limb transformer model is introduced in PSCAD/EMTDC and improved with the modified J-A ferromagnetic hysteresis model proposed in Chapter 3.

4.2 Inrush Current Elimination by Controlled Switching Technique

4.2.1 Theory and Underlying Principle

When a transformer is energized, the applied voltage has a prospect to induce a prospective magnetic flux on transformer wound cores [8]. If it occurs at an instant that results in flux magnitude to increase beyond core saturation, excessive inrush currents can be generated. Winding inductance is proportional to the slope of flux and current curve, so transformer winding cores behave like nonlinear inductances which becomes very small in deep saturation region and create high inrush currents [8]. Therefore, preventing transformer core saturation can effectively eliminate undesired inrush currents and this can be accomplished by energizing the transformer windings at instants when the prospective fluxes are equal to core remanence fluxes [8].

For illustration, the total magnetic flux on transformer core at an arbitrary energization instant of a single-phase transformer neglecting winding and core losses can be analytically calculated by

$$\begin{aligned}\Phi_{core}(t) &= \Phi_{remanence} + \frac{1}{N}\int_{t_{close}}^{t+t_{close}} V_{source}(t)dt \\ &= \Phi_{remanence} + \frac{V_{LN}}{N\omega}cos(\omega t_{close}) - \frac{V_{LN}}{N\omega}\cos\big(\omega(t+t_{close})\big)\end{aligned} \tag{4.1}$$

where Φ_{core} total instantaneous core flux at energization (T),

$\Phi_{remanence}$ remanence flux on core from the prevailing de-energization (T),

$V_{source}(t)$ source voltage time function assumed of a sinusoidal function (kV),

t_{close} energization instant (s),

t time (s),

V_{LN} primary voltage peak magnitude (kV),

N transformer energizing side winding turns,

ω source voltage angular speed (rad),

$\frac{V_{LN}}{N\omega} cos(\omega t_{close})$ source voltage induced prospective flux at time t_{close}.

An optimal instant can be predicted so that perspective and remanence fluxes are neutralized, hence diminishing the resultant inrush current. If transformer core becomes saturated, majority of magnetic fluxes escape to the air surrounding winding cores and inrush current formation can be analytically calculated by relating magnetic and electrical properties with all losses neglected in Equation (4.2) [82]:

$$
\begin{aligned}
i_{inrush} &= \frac{N\Phi_{air}}{L_{air}} = \frac{NA_{air}}{L_{air}} B_{air} \\
&= \frac{NA_{air}}{L_{air}} \frac{A_{core}}{A_{air}} (2B_{nominal} + B_{remanence} - B_{saturation}) \\
&= \frac{NA_{core}}{L_{air}} B_{asymmetry} \\
&= \frac{NA_{core}}{\frac{N^2 \mu_0 A_{air}}{Length_{air}}} B_{asymmetry} \\
&= \frac{1}{\mu_0} \frac{A_{core}}{A_{air}} \frac{Length_{air}}{N} B_{asymmetry}
\end{aligned}
\tag{4.2}
$$

where i_{inrush} magnetizing inrush current magnitude

N number of winding turns on the energized coil

Φ_{air} escaped magnetic flux to air due to core saturation (Wb)

L_{air} linear air inductance (H)

B_{air} escaped magnetic flux density (T)

A_{air} cross section area closing escaped magnetic flux after core saturation (m^2)

A_{core} cross section area of wound core limbs (m^2)

$B_{nominal}$ nominal magnetic flux density in steady state (T)

$B_{remanence}$ remanence magnetic flux density (T)

$B_{saturation}$ magnetic flux density of a ferromagnetic core saturation limit (T)

$B_{asymmetry}$asymmetrical magnetic flux density due to remanence (T)

μ_0 vacuum permeability coefficient

$Length_{air}$ equivalent length of air core inductor (m)

This equation analytically confirms inrush current reduction by magnetic flux asymmetry removal and suggests that alternatively higher number of winding turns can alleviate inrush current, which rationalizes the prevailing industry practice of a transformer energization with maximum winding turns [19].

In a 12-pulse HVDC transmission network, a pair of three-phase transformers with YNy0 and YNd1 vector groups is generally connected electrically in parallel and switched by a single AC circuit breaker for optimal and economical filter designs. Unlike the three-limb counterparts, questions such as effectiveness of optimal closing instants and remanence flux distribution patterns arise on controlled switching while accounting for

remanence flux of a pair of five-limb HVDC converter transformers operating in parallel with a single delta winding connection.

4.2.2 Controlled Switching: Delayed Closing Strategy

Presence of three-limb core or delta connected winding ensures a core flux equalization phenomenon which is the underlying principle of optimal controlled switching [8]. However, they also revert the static fluxes on the two remaining phases to dynamic fluxes caused by voltage transients inducted upon first phase energization [8]. For illustration, a three-phase transformer with a typical remanence flux pattern of 0.0 p.u. 0.6 p.u. and -0.6 p.u.is presented in Figure 4.1. When optimal energization occurs on phase A at zero remanence flux, the resultant dynamic core flux on two other phases is divided unevenly. This behavior is referred to as dynamic flux due to which phase C flux progresses towards saturation knee point while phase B flux stays in the linear region [8]. As core inductance is proportional to slope on flux and current curve, voltages on these two windings evolve unequally, i.e. a higher voltage appearing across the larger inductance of phase B which in turn elevates its flux level toward the magnitude of phase C flux [8]. This phenomenon, identified as core flux equalization and limited to transformer with a three-limb core or a delta winding connection, forces fluxes to rapidly equalize and eliminates the effect of remanence fluxes in phases B and C [8].

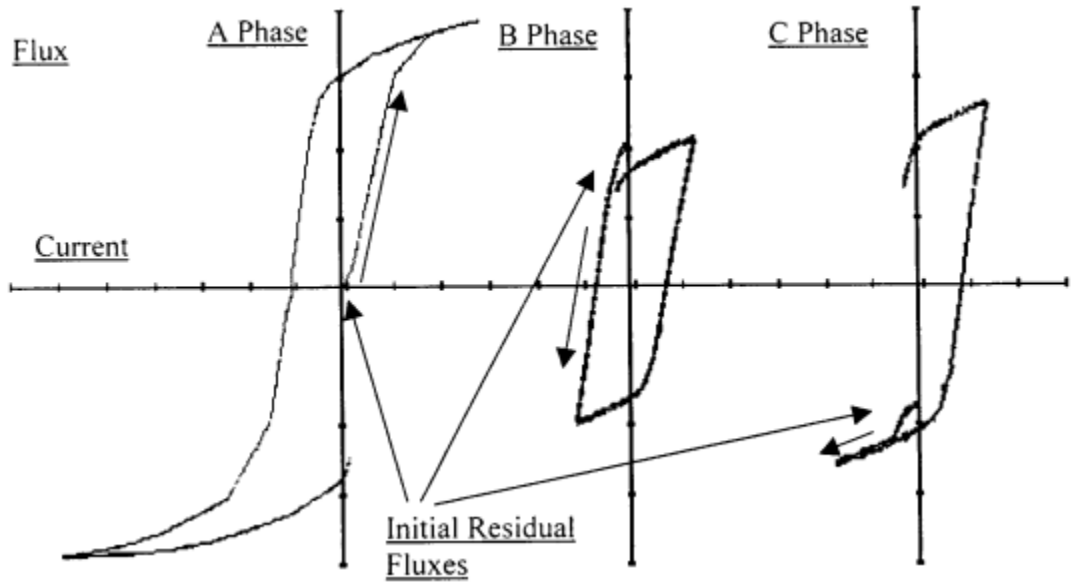

Figure 4.1 Flux equalization (three-limb core or delta-winding connection) [8]

As demonstrated in Figure 4.2, controlled switching with a delayed closing strategy closes one phase first and remaining two phases a few cycles later when their fluxes become half the magnitude and 180 degrees out of symmetrical flux on the first optimally energized phase [8]. Although a few other strategies have been proposed for controlled switching multi-phases transformers, in reality only delayed closing strategy is feasible for three-phase transformer applications due to prohibitive computation and complication of dynamic fluxes [8].

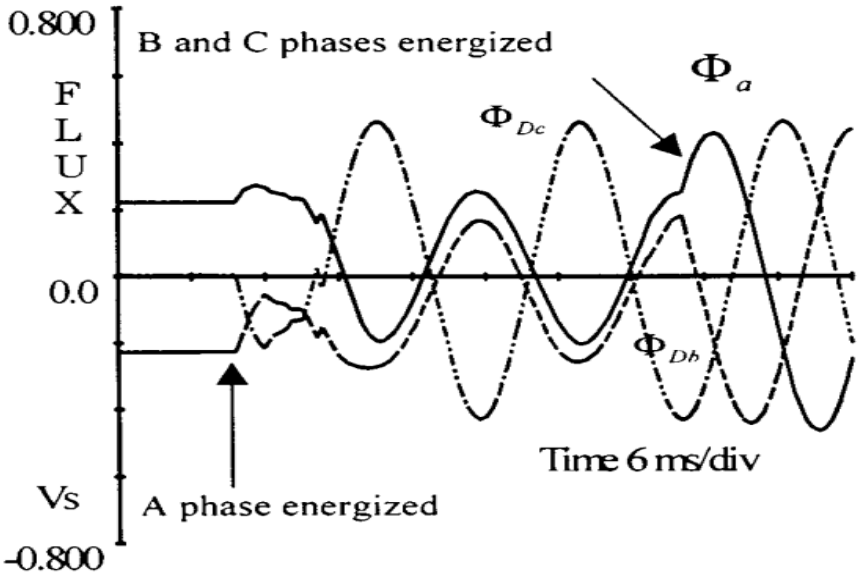

Figure 4.2 Delayed closing strategy and dynamic fluxes [8]

(three-limb core and a delta-connected winding)

Based on the delayed closing strategy, a user defined component is developed in PSCAD/EMTDC which measures the remanence fluxes by integrating transformer winding voltages in a definite time window upon de-energization. It then closes first breaker phase at an optimal instant calculated using Equation (4.3) and several electrical cycles later followed by simultaneous closing of other phases once in synchronization with source voltages.

$$t_{optimal} = \begin{cases} \dfrac{\pi + \cos^{-1}\left(\Phi_{remanence\ p.u.}\right)}{\omega} & if\ \Phi_{remanence\ p.u.} \geq 0 \\ \dfrac{\pi - \cos^{-1}\left(\Phi_{remanence\ p.u.}\right)}{\omega} & if\ \Phi_{remanence\ p.u.} < 0 \end{cases} \tag{4.3}$$

where $t_{optimal}$ optimal closing instant after synchronizing with source voltages (s),

$\Phi_{remanence\ p.u.}$ per-unitized remanence flux calculation (p.u.),

ω source voltage angular speed (rad/s).

4.3 Circuit Breaker with Pre-Insertion Resistors

A pre-insertion resistor (PIR) combined with an auxiliary breaker can be installed in parallel to a circuit breaker. It is deliberately inserted in electrical network by closing auxiliary breaker contact for a typical duration 10 ms before closing the main breaker contacts hence effectively removing the PIR by short-circuiting it. Modern modularized PIRs designed for SF6 breakers rated 230kV and above are of about 400 ohms – equivalent to the surge impedance of a 230kV transmission line.

As winding cores exhibit nonlinearity depending on the flux trajectory, by strategically placing a large resistor in series with this nonlinear winding inductor for a sufficient duration, the voltage that would have driven transformer core into heavy saturation region is depleted from the wound core and dynamically transitioned across PIR. This process prevents core flux from entering heavy saturation till it returns to unsaturated region. For effective inrush current reduction, value of PIR and insertion duration must be judiciously selected [9]. A conceptual illustration of PIR and a simplified transformer representation is given in Figure 4.3.

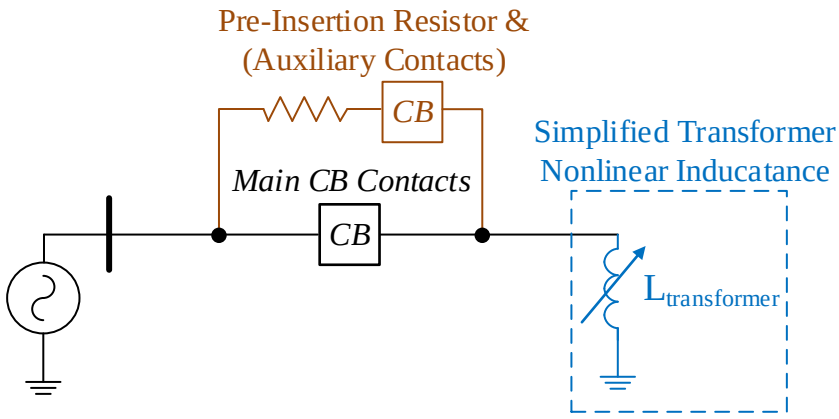

Figure 4.3 Conceptual illustration of breaker PIR and transformer nonlinear inductance

4.4 Three-Phase Five-Limb Transformer Model with Hysteresis Representation

4.4.1 Magnetic Electric Equivalent Circuit (MEEC) Three-Phase Five-Limb Transformer Model

A three-phase five-limb transformer component referred to as Magnetic Electric Equivalent Electric Circuit (MEEC) model based on the topological Hybrid concept has been developed in PSCAD/EMTDC by HVDC Research Centre [83]. This model considers core topology with direct entries of physical dimensions as shown in Figure 4.4 and accounts for hysteresis characteristics by J-A model. Leakage inductance matrix is externally formed and is connected to hysteretic duality deduced topological core representation via a fictitious infinitely thin coil at the surface of core branches [51], [52].

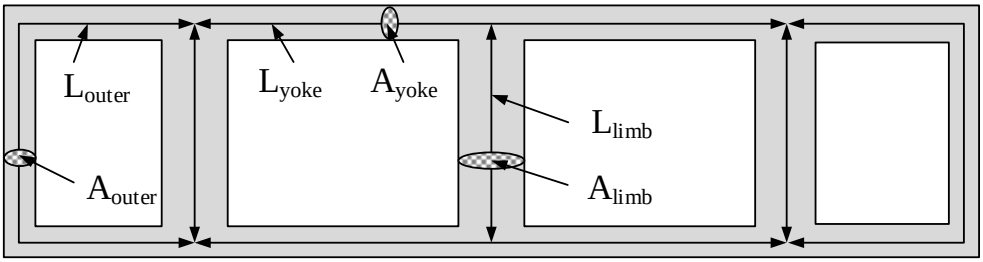

L_{outer} = Outer Limb Length
A_{outer} = Outer Limb Average Area
L_{yoke} = Yoke Section Length
A_{yoke} = Yoke Section Average Area
L_{limb} = Wound Limb Length
A_{limb} = Wound Limb Average Area

Figure 4.4 Three-phase five-limb MEEC transformer core geometry

Applying classical magnetic circuit theory, a five-limb MEEC transformer core can be discretized into aggregated magnetic elements as conceptualized in Figure 4.5. It assumes

that core is assembled from the same ferromagnetic material with a homogeneous permeability and magnetic fluxes and is uniformly distributed and confined [50], [84].

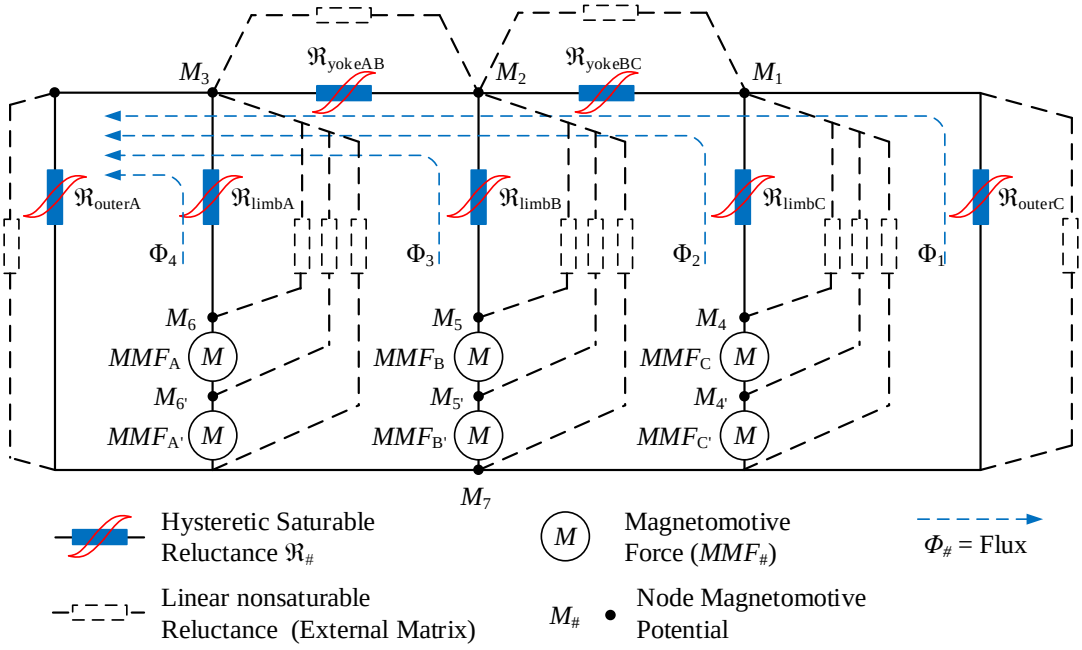

Figure 4.5 Conceptualized five-limb MEEC transformer magnetic circuit

With magnetic and electric analogous relations summarized in Table 4.1, a dual electric circuit is deduced graphically using the duality principles [84].

Table 4.1 Magnetic and electric dual analogies

Magnetic Quantities	**Electric Quantities**	**Governing Laws**
Magnetomotive Force (MMF)	Current (i)	Ampere's Law ($MMF = Ni$)
Rate of Flux Change ($d\Phi/dt$)	Voltage (V)	$V = d\Phi/dt$
Reluctance ($\Re$)	Inductance (L)	$L = N^2/\Re$ $= (\mu N^2 Area)/Length$
Parallel Connection	Series Connection	Graphical Duality
Series Connection	Parallel Connection	
Node (KCL)	Mesh (KVL)	Maxwell's Equations
Mesh (KVL)	Node (KCL)	

Existing saturable inductor model is composed of a static J-A hysteresis model current injection and two resistors representing the classic and excess eddy current losses thus frequency-independent. In comparison, the improved model incorporates the modified dynamic inverse J-A hysteresis model with frequency-dependency current injections as shown in Figure 4.6 to avoid unnecessary computational expensive admittance matrix inversion and triangulation at each time step.

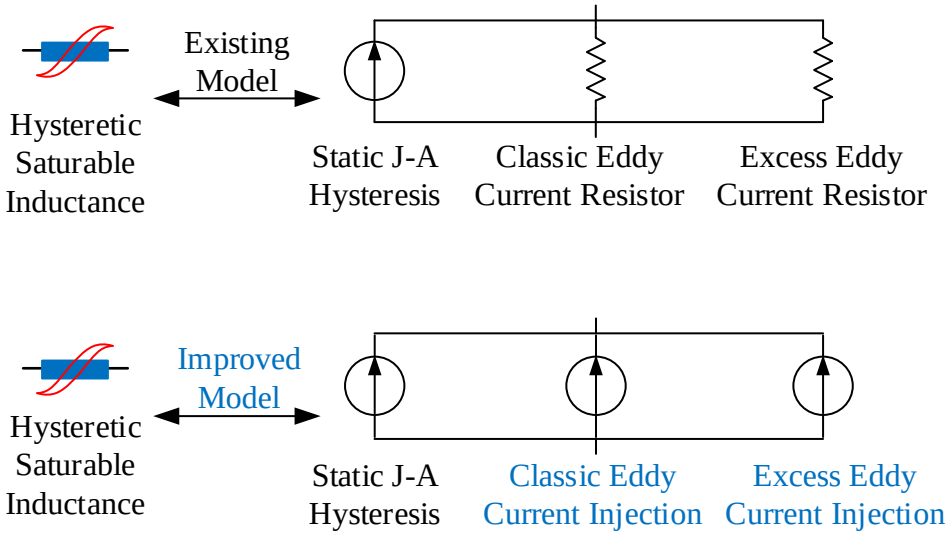

Figure 4.6 Improved hysteretic saturable core branch representation

In PSCAD, as illustrated in Figure 4.7 fictitious transformer windings are introduced to facilitate connections to the external leakage circuit representation. When solving the equivalent dual electric core circuit at each solution time step, an iterative method is used to ensure convergence of all unknown quantities.

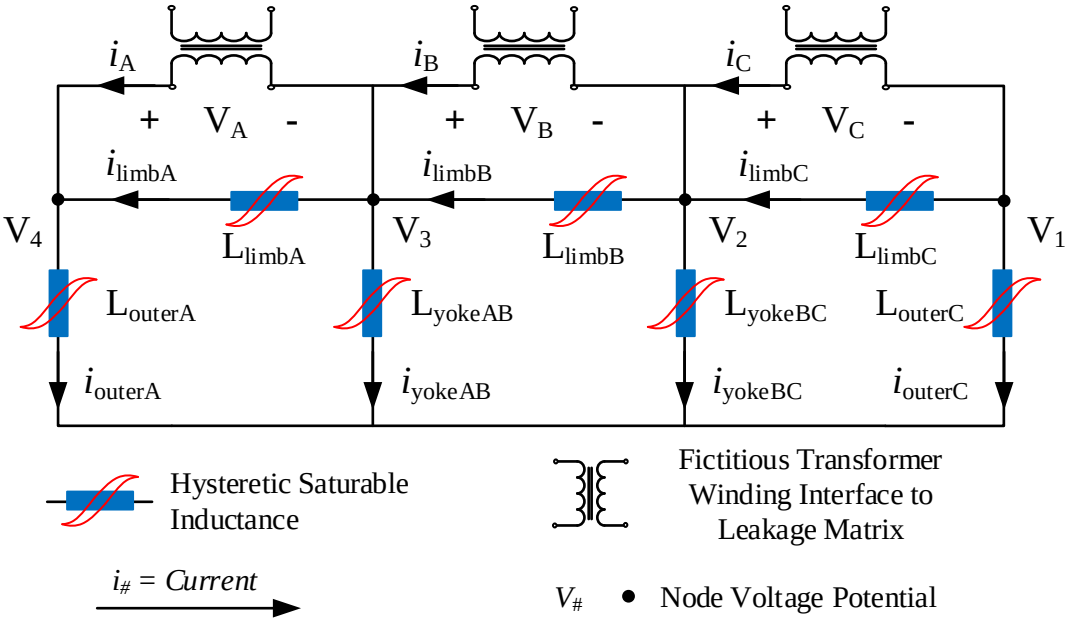

Figure 4.7 Equivalent electric circuit of 5-limb core transformer (duality theory)

4.4.2 Efficient J-A Hysteresis Numerical Solution Algorithm

In EMT power transformer models, solving saturable core hysteresis is a nontrivial problem where magnetic induction B is directly calculated by integrating winding voltages and finding the corresponding field strength H through an iterative numerical solution procedure. Reference [49] proposes a technique that translates this into a confined search problem which executes J-A model differential equations to reduce incremental susceptibility dM/dH error by varying a search index Q. The magnitude of Q is iteratively refined successively by the following equations with an objective to converge dM/dH and this non-trivial and nonlinear numerical process is repeated for all core branches in the equivalent electric circuit [49].

$$\Delta\Phi_i = \frac{V_i^{new} + V_i^{old}}{2}\frac{\Delta t}{N_i} \tag{4.4}$$

$$\Delta H_{imax} = \frac{\Delta\Phi_i}{Area_i \mu_0} = \frac{\Delta B_i}{\mu_0} \tag{4.5}$$

$$\Delta H_i = Q\Delta \mathrm{H_{imax}} \quad where\ (0 \le Q \le 1) \tag{4.6}$$

$$\Delta M_i = \frac{\Delta \mathrm{B_i}}{\mu_0} - \Delta H_i \tag{4.7}$$

$$H_i = H_{oldi} + \Delta H_i \tag{4.8}$$

$$M_i = M_{oldi} + \Delta M_i \tag{4.9}$$

where i = transformer winding number,

$\Delta\Phi_i$= incremental flux in the present time step,

V_i^{new} = present value of voltage in the i^{th} winding,

V_i^{old}= value of voltage in the i^{th}winding in previous time step,

Δt = time step,

N_i = number of turns in the i^{th}winding,

ΔH_{imax} = maximum magnitude of incremental flux intensity in i^{th} winding,

$Area_i$ = cross section area of i^{th} winding limb,

ΔB_i = incremental flux density in i^{th} winding,

μ_0 = permeability in vacuum,

ΔM_i = incremental magnetization in i^{th} winding,

H_i & H_{oldi} = flux intensity values of present and previous time step, respectively,

M_i & M_{oldi} = magnetization values of present and previous time step, respectively.

Equations (4.4) and (4.5) show that flux and flux density can be readily calculated from winding voltages at each time step. Inverse J-A model directly relates the incremental magnetization and flux density by dM/dB and benefits from such observation. When initialized with a well contemplated estimation of Q together with numerical algorithms like Bisection and Golden Ratio methods, inverse J-A can substantially enhance computational efficiency. Newly implemented inverse J-A is demonstrated in Figure 4.8 to reach a smaller convergence target much more rapidly than that of the existing J-A algorithm. About 95% of inverse J-A solution takes less than 5 iterations and yields smaller convergence errors in comparison to that only 2% of the existing J-A solutions converges before reaching the pre-defined maximum number of 25 iterations yet in general produce larger convergence errors.

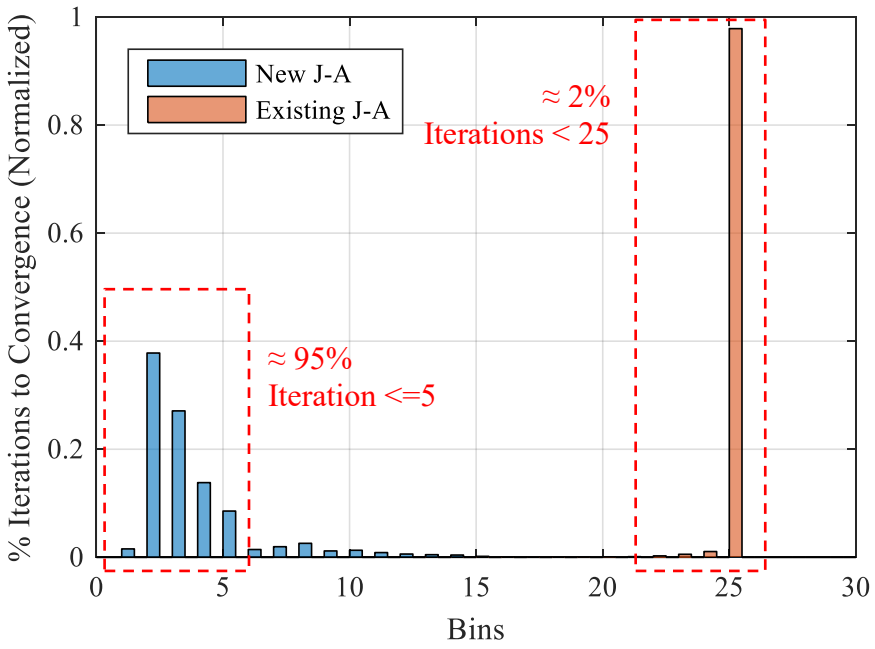

(a) Computation efficiency of existing and new J-A solution algorithm

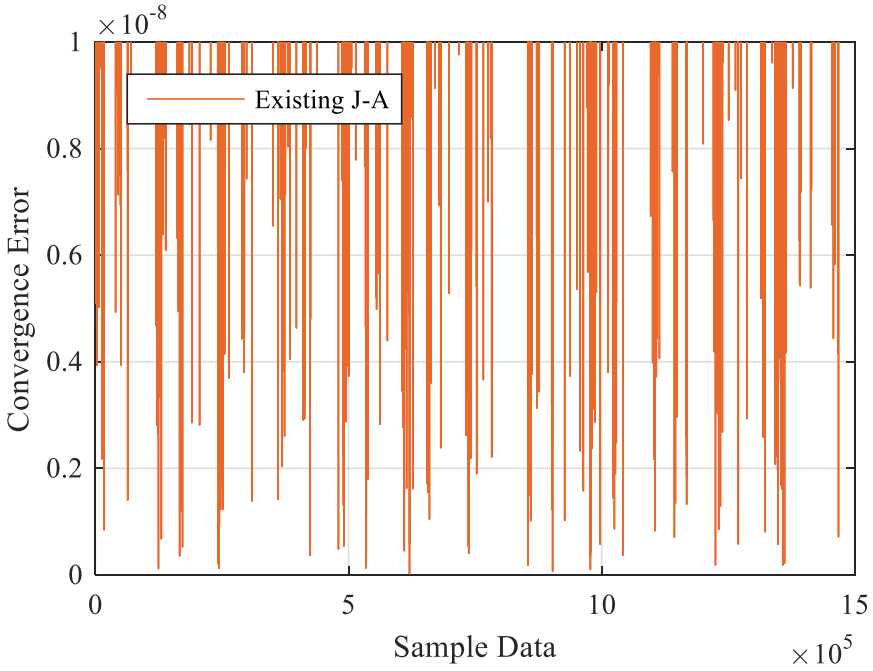

(b) Convergence error of Q (existing J-A model solution algorithm)

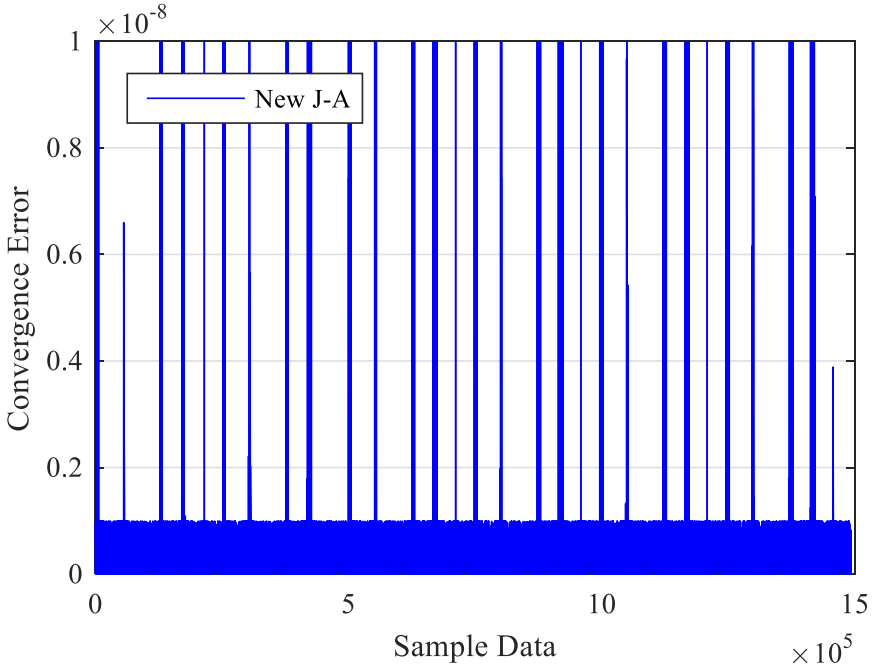

(c) Convergence error of Q (new inverse J-A model solution algorithm)

Figure 4.8 Computation efficiency of new inverse J-A over existing algorithm

4.4.3 Dynamic J-A Model with Frequency Dependent Losses

According to the loss separation theory discussed in Chapter 2, frequency dependent effects of classical and excess eddy currents can be appended to the calculated field intensity H for all saturable core sections at the end of each iteration in PSCAD. As explained in Chapter 3, an empirical trial and error approach has been employed in PSCAD for identification of eddy current related coefficients since only a graph of measured 50Hz hysteresis loops at 1.0T, 1.5T and 1.7T for a 23 mm M3 grade DR GOES compatible material has been made available. If lamination geometry and recorded time-series waveforms of this material are provided, those coefficients can be estimated and optimized by the constrained multi-objective PSO procedure proposed in Chapter 3.

A good agreement of hysteresis loops at 50Hz between PSCAD calculated and measured has been obtained by starting with coefficient values of M4 grade GOES material published in [49] and gradually reducing them through trial and error. By steel grade classifications, M3 grade GOES dissipates less core loss than M4 grade counterpart so M4 eddy current coefficients are scaled by a ratio of these core loss at beginning. Initial fitness reveals a good accuracy on loop width but a slight disparity of orientational rotation between the calculated and measured hysteresis loops at 50Hz, which agrees with the phenomena observed in [49]. Hysteresis loop orientational rotation is dominated by the inter-domain coupling parameter α; therefore, parameters of the modified inverse J-A model have been slightly adjusted for optimal accuracy while retaining good fitness on magnetization curve characteristics. Final optimized hysteresis loops and magnetization curve are compared with the measured quantities in Figure 4.9.

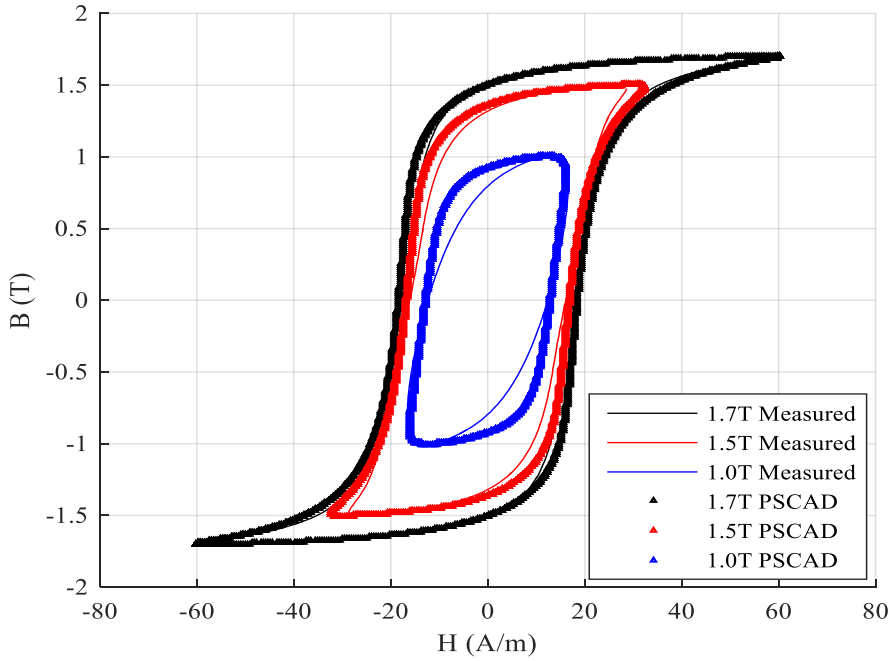

(a) Measured and calculated hysteresis loops at 50 Hz

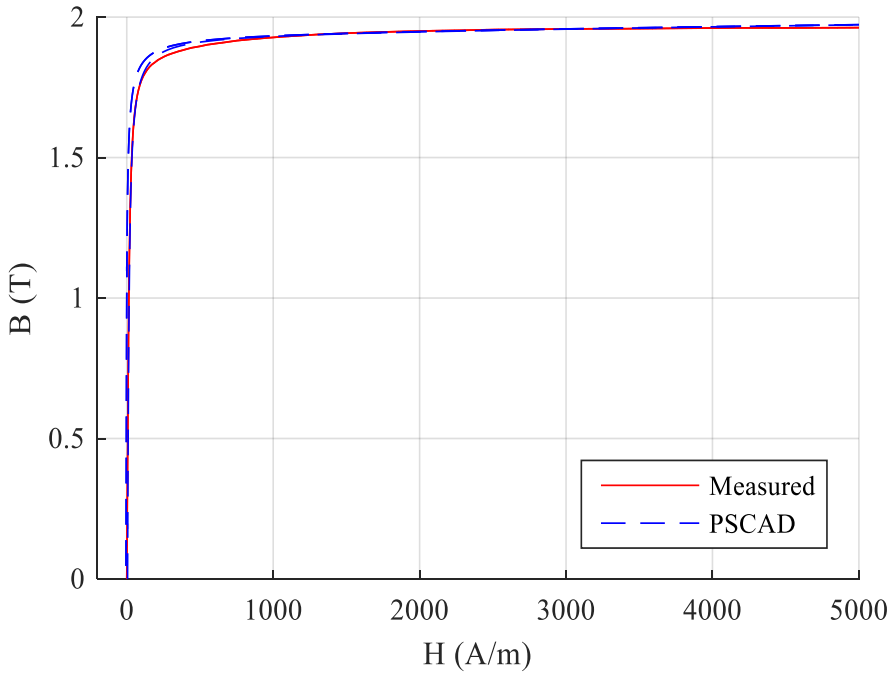

α	c	k_s	M_s	a_1	a_2	a_3	pk_1	pk_2	k_1	k_2
5×10^{-6}	0.3	7.8	1.69×10^{6}	2.4×10^{4}	2.7×10^{4}	2.3×10^{5}	31.7	4.8	6×10^{-3}	0.33

(b) Measured and calculated magnetization curve and refined J-A model parameters

Figure 4.9 B-H loops and curve fitness
(modified J-A model with variable k & optimally adjusted parameters)

By maintaining the same voltage and frequency ratio at different voltage frequencies in PSCAD, a series of calculated hysteresis loops of a transformer core branch is plotted with an identical flux density level in Figure 4.10 to illustrate the frequency dependent nature of dynamic J-A model. Figure 4.11 presents an overview of both dynamic and static J-A model calculations from PSCAD in comparison to the measurements.

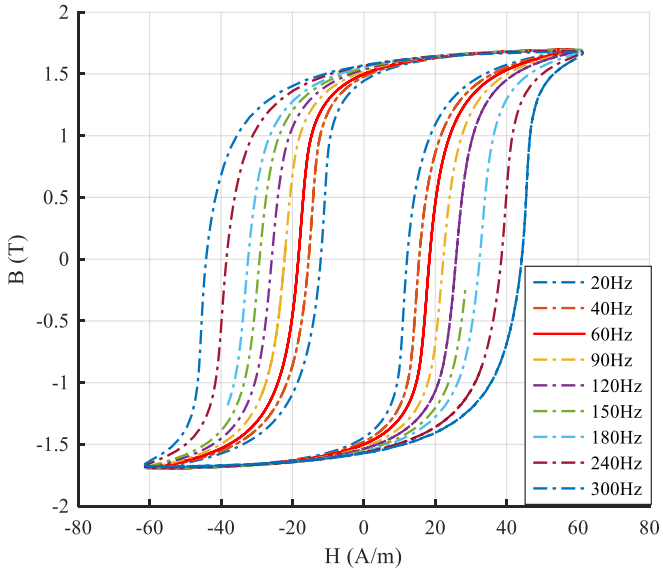

Figure 4.10 Frequency dependent behavior of dynamic inverse J-A model in PSCAD

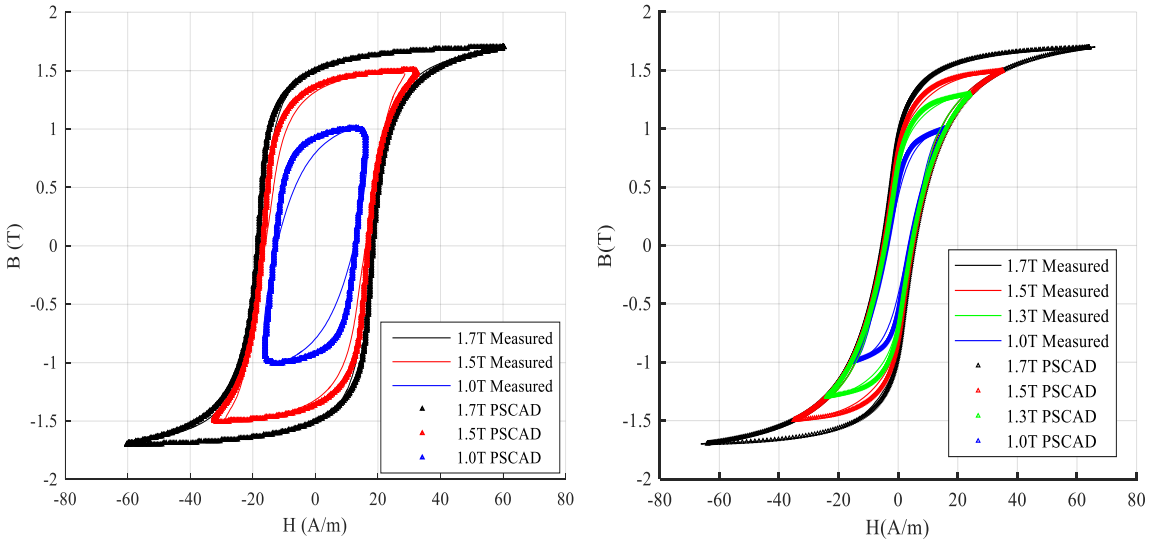

Figure 4.11 Dynamic and static J-A model in PSCAD comparison to measurements

Now with the improved J-A model incorporated into the MEEC transformer model in PSCAD, the merits of accurate hysteresis characteristic can finally be illustrated and appreciated. In Figure 3.14 of Chapter 3, a variable pinning k was proposed to replace the constant k and was demonstrated to significantly improve the overall description of hysteresis prediction, especially near regions related to the remanence. Hysteresis trajectories calculated by J-A model with constant k generally suggested smaller remanence fluxes than that of the J-A model with variable k.

In PSCAD, comparative simulations of a three-phase five-limb MEEC transformer de-energization followed by a subsequent energization for inverse J-A model with a constant pinning k versus the proposed variable pinning k were conducted. In Figure 4.12, given identical breaker opening instants in these two simulations, transformer winding voltage waveforms remain relatively identical but the remanence fluxes calculated on respective phases show visible differences, where remanence fluxes are higher for J-A model with variable pinning k. This manifest into more elevated inrush currents during the subsequent transformer energizations for these two models when the circuit breaker closes at exactly the same instants on source voltage waveforms in the two simulations.

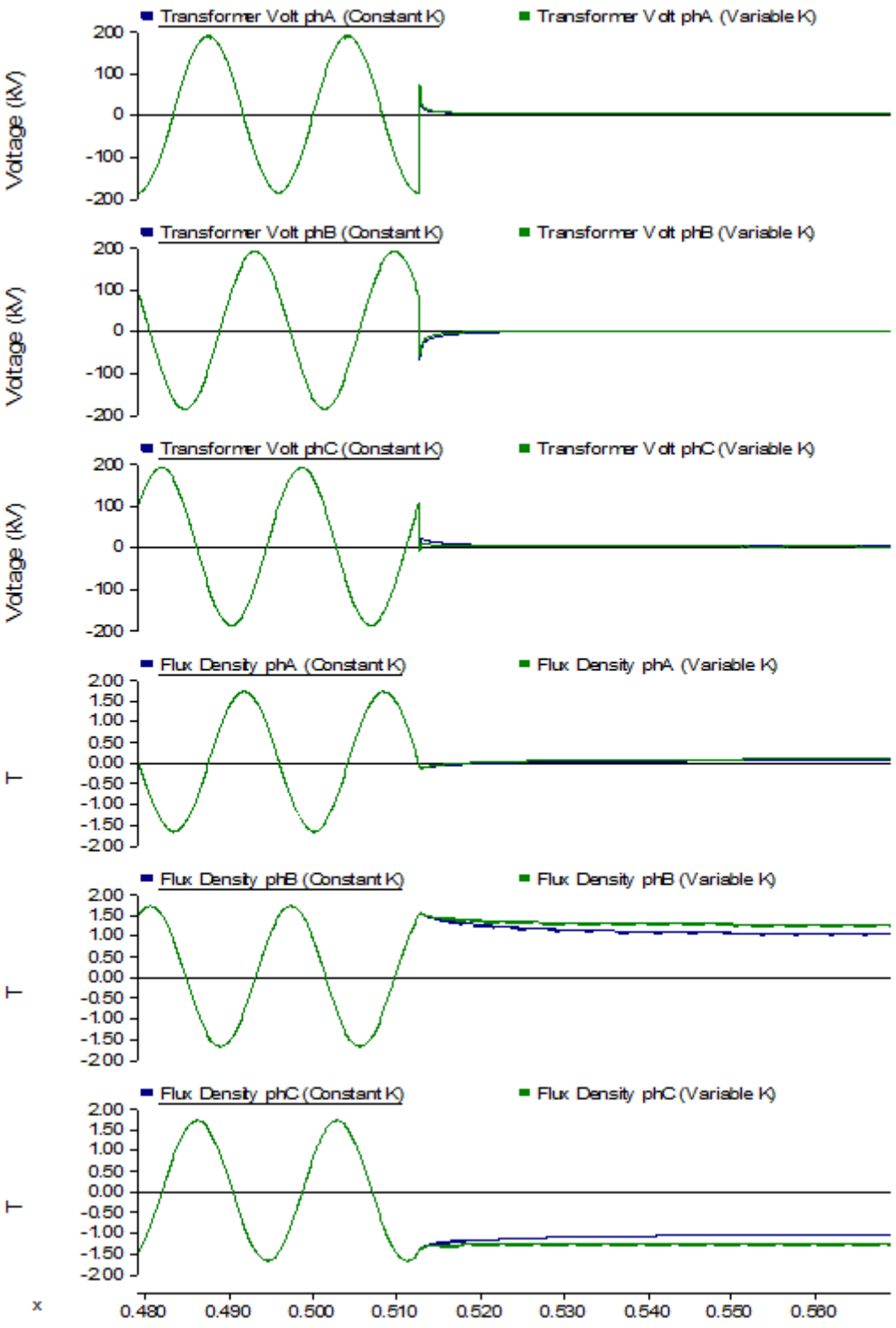

(a) Transformer winding voltages and flux densities during a de-energization

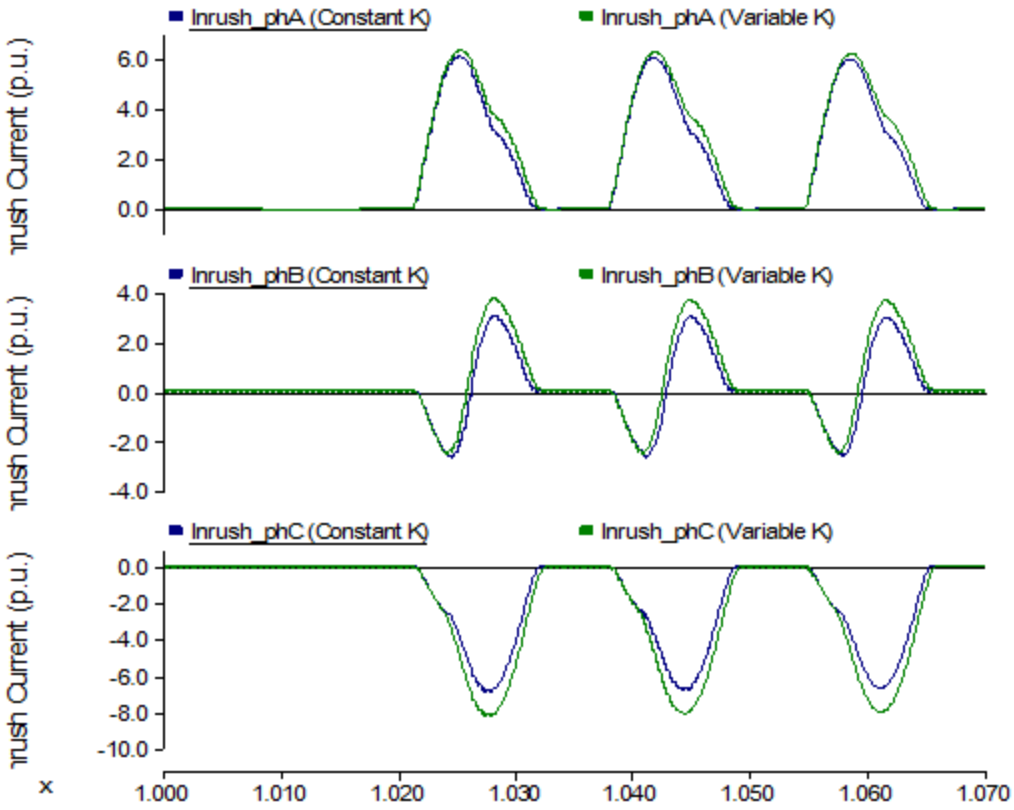

(b) Transformer inrush current waveforms during a subsequent energization

Figure 4.12 Comparison of J-A model with a constant pinning k versus the proposed variable k and effects on transformer flux predictions and inrush current

Power transformer core is assembled from thin laminations of GOES material, and it is rational to assume homogenous ferromagnetic properties of B-H hysteresis loops and magnetization curve characteristics [84]. Conventional transformer saturation behavior is expressed by a flux and current relation, which is different on core branches by geometry but proportional to the same magnetic properties by equations

$$\Phi = \mathrm{B}\times\mathrm{A} \tag{4.10}$$

$$Ni = H\times l \tag{4.11}$$

where Φ = flux (Wb)

B = magnetic induction (T)

A = core cross section area (m^2)

N = number of winding turns

i = current (A)

H = magnetizing force (A/m)

l = flux path length (m)

4.5 Concluding Remarks

In this chapter, the fundamental theory of inrush current elimination by controlled switching unloaded power transformers was reviewed, and for comparison the working principle of circuit breaker PIR was presented.

The concept of a new three-phase five-limb hybrid transformer MEEC model developed by HVDC Research Centre was reviewed. This model properly represented the core structure and magnetic interaction between different limbs. It consolidated strengths of leakage inductance matrix and a topologically correct core represented by a magnetic equivalent electric circuit using duality principle. To improve the accuracy and overall description of core magnetic behaviors, the modified inverse J-A model with variable pinning parameter k proposed in Chapter 3 was successfully incorporated into MEEC. A novel numerical solution algorithm was developed to significantly improve computation efficiency of inverse J-A model over the existing algorithm. The frequency-dependent effects due to classic and excess eddy current were implemented and was turned and validated against measurements taken at 50Hz. Given limitation of data available, tuning of eddy current loss coefficients were done by trial and error technique and was seen to yield results in good agreement to the measurements.

Chapter 5

Controlled Switching Studies: Systematic Analysis and Considerations

In this chapter, a systematic analysis that compares inrush current reduction performance of controlled switching and pre-insertion resistor on parallel-operated five-limb converter transformers pair energization is conducted. Effects of practical considerations, such as circuit breaker current chopping and pole scatter effects and HVDC on-load tap changer (OLTC) movements, are also investigated.

5.1 Systematic Analysis of Controlled Switching Five-Limb HVDC Converter Transformer Pair

5.1.1 System Model Description

Currently, an off-the-shelf 230kV commercial AC circuit breaker has a guaranteed open time of 2 or 3 cycles while response time of HVDC protection and control to form a bypass pair is generally in milliseconds window, thus much faster. Therefore, it is justified to investigate switching transients of unloaded converter transformer pair assuming valve groups are blocked and bypassed. Actual data of five-limb converter transformers recently installed in Manitoba for a newly constructed LCC HVDC transmission system has been applied in PSCAD/EMTDC.

Circuit breaker current chopping feature has been enabled in PSCAD to permit arbitrary openings instead of current natural zero crossings and different remanence flux patterns on respective winding core limbs. Modern SF6 circuit breakers exhibit a tendency to chop small inductive magnetizing currents (milli-ampere range) of unloaded power transformer de-energization due to limited withstand capability of breaker insulation media [85]. Breaker open and close commands are issued at 15 electric degree increments from 0 to 360 degrees on the rising voltage zero transition of phase A source voltage. Breaker contacts open when currents are less than a current chopping threshold and close at instants dictated by mitigation philosophies as shown in Figure 5.1.

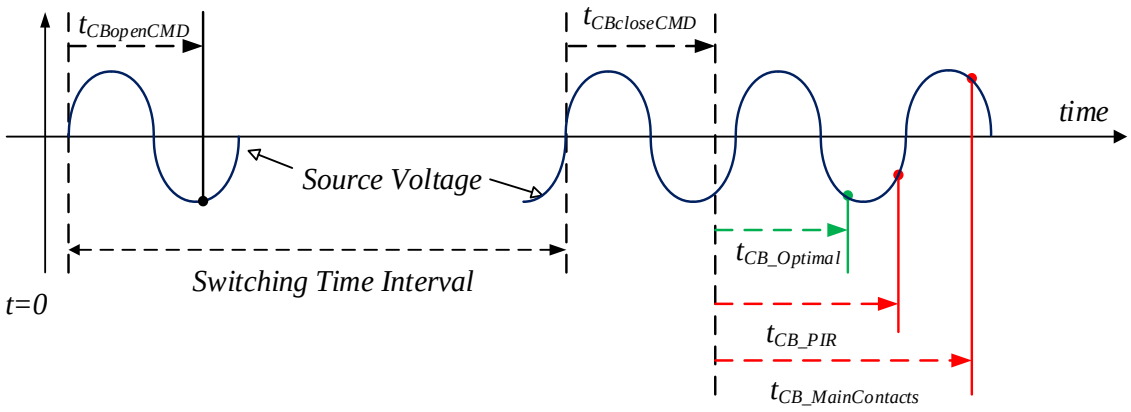

$t_{CBopenCMD}$ = *Breaker Open Command*

$t_{CBcloseCMD}$ = *Breaker Close Command*

} *Circuit Breaker Operating Command Ranging from 0 to 360 electric degrees at increment of 15 degrees*

Breaker Closing Instant : (Controlled Switching or Breaker Pre-Insertion Resistor)

Either $t_{CB\_Optimal}$ = *Calculated Controlled Switching Optimal Closing Instant*

Or

t_{CB_PIR} = *Breaker Pre-Insertion Resistor (PIR) Insertion Duration*

$t_{CB\_MainContacts}$ = *Breaker Main Contacts Closing Instant & PIR Removal*

Figure 5.1 Systematic switching process for circuit breaker opening and closing

The parallel-operated converter transformer pair is first operated by a single AC circuit breaker systematically with no mitigation just to establish a base line of resultant inrush currents. This is repeated with controlled switching device with a delayed closing strategy that issues an optimal closing signal on the first phase followed by closing two remaining phases at the first rising voltage zero transition 4.5 cycles after the 1st phase closing [20]. Remanence flux is calculated by phase voltage integration during transformer de-energization and an optimal closing instant is predicted as depicted in Figure 5.2. Lastly, breaker PIR with a typical 230kV 400 ohms and 10ms insertion time on inrush current reduction is evaluated in comparison to controlled switching remedy.

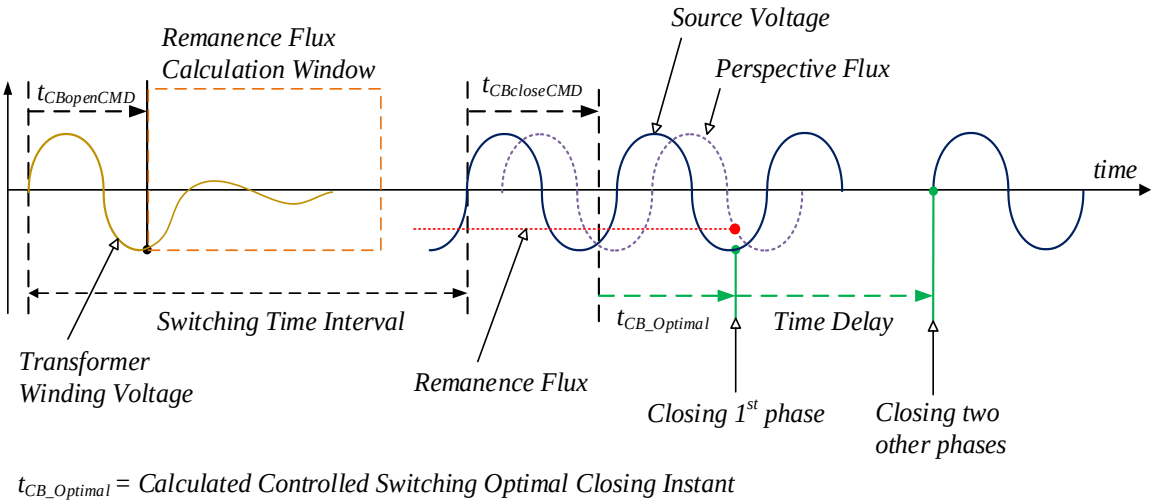

Figure 5.2 Depiction of controlled switching and remanence flux calculation

Figure 5.3 shows these three switching study scenarios of unloaded converter transformer pair with different inrush current mitigations. To help in visualizing the inrush current peak magnitude variation as a function of the opening and closing times, a three-dimensional (3D) pattern illustration supplemented by a 2D contour plot are given [26].

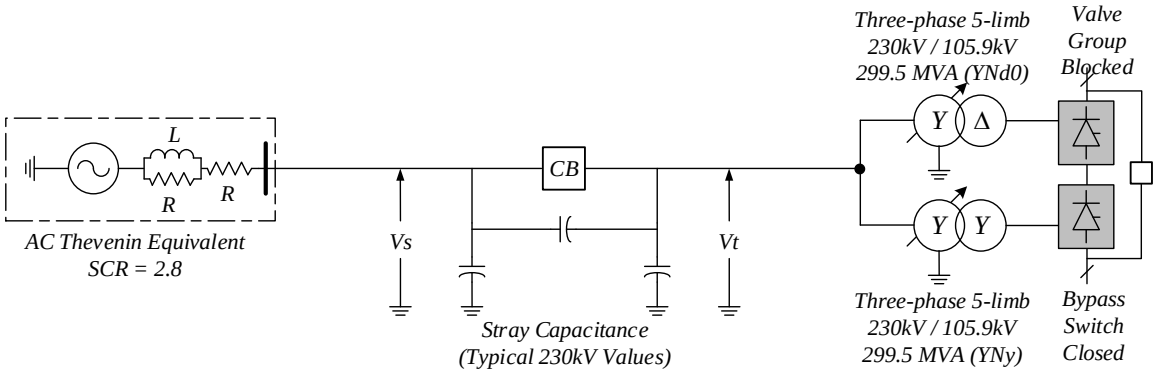

(a) Single breaker switching with no mitigation

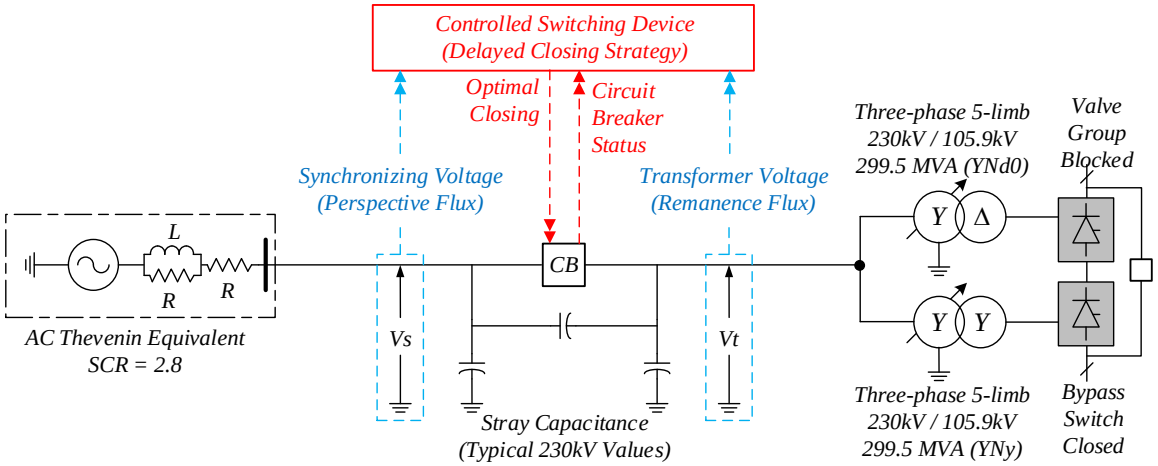

(b) Single breaker switching with controlled switching

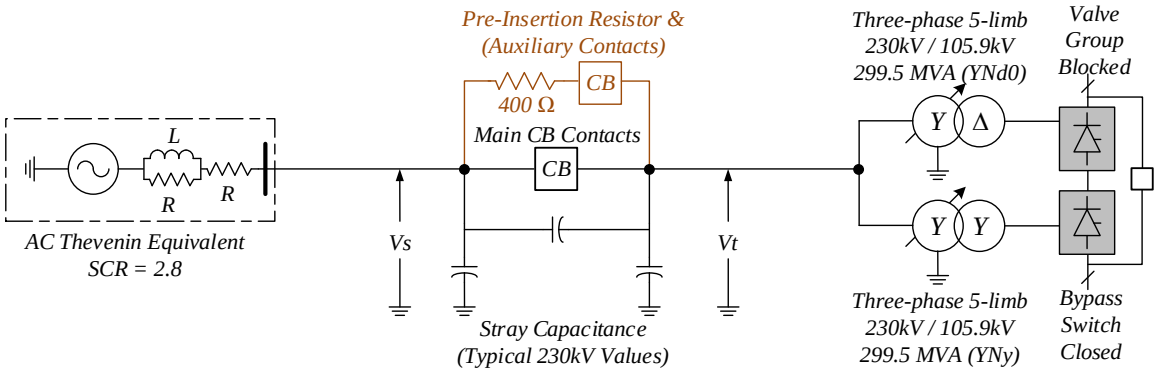

(c) Single breaker switching with pre-insertion resistor

Figure 5.3 Converter transformer pair energization with different mitigations

A summary of system and component data considered has been summarized in Table 5.1.

Table 5.1 Study simulation system data summary

AC Thevenin Equivalent Strength	
Short-Circuit Ratio (SCR) on 2000MW base	2.8
AC Circuit Breaker	
Current chopping threshold	3 mA ≤
12-Pulse Converter Transformer	
Rating	230 kV/105.9 kV, 299.5 MVA
Commutation reactance	18%
Core construction	three-phase five-limb
Core ferromagnetic material	23 mm M3 Grade GOES
Inrush current per-unit base value	1.5 kA (pair together)
On-load tap changer (OLTC) turn ratios	100% at Tap 26 & 139% at Tap 1
YNd1 (wye grounded & delta lagging)	
Yoke / limb length aspect ratio	1.43
Yoke / limb cross-section area aspect ratio	0.57
Yoke / outer-limb length aspect ratio	0.75
Yoke / outer-limb area aspect ratio	1.00
YNy0 (wye grounded & wye ungrounded)	
Yoke / limb length aspect ratio	1.29
Yoke / limb cross-section area aspect ratio	0.57
Yoke / outer-limb length aspect ratio	0.70
Yoke / outer-limb area aspect ratio	1.00
Controlled-Switching (Remanence Estimation & Delayed Closing Strategy)	
1st energization phase	largest remanence flux phase [20]
2nd & 3rd phase closing delay	4.5 electric cycles [20]
230kV Circuit Breaker Pre-Insertion Resistor	
Resistance	400 ohms
Insertion time	10 ms
Breaker pole scatter time	+ / - 1 ms

5.2 Simulation Results and Discussions

5.2.1 No Mitigation (Baseline)

With no inrush mitigation and actual breaker related effects, excessive inrush currents up to 10 p.u. and RMS voltage depression of 0.76 p.u. are observed in Figure 5.4.

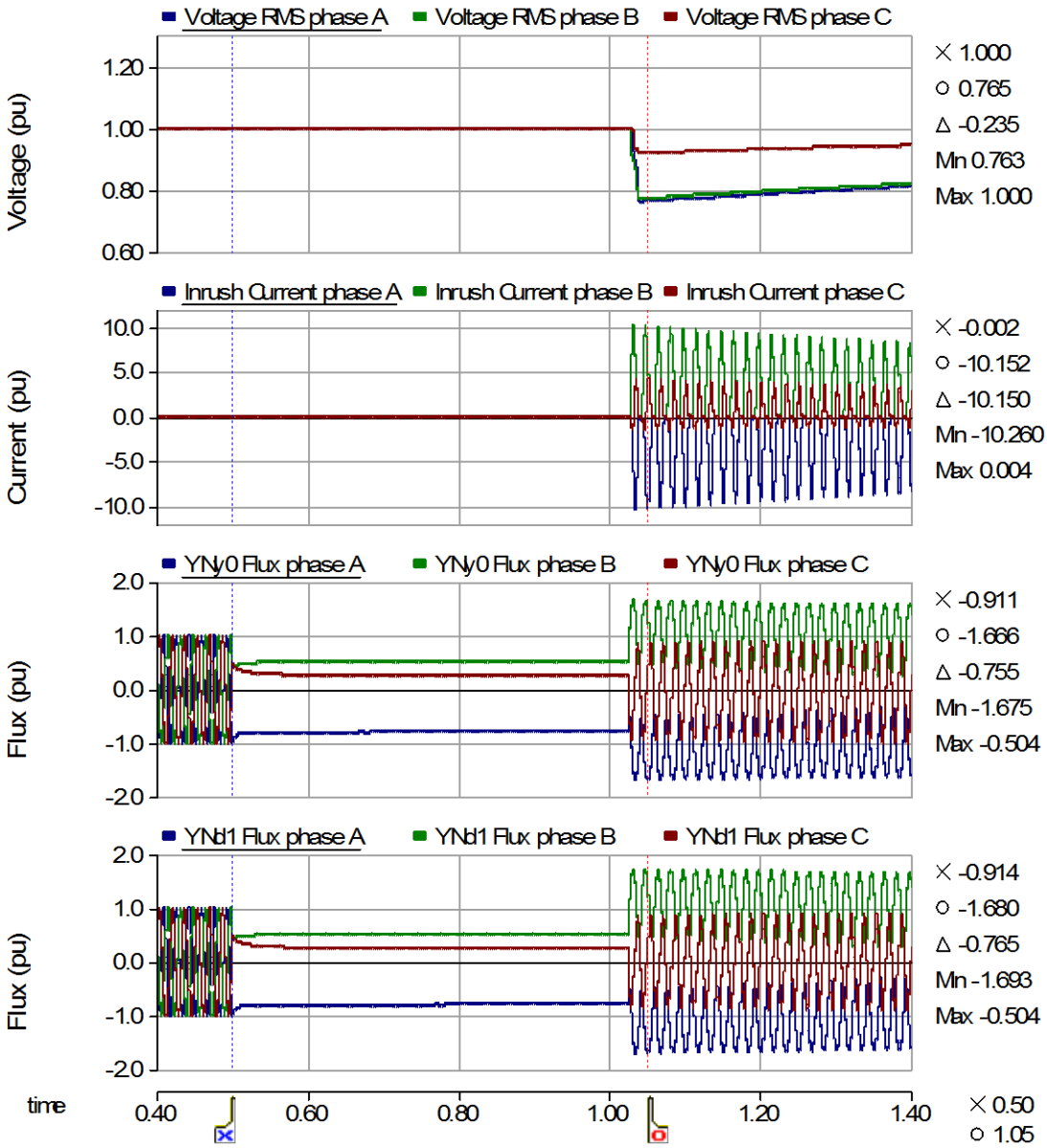

Figure 5.4 Inrush current waveforms (no mitigation example)

This is particularly pronounced if unfavorable high transformer core flux asymmetries occur, especially when the opening and closing instants are shifted from voltage zero crossing transitions by a multiple of half-cycle (or 180 degrees) as seen in Figure 5.5. Systematic switching patterns in 2D contour plot in Figure 5.6 clearly exhibit that negligible inrush currents are produced when the closing and opening instants are equal, which translates into equal remanence and perspective fluxes – an underlying principle of controlled switching. With respect to phase A, onsets of high inrush current magnitudes on phase B and C are 120 and 240 electrical degrees deferred on both opening and closing instants respectively due to the fact AC breaker switching commands are issued in reference to phase A rising zero transitions.

Statistical analysis in Figure 5.7 suggests the probability of detrimental inrush current magnitude is very likely by random switching with no remedies. This significantly increases commutation failure risks of already conducting valve groups (VG) as high inrush current cause severe depression of commutating RMS voltage, as a result causing tremendous loss in HVDC power transfers [4], [20]. The violin statistic plots in Figure 5.7 illustrate distribution, extremities and probability of inrush current on each phase. Red box highlights the median value of all recorded inrush currents.

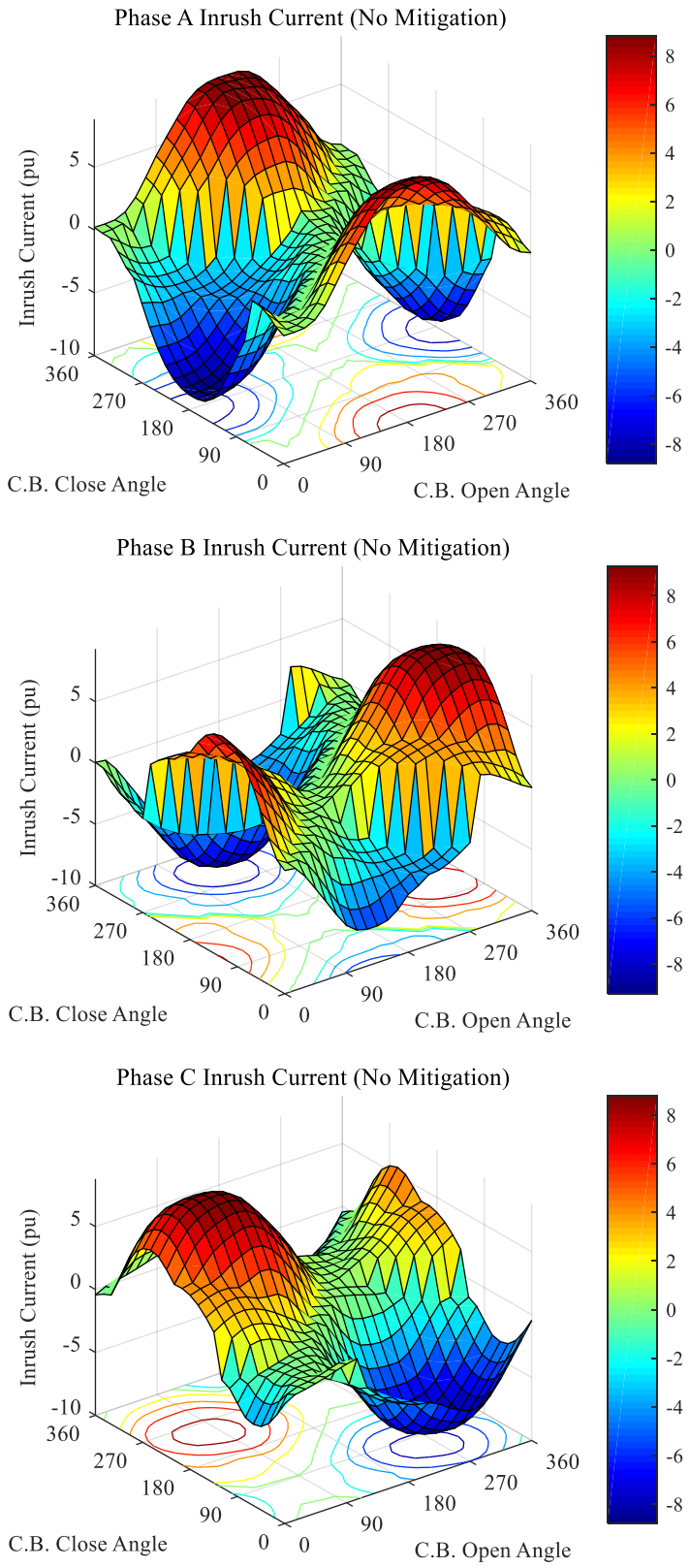

Figure 5.5 Inrush current first peaks 3D illustration (no mitigation)

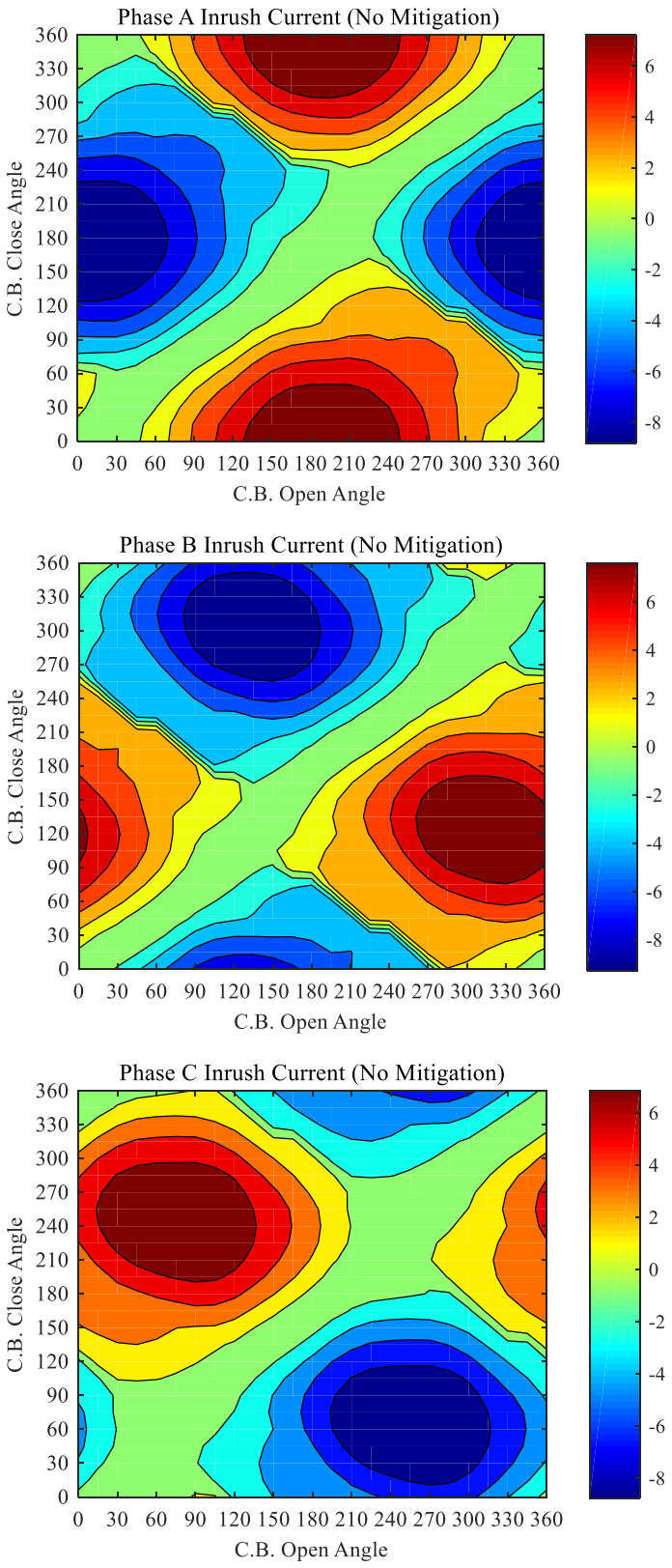

Figure 5.6 Inrush current first peaks 2D contour illustration (no mitigation)

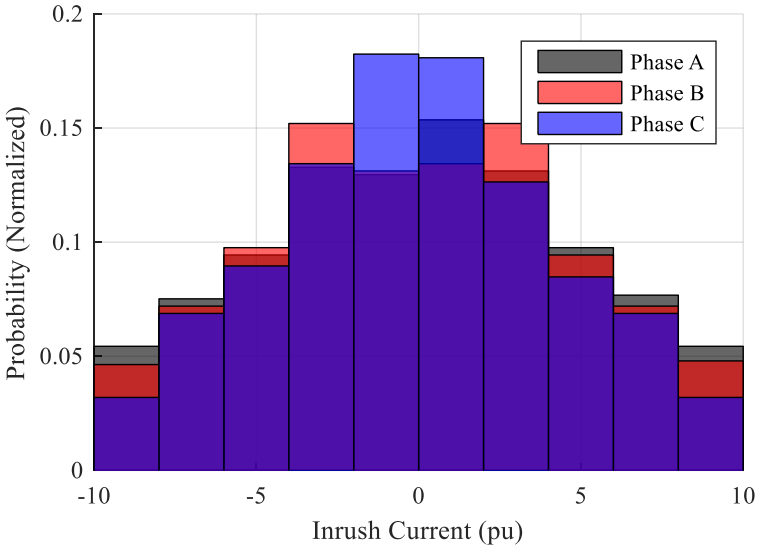

(a) Inrush current distribution

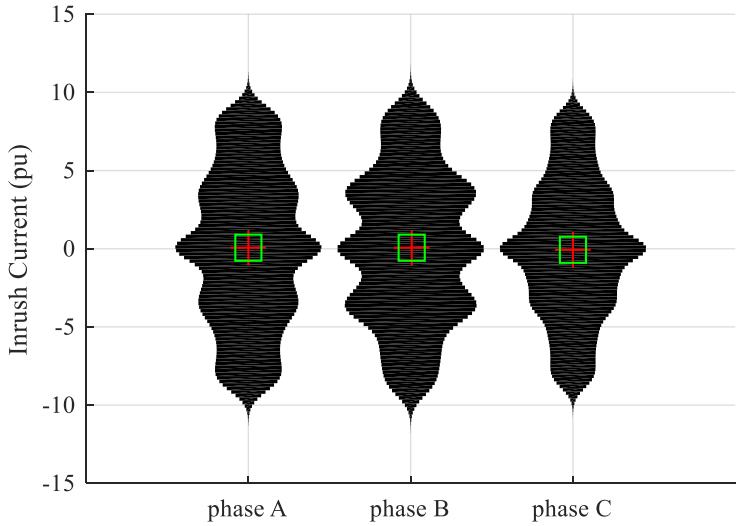

(b) Inrush current violin plot

Figure 5.7 Statistical Analysis of inrush current (no mitigation)

5.2.2 Controlled Switching (Delayed Closing Strategy)

With controlled switching accounting for remanence fluxes, the delayed closing strategy close the first phase at optimal instant followed by a 4.5 cycle delay on closing last two phases always assuming a fixed number of winding turns. It is exhibited in Figure 5.8 that inrush current and undesired RMS voltage sag can be effectively eradicated.

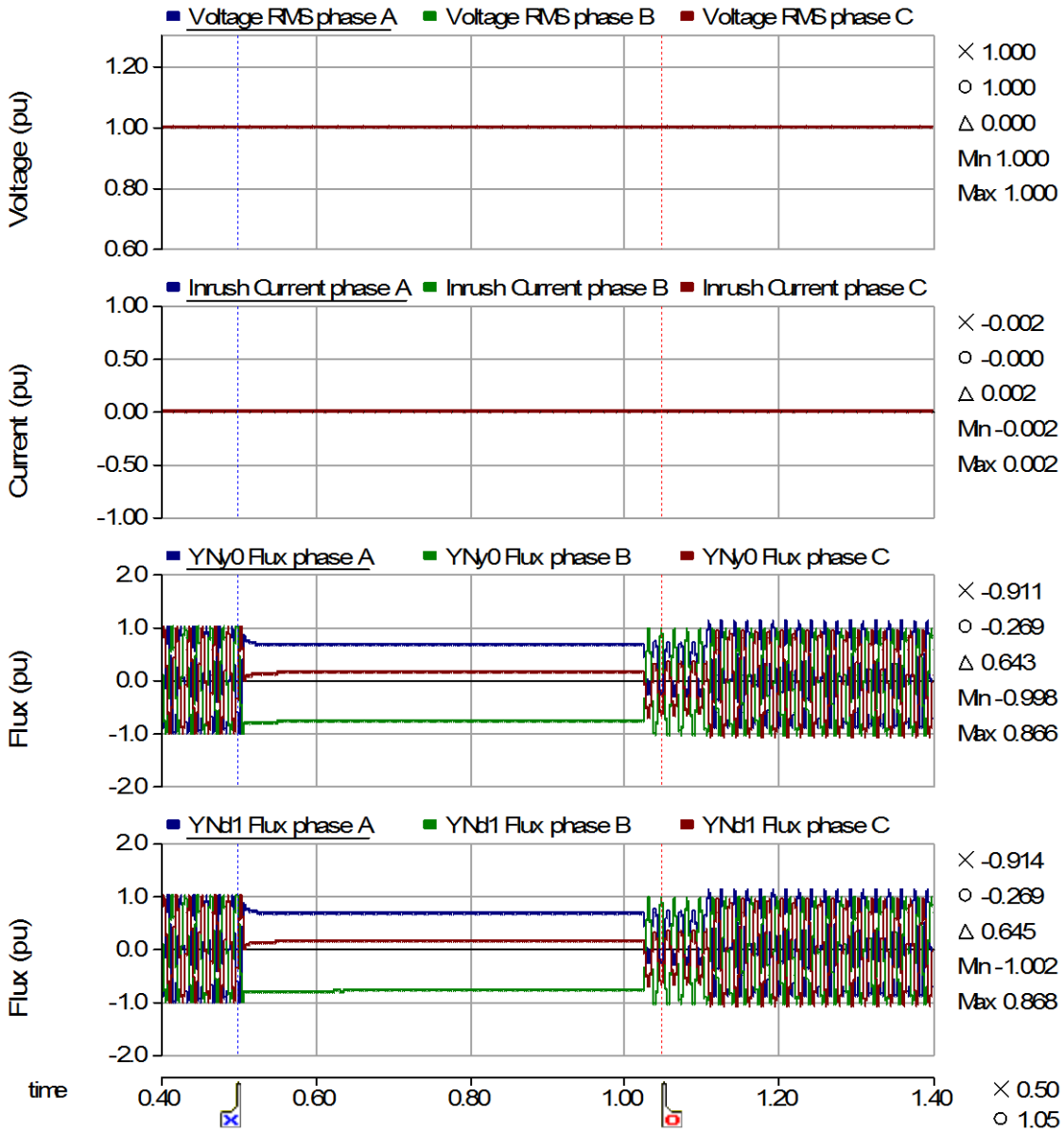

Figure 5.8 Inrush current waveforms (controlled switching example)

In general, the overall inrush current peaks of energization of converter transformer pair are substantially reduced as seen in Figure 5.9. The highest inrush current peak is now lowered to 0.25 p.u. and majority of these first peaks are less than 0.1 p.u. and negligible.

It is stated that optimal closing of the two other phases is not feasible on a five-limb transformer if no delta winding is present [51], [52]. As suggested in Figure 5.10, the single delta connection on YNd1 transformer can be perceived a virtually shared winding by both of the two parallel-operated converter transformers. It offers an electrical to magnetic coupling conduit for flux equalization required by optimal controlled switching. Typical operating practice ensures insertion and removal of 12-pulse VGs and connected converter transformers, so it can benefit from this virtual delta-winding in controlled switching.

The symmetry of sublet inrush current peaks mirrored on phase A and C with respect to phase B observed in Figure 5.11 is attributed to the physical symmetry of a five-limb core. Repeated occurrences of these minor inrush currents at opening angles of 115 and 285 degrees regardless closing angles happen during energization of the two remaining phases after a 4.5 cycle delay. This is caused by slightly elevated flux asymmetries at these closing instants as their dynamic fluxes do not fully equalize within the given delay period. It is suspected that the delta winding connection is successful in equalizing these dynamic fluxes and suppressing inrush currents as confirmed by statistics analysis in Figure 5.12 but perhaps not perfect in a 4.5 cycle delay window. With a longer delay time on closing the last two phases, these fluxes are expected to converge due to system and transformer losses. Nonetheless, this would create a prolonged unbalance conditions that are unfavorable to neither HVDC operation or protection coordination and must be carefully reviewed and would not be evaluated further in this work.

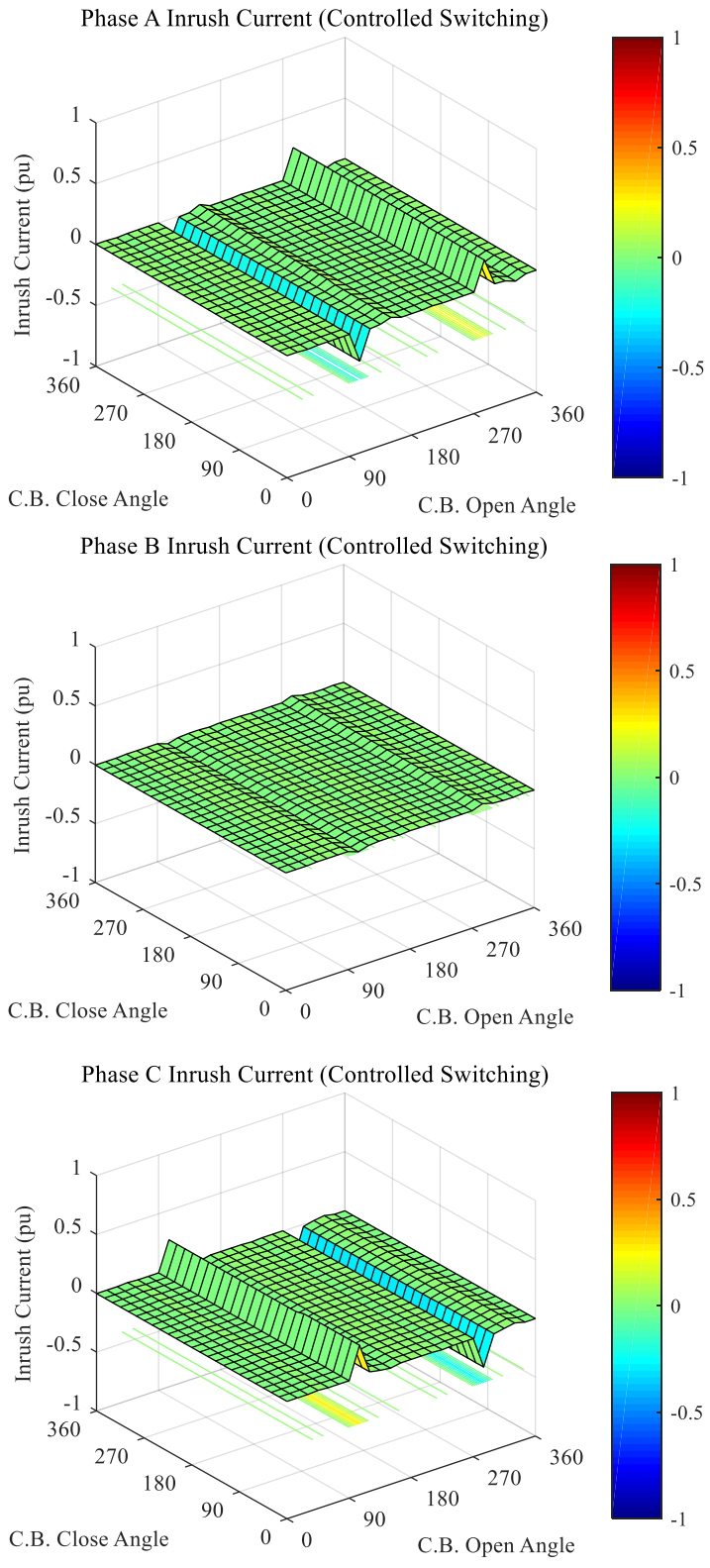

Figure 5.9 Inrush current first peaks 3D illustration
(controlled switching – 4.5 cycles delayed closing strategy)

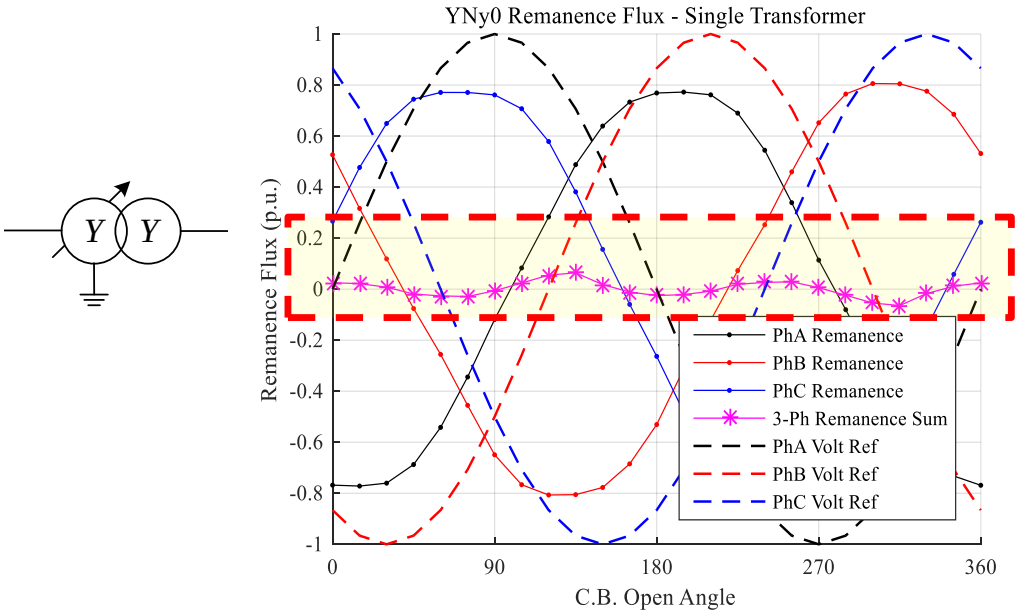

(a) Single YNy0 three-phase five-limb transformer

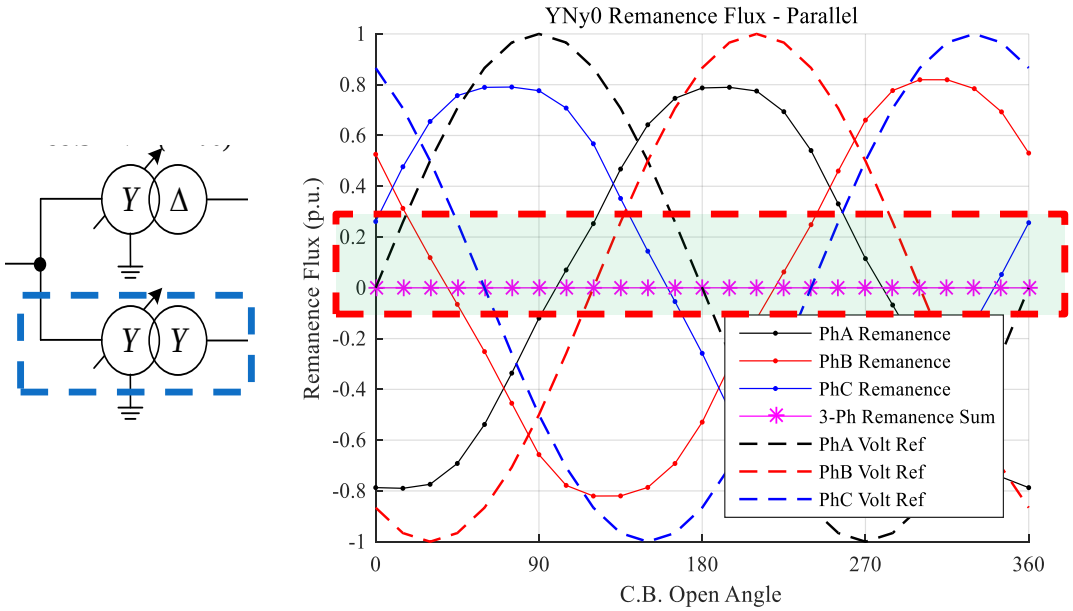

(b) Parallel-operated YNy0 three-phase five-limb transformer

Figure 5.10 YNy0 Three-phase five-limb transformer remanence flux distribution pattern on three wound limbs for single versus parallel-operation

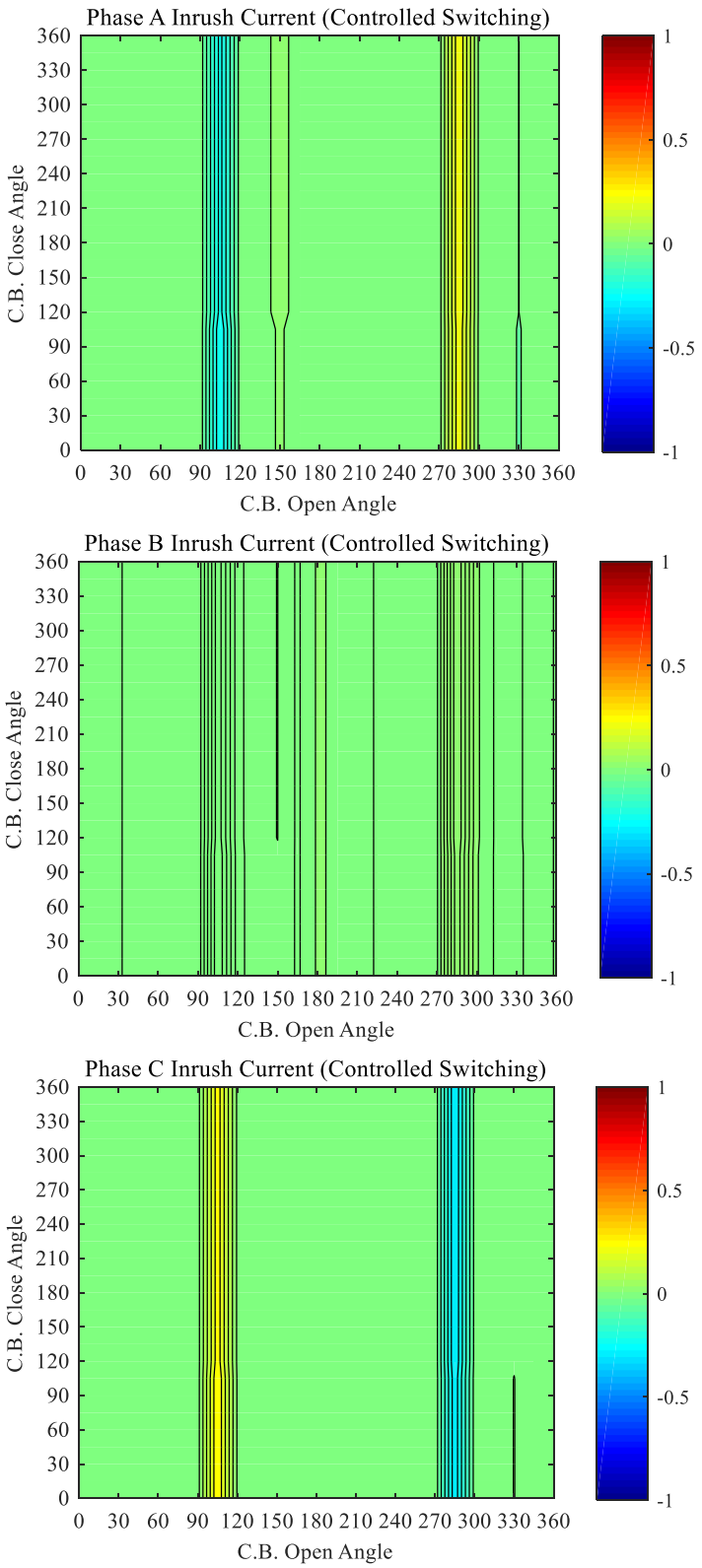

Figure 5.11 Inrush current first peaks 2D contour illustration (controlled switching – 4.5 cycles delayed closing strategy)

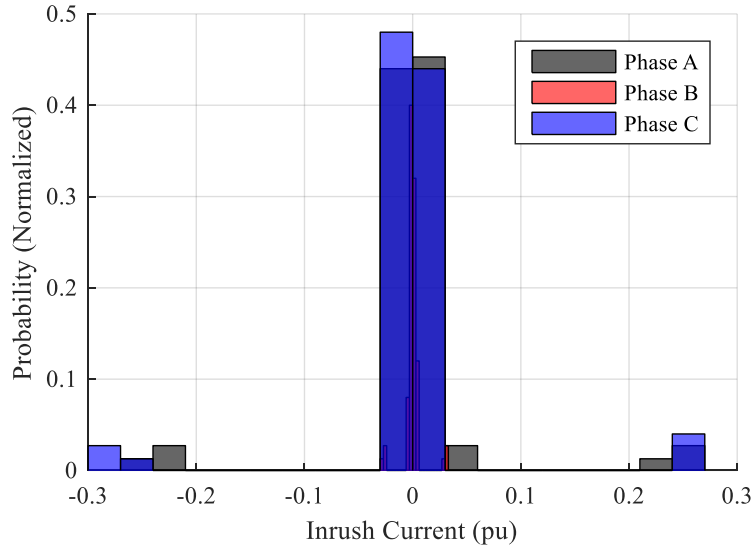

(a) Inrush current distribution

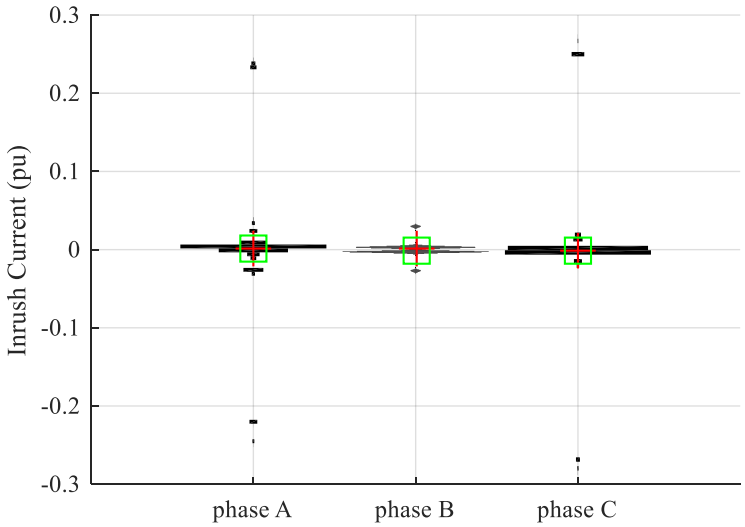

(b) Inrush current violin plot

Figure 5.12 Statistical analysis of inrush current
(controlled switching – 4.5 cycles delayed closing strategy)

5.2.3 Breaker Pre-Insertion Resistor

In contrast, the 400 ohms pre-insertion resistor with a 10 ms insertion time is capable of limited inrush current suppression but rather an incomplete elimination as shown in Figure 5.13. Additional waveform plots have been provided in Appendix B.1 which illustrates the dynamic voltage transition between breaker PIR and transformer reactance.

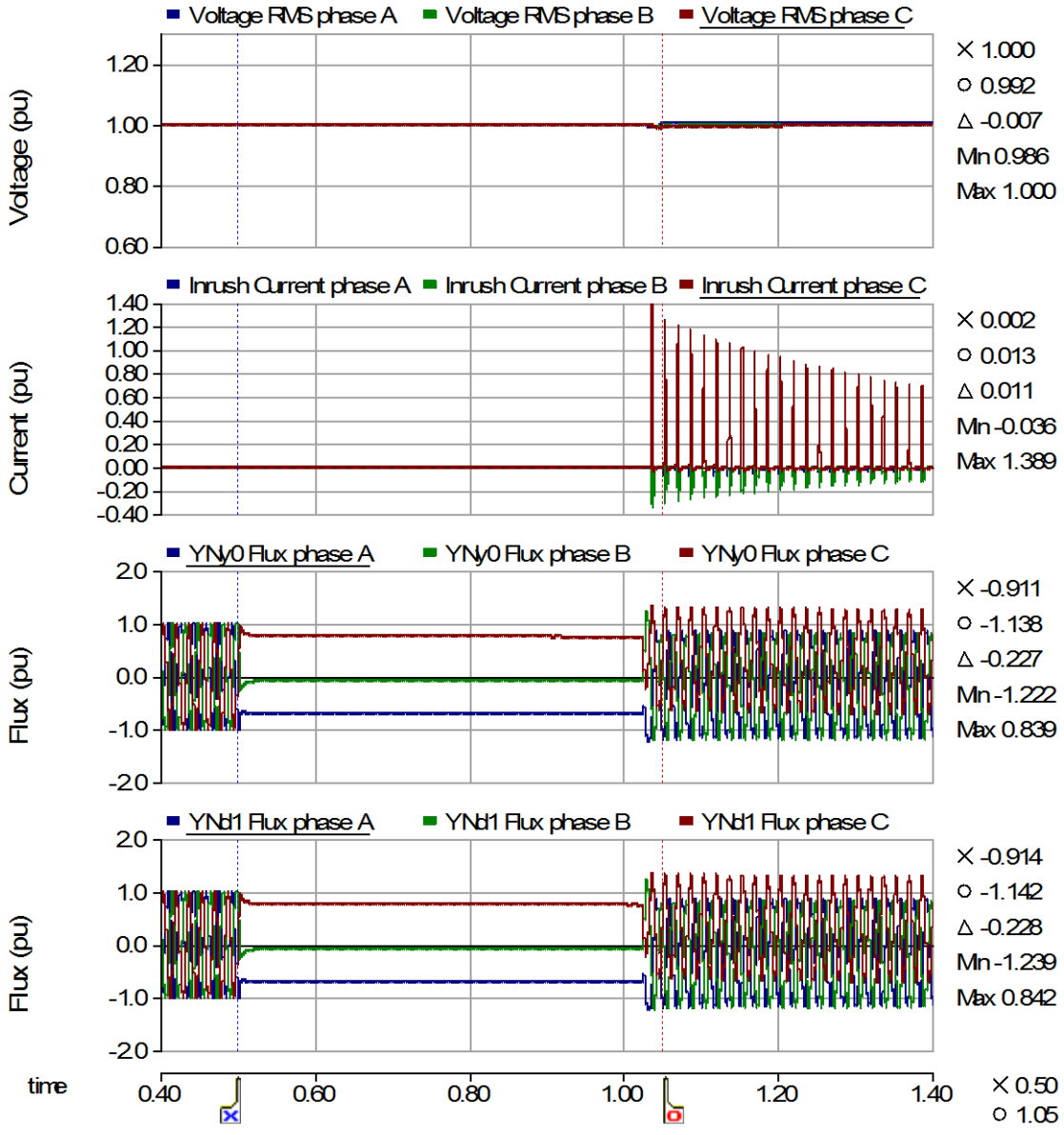

Figure 5.13 Inrush current waveforms (breaker PIR example)

The largest inrush peak magnitude observed in Figure 5.14 is about 1.4 p.u. and a relative high density of peaks above 1.0 p.u. is commonly seen in Figure 5.15. This is mainly attributed to the different fundamental philosophy on targeting inrush current reduction than that of controlled switching.

The 400 ohms PIR stays inserted in series with the nonlinear transformer core inductance for 10 ms and essentially deprives two wound limbs with the largest remanence fluxes from further excitation voltage increase when their inductance become much smaller in comparison to PIR as limb fluxes travel into saturation. High inrush current peaks are manifestations of flux on the phase that remains mostly in the unsaturated region during PIR insertion but naturally moves into saturation immediately after PIR removal.

For example, opening at 0 degrees in reference to phase A voltage rising zero transition produce a -0.8 p.u., 0.5 p.u. & 0.3 p.u. remanence flux pattern. If subsequent closing between 30 to 90 degrees on phase A, prospect flux is favorably reducing the flux asymmetry buts its magnitude is insufficient for a complete remanence effect eradication. As a result, phase A dynamic flux temporary suspends in the linear region where PIR is relatively smaller and large portion of excitation voltage remains across phase A wound limb, which in turn drives its limb flux into deep saturation soon after PIR removal. This phenomenon creates an inrush peak zone spanning 180 opening degrees by 90 closing degrees and reoccurs on all three phases 120 degrees apart as in Figure 5.15. In comparison to controlled switching in Figure 5.12, there is a relative higher probability of moderate inrush current as observed in Figure 5.16

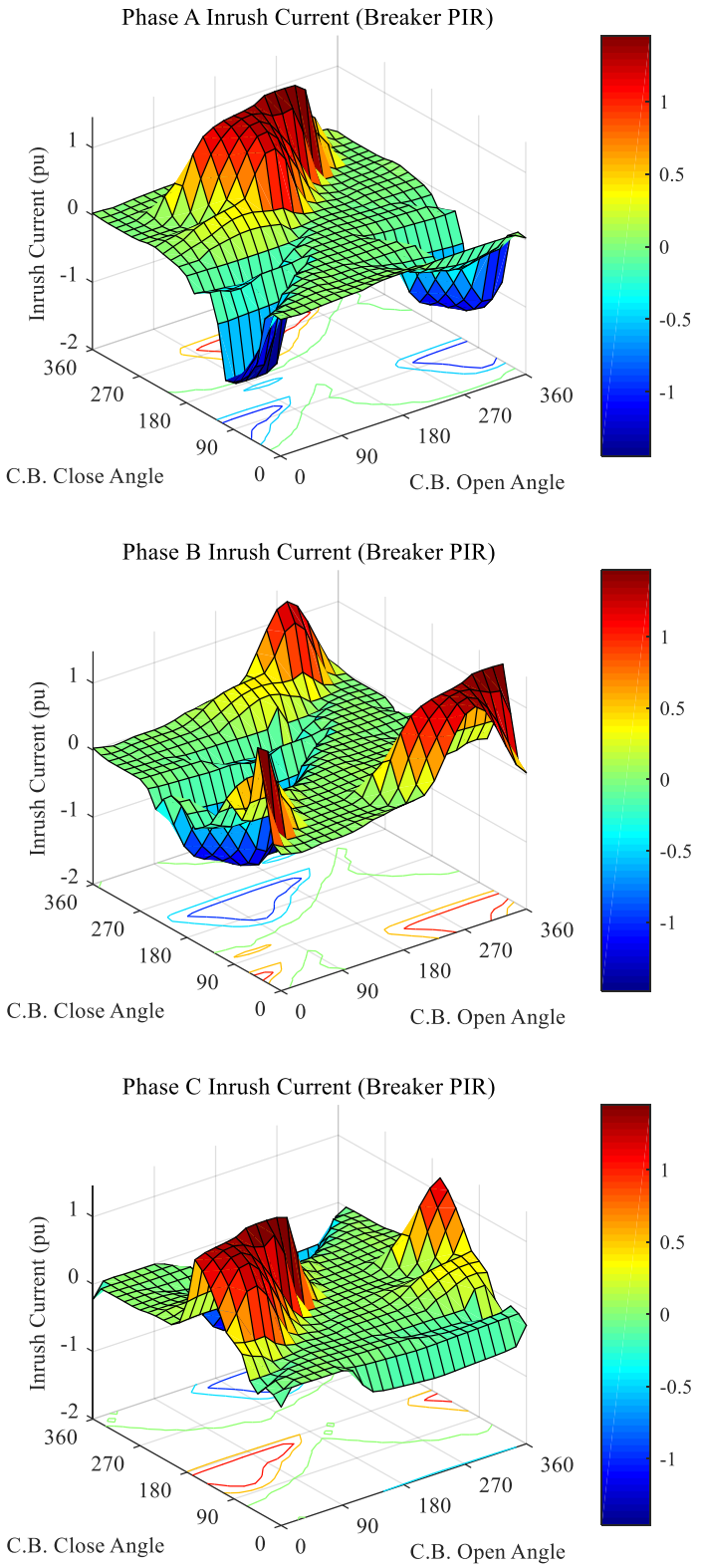

Figure 5.14 Inrush current first peaks 3D illustration
(breaker PIR 400ohms 10ms insertion)

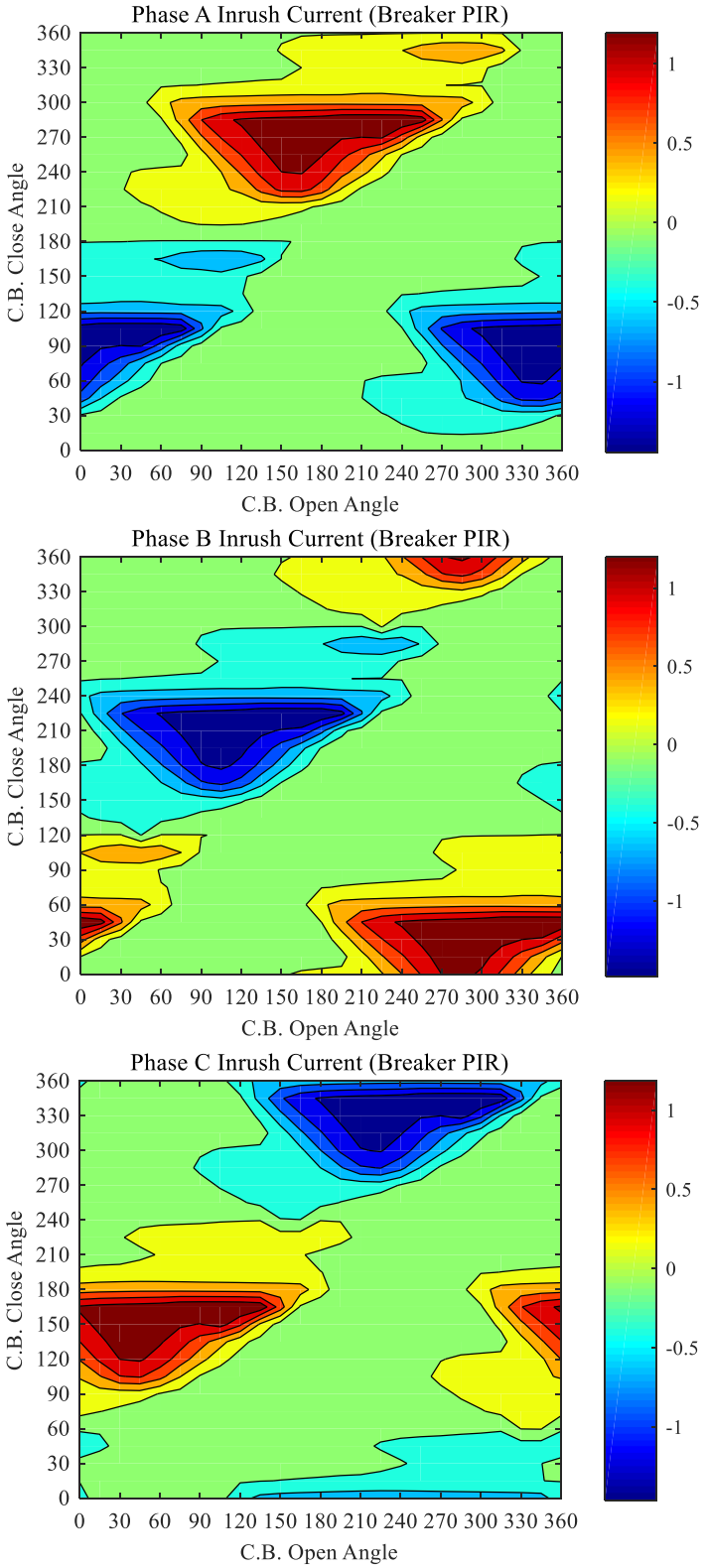

Figure 5.15 Inrush current first peaks 2D contour illustration (breaker PIR 400ohms 10ms insertion)

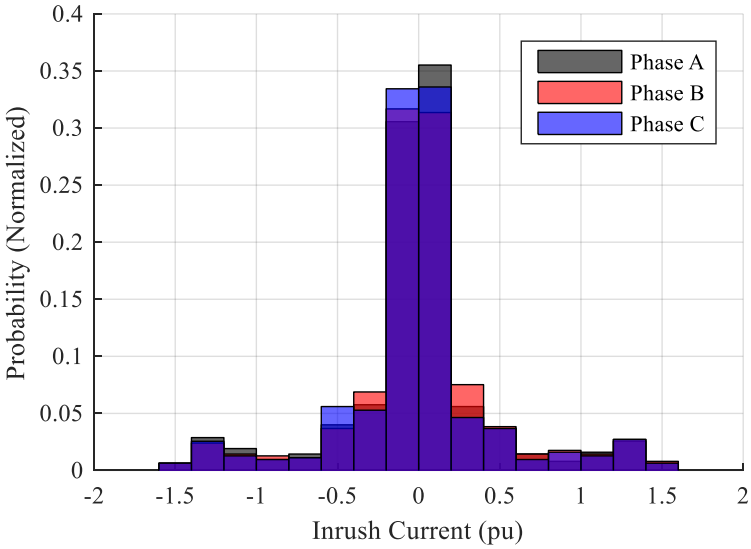

(a) Inrush current distribution

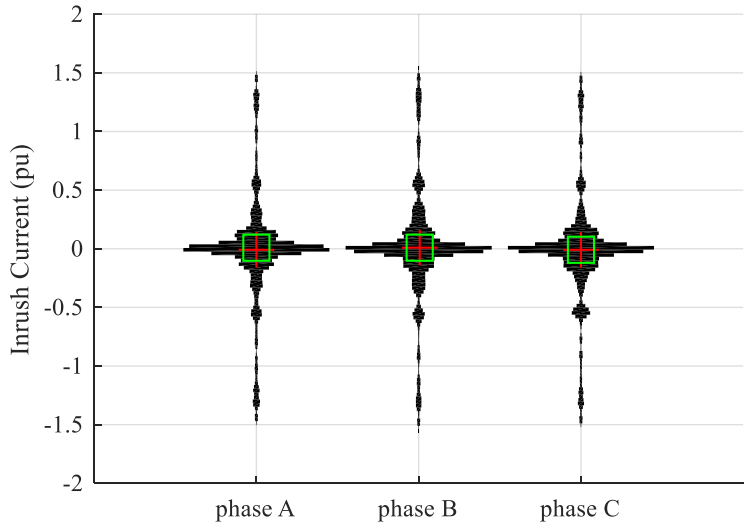

(b) Inrush current violin plot

Figure 5.16 Statistical analysis of inrush current
(breaker PIR 400ohms 10ms insertion)

5.2.4 Circuit Breaker Pole Mechanical Scatter Effects

For optimal inrush elimination, controlled switching relies on a precise, reliable and repeatable execution on individual breaker poles. Flux is time integral of source voltage waveform so any error on breaker contacts electrical making instants can aggravate flux asymmetries. Among all external factors, breaker pole scattering, either mechanical or dielectrical, is considered one of the most dominant effects [8], [86]. Modern 230kV SF6 breakers are typically guaranteed with a $+/-$ 1ms pole scatter which is inherently statistic in nature and is best characterized by a Gaussian distribution [87], [88].

In PSCAD, a Gaussian statistical breaker timing component is appended to the actual breaker closing signals to account for a $+/-$ 1ms scatter with a mean of 1ms and two standard deviations. Accordingly, the PIR insertion time and controlled switching optimal closing time have been corrected by 1ms to accommodate the mean scatter time as illustrated in Figure 5.17

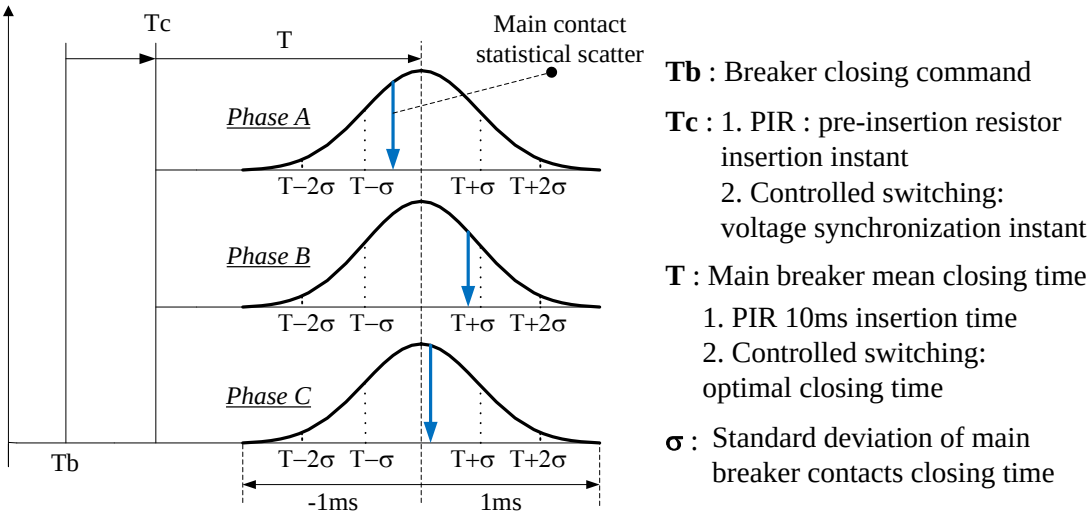

Figure 5.17 Circuit breaker scatter effects with a Gaussian distribution

Performance of controlled switching as seen in Figure 5.18 and Figure 5.19 is somewhat encroached by the uncertainties of pole closing and resultant flux asymmetries in comparison to optimal closings in Figure 5.9 and Figure 5.11. The largest inrush peak is now 1.8 p.u. but the probability of such occurrence is nil. Over 90% of inrush peaks are well within 1 p.u., most of which is lower than 0.5 p.u. as confirmed in Figure 5.20. Similarly, a degraded performance is seen in Figure 5.21 and Figure 5.22 with breaker PIR. The highest inrush peak is 2.2 p.u. with an effective insertion time of 9 ms. A relative high concentration of outlier inrush peaks over 1.0 p.u. is observed in comparison to that of controlled switching cases.

In Figure 5.24, inrush peaks are plotted against breaker statistical scatter effects. Close inspection of inrush peaks with controlled switching technique reveals that a dispersing pattern where occurrence of higher inrush peaks is more frequent as the effective closing instants are further away from the optimal time. On the contrary, plot of inrush peaks with PIR versus the breaker scatter effects displays a convergent pattern where the probability of high inrush peaks is higher with a shorter effective insertion time and is decreasing as effective insertion time becomes longer due to breaker scatter effects. These observations underline the importance of a proper compensation of circuit breaker scattering during the field commissioning for controlled switching and a longer effective insertion time for breaker PIR specification.

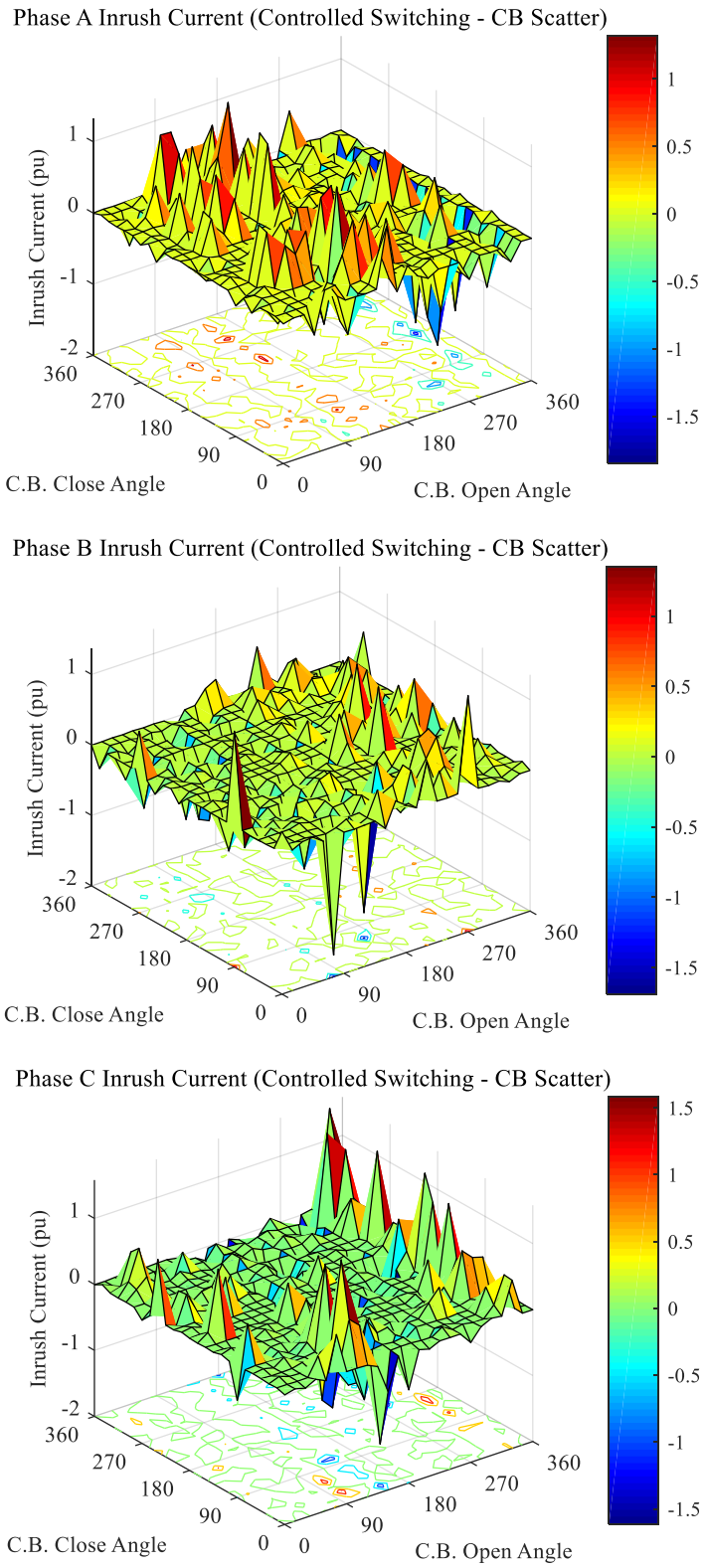

Figure 5.18 Inrush current first peaks 3D illustration (controlled switching with CB +/- 1ms scatter)

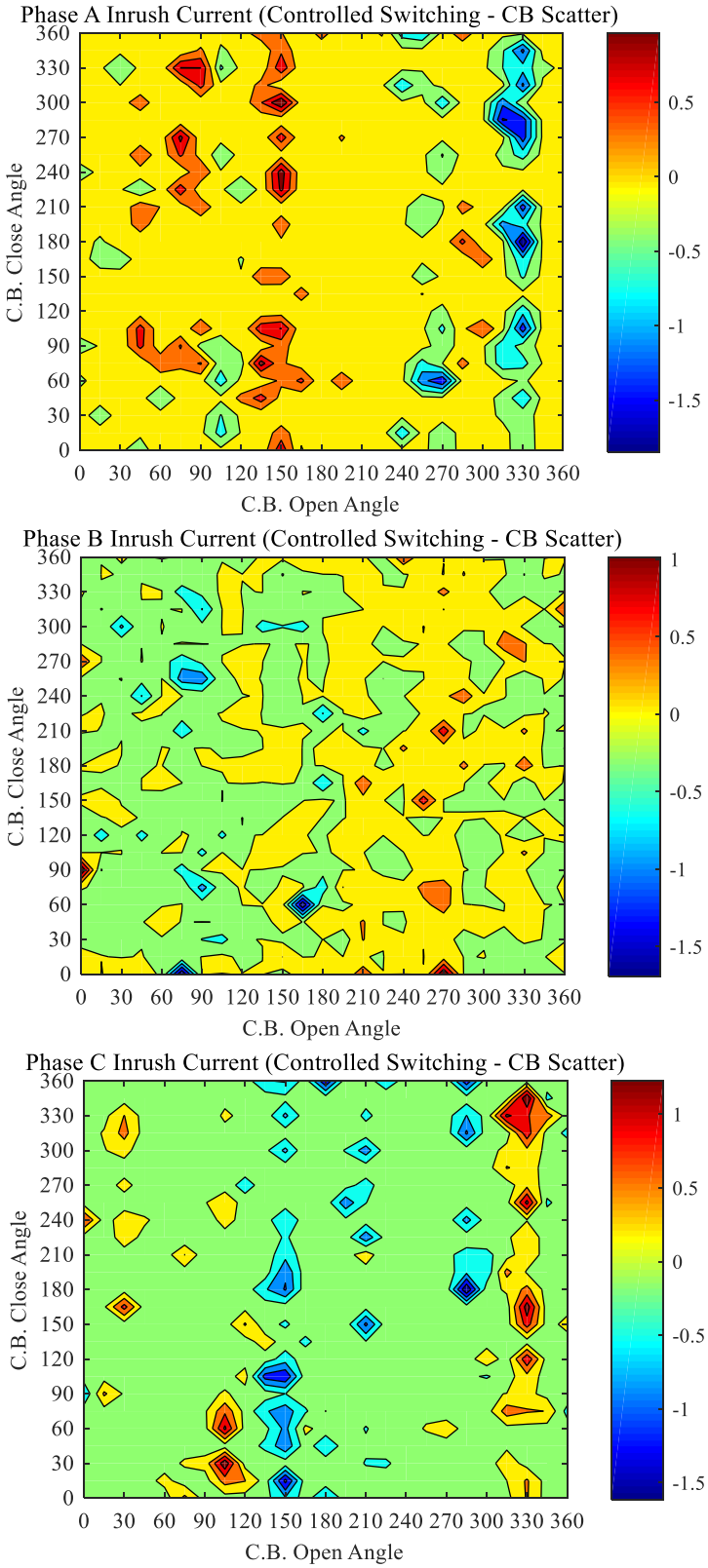

Figure 5.19 Inrush current first peaks 2D contour illustration (controlled switching with CB +/- 1ms scatter)

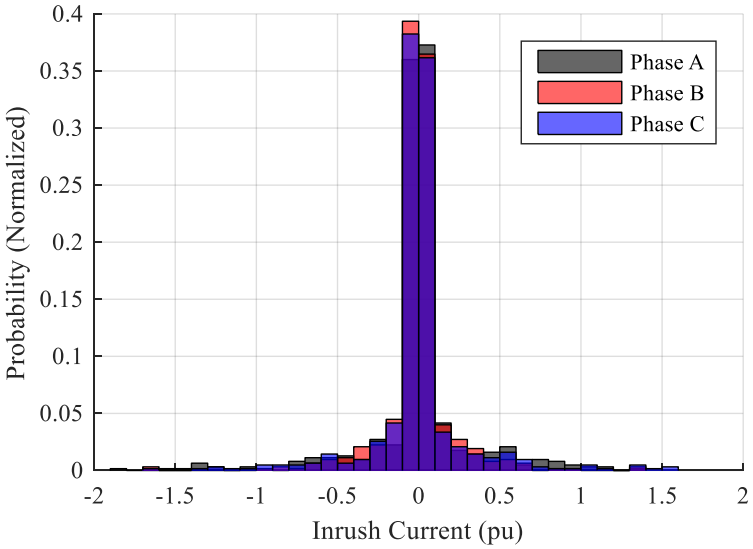

(a) Inrush current distribution

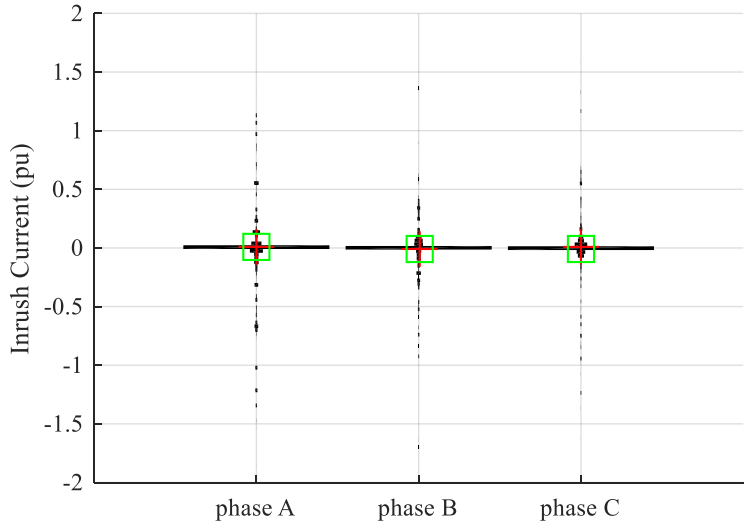

(b) Inrush current violin plot

Figure 5.20 Statistical analysis of inrush current (controlled switching with CB +/- 1ms scatter)

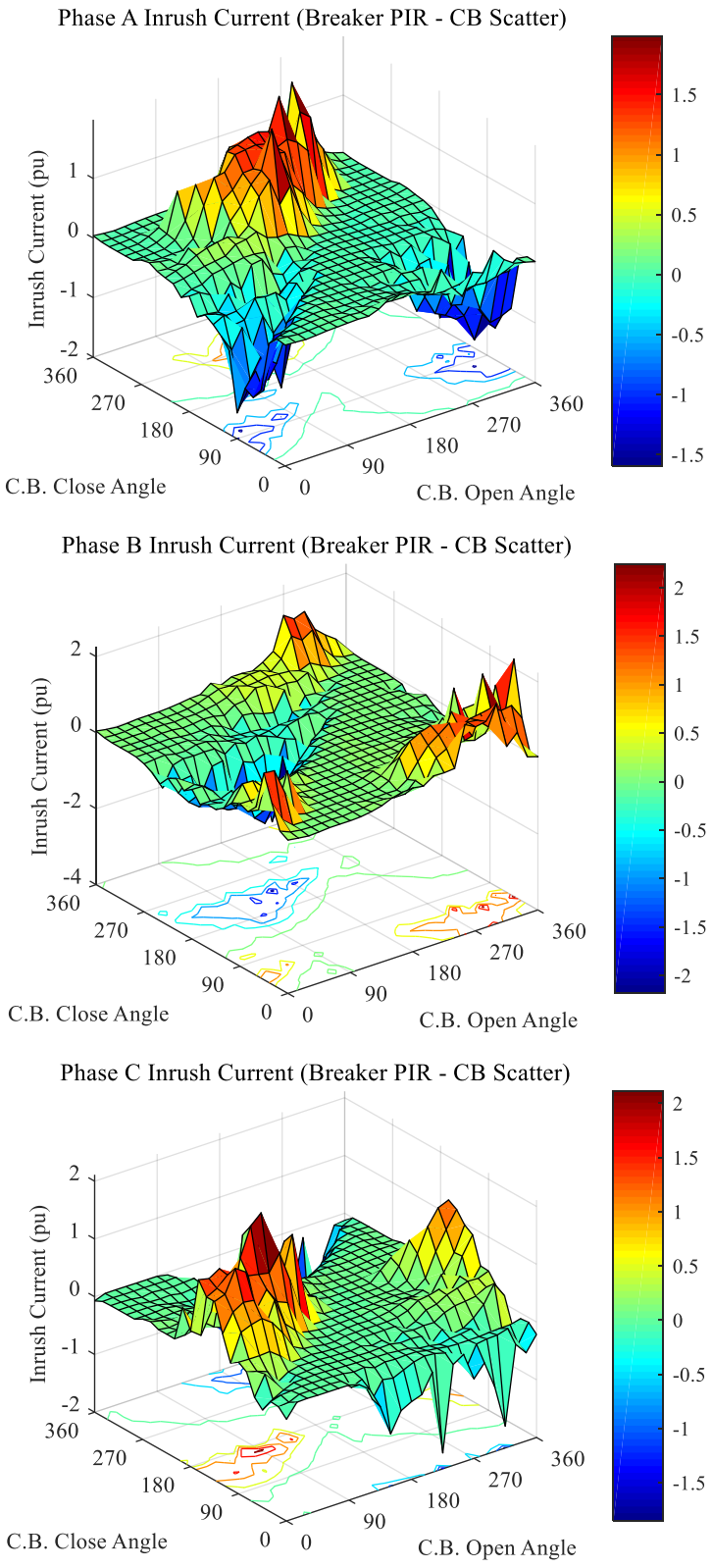

Figure 5.21 Inrush current first peaks 3D illustration
(breaker PIR 400ohms 10ms insertion with CB +/- 1ms scatter)

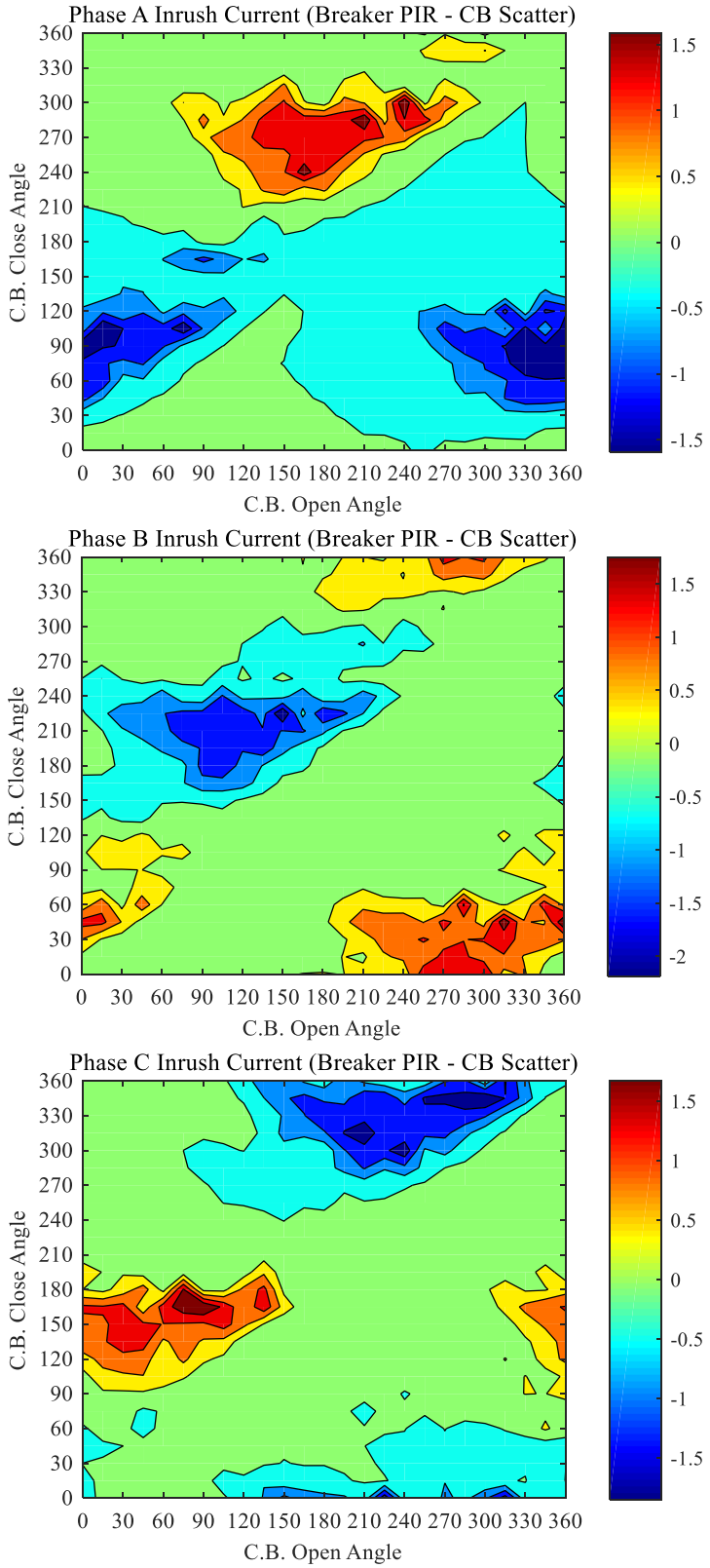

Figure 5.22 Inrush current first peaks 2D contour illustration
(breaker PIR 400ohms 10ms insertion with CB +/- 1ms scatter)

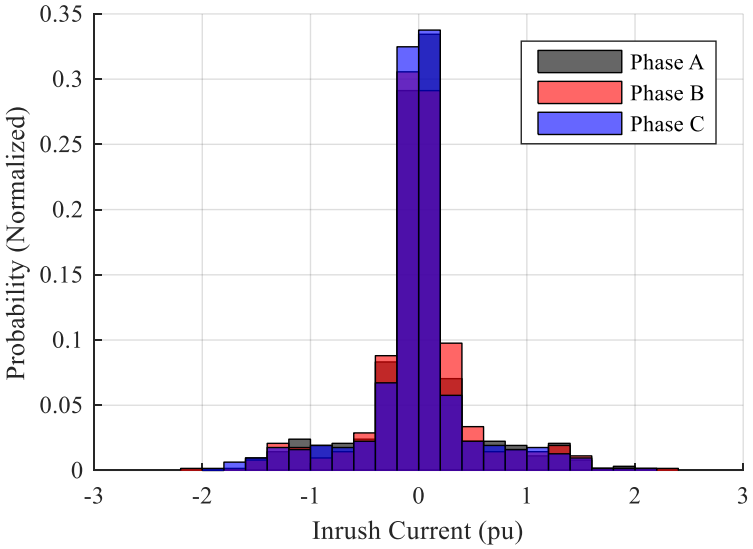

(a) Inrush current distribution

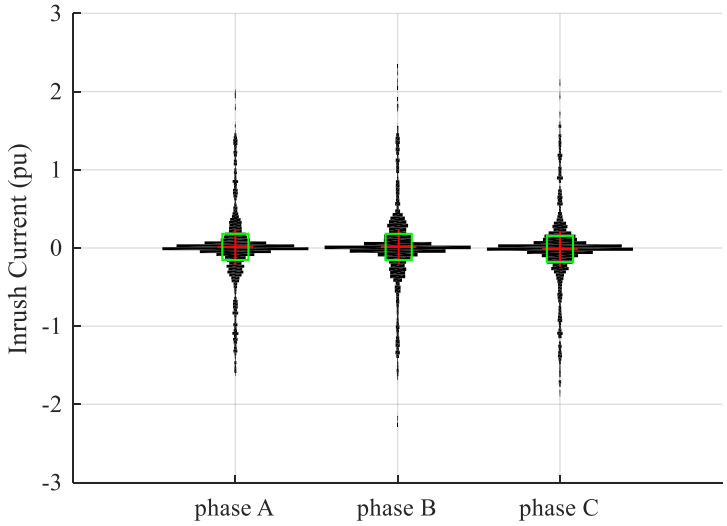

(b) Inrush current violin plot

Figure 5.23 Statistical analysis of inrush current
(breaker PIR 400ohms 10ms insertion with CB +/- 1ms scatter)

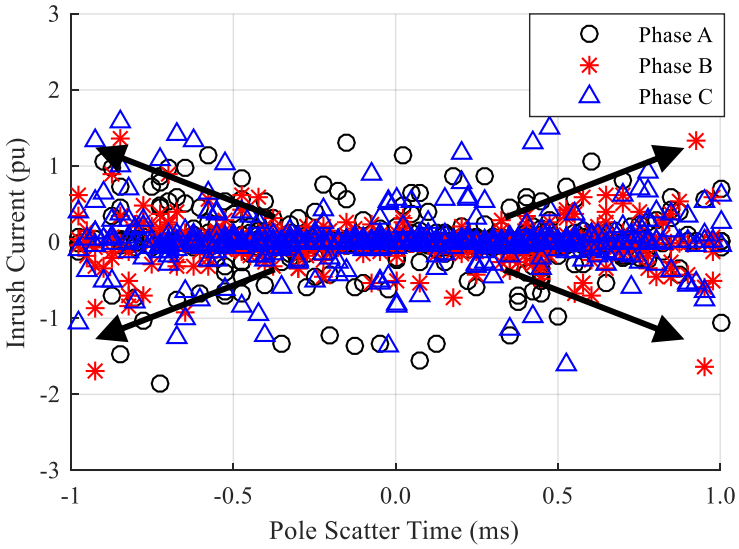

(a) Inrush peaks with controlled switching

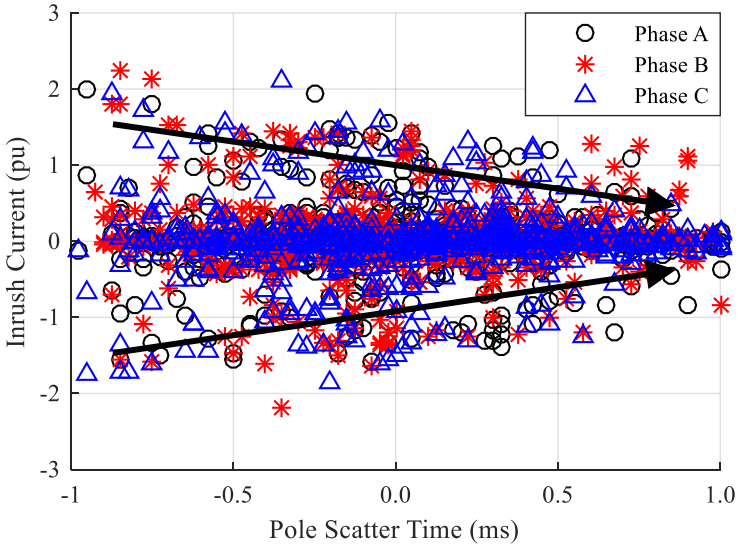

(b) Inrush peaks with breaker PIR

Figure 5.24 Inrush peaks statistic patterns with CB scattering effects

5.2.5 Converter Transformer On-Load Tap Changer (OLTC)

For optimal and economic operations, commutating bus side of HVDC converter transformers are equipped with on-load tap changers (OLTC) with a high number of tap positions capable of operating at various terminal voltage conditions. Under normal conditions, the valve groups (VG) removal process can commence a maneuver that change OLTC to its lowest tap position with the highest number of winding turns. This is designed purposely to minimize remanence flux on transformer core. During the start up of a VG, the OLTC on the converter transformers are again positioned at the lowest tap position possible, which reflects the highest number of winding turns on wound limbs to be energized. This position represents a relatively larger leakage inductance and would yield the smallest prospective fluxes that are beneficial during transformer energization with or without any remedial techniques.

Under protection initiated VG shut-down, AC circuit breaker is tripped much faster than OLTC movements. This essentially let the transformer core get de-energized at its nominal tap position. However, OLTC are then moved to its lowest tap position prior to the subsequent energization. This is expected to have no major impact on the performance of breaker PIR or controlled switching that considers OLTC tap information. However, it is a more complex problem when knowledge of OLTC tap is unknown for the controlled switching technique. The stop and start positions of converter transformer OLTC for normal and protection initiated shut-downs are illustrated in Figure 5.25.

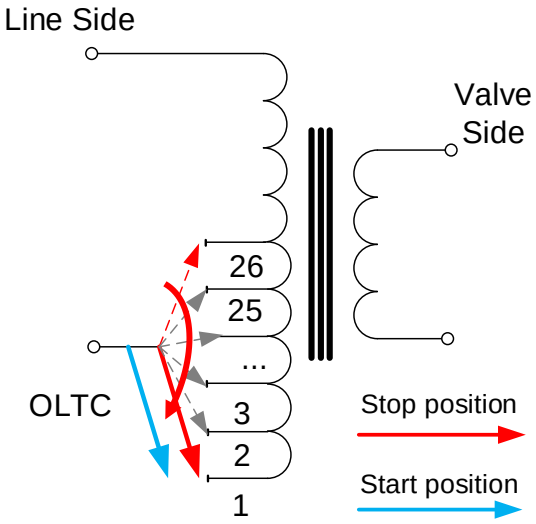

(a) Normal VG and converter transformer shut-down

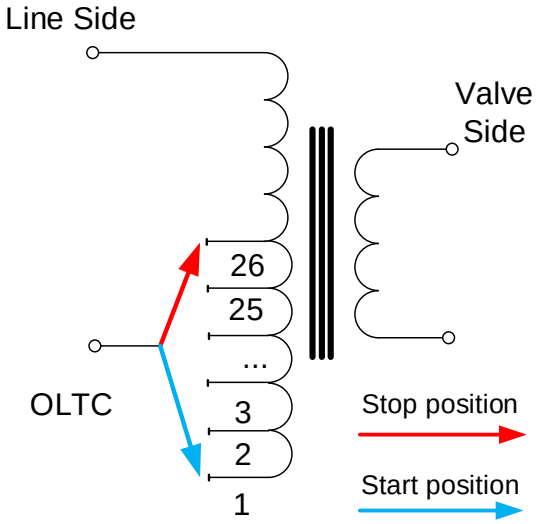

(b) Emergency VG and converter transformer shut-down

Figure 5.25 Converter transformer OLTC stop and start positions under normal and protection initiated shut-downs

To investigate the impact of OLTC movements on performance of controlled switching, the systematic inrush peak study is repeated with circuit breaker pole scatter effects. In addition, the converter transformer pair is de-energized at nominal Tap 26 and

subsequently energized at the lowest position Tap 1 in Table 5.1. This represents a 39% difference in winding voltages or winding turns between the de-energization and energization switchings.

In comparison to section 5.2.4, Figure 5.26 and Figure 5.27 confirm that the probability of high inrush peaks is greatly reduced even when OLTC position is not taken into account. OLTC remains at Tap 26 during transformer de-energization and moves to Tap 1 during energization with a $+/-$ 1ms breaker scatter considered. The largest inrush peak is reduced to 1.3 p.u. and up to 95% of calculated inrush peak magnitudes are less than 0.5 p.u. as seen in Figure 5.28. Impact of breaker pole scatter on controlled switching performance is deescalated as confirmed in Figure 5.29

During protection initiated converter transformers de-energization, a properly commissioned controlled switching device is expected to correctly estimate remanence fluxes on transformer core since OLTC still remains at its nominal position Tap 26 at the time. With no prior knowledge of the new OLTC position, the device would continue to calculate and issue an "optimal" closing time assuming a unchanged OLTC. Prospective fluxes created at Tap 26 and Tap 1 positions are in phase but with different peak magnitudes of 1.0 p.u. and 0.72 p.u., respectively. When temporarily neglecting breaker scatter and losses for simplicity, the most pessimistic flux calculation error would be 0.28 p.u. flux asymmetry, which superimposes on a much lower symmetric perspective flux of 0.72 p.u., as in Equation (4.1), is still well below core saturation level. Of course, breaker scatter effects would escalate this flux asymmetry. Therefore, it would be beneficial to energize the converter transformer pair with OLTC at Tap 1 position.

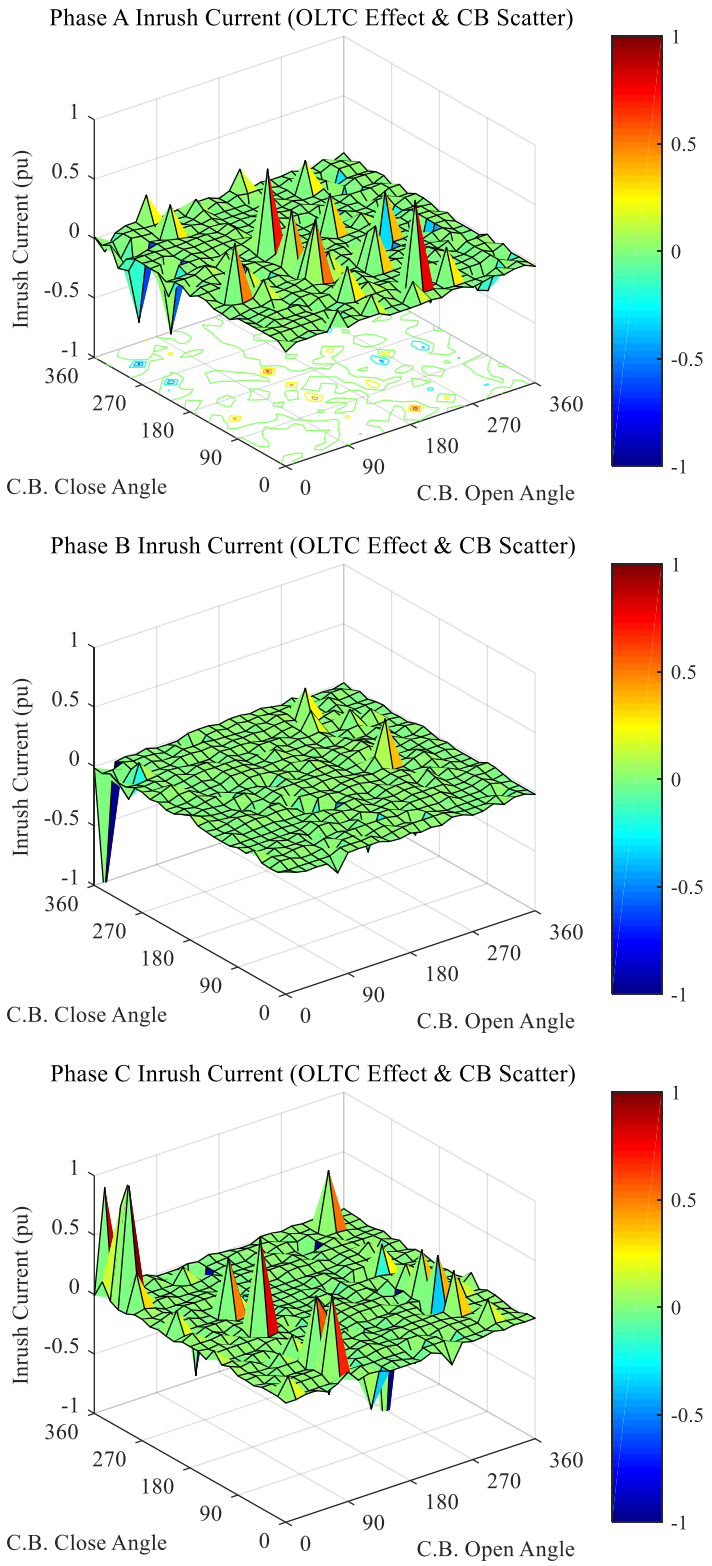

Figure 5.26 Inrush current first peaks 3D illustration (controlled switching with OLTC & CB scatter effects)

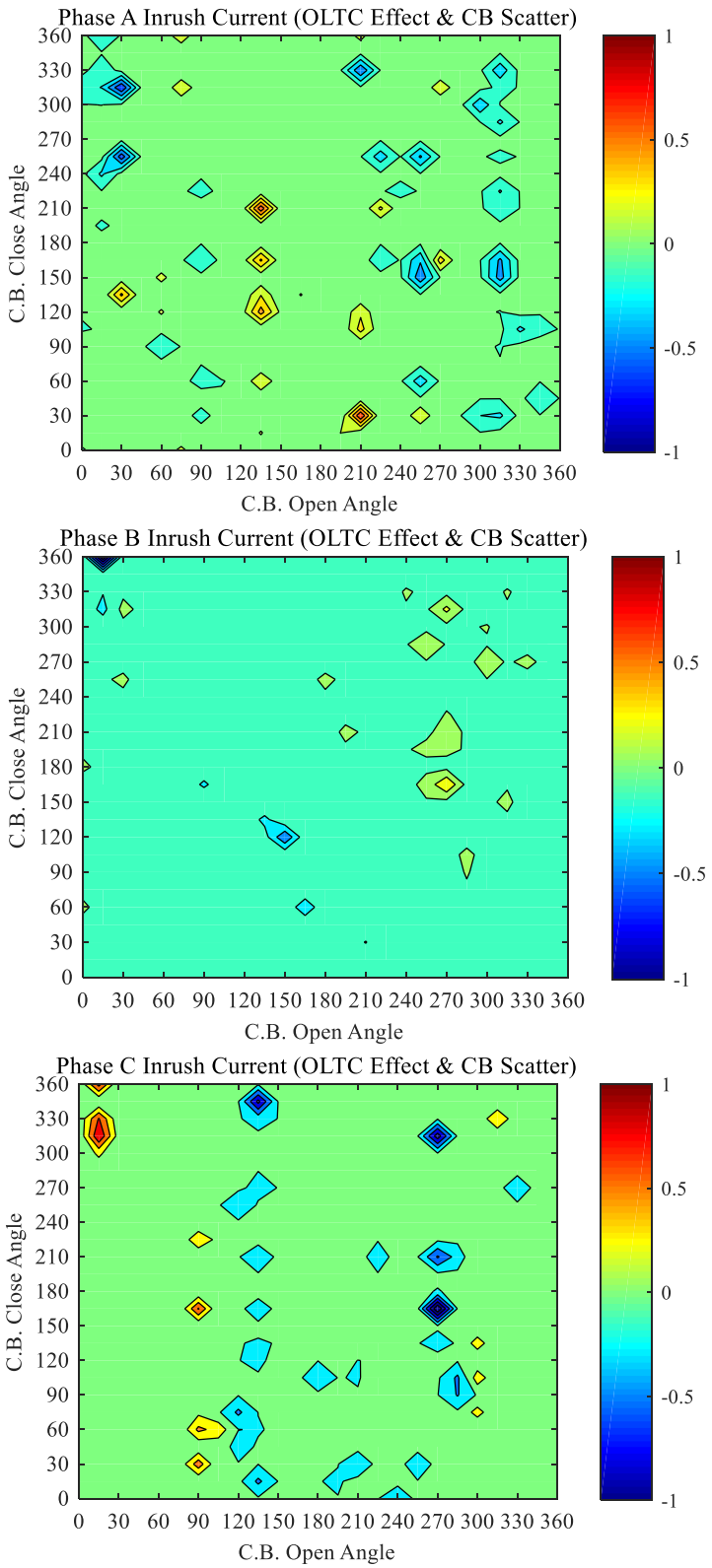

Figure 5.27 Inrush current first peaks 2D contour illustration (controlled switching with OLTC & CB scatter effects)

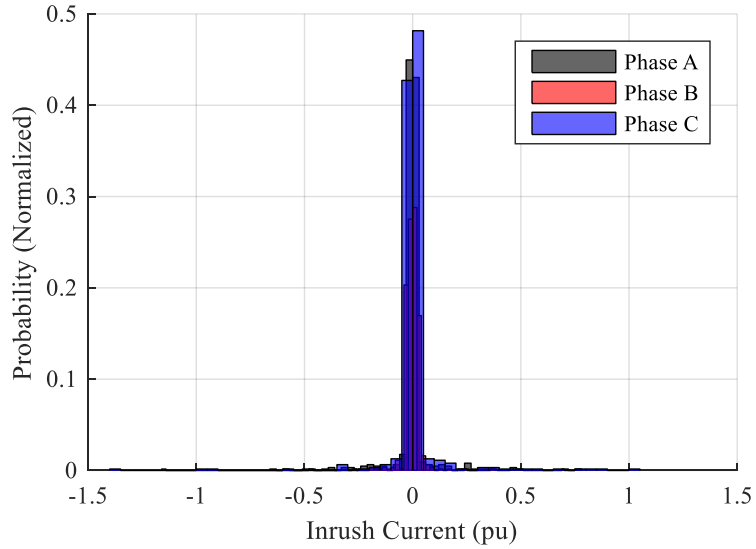

(a) Inrush current distribution

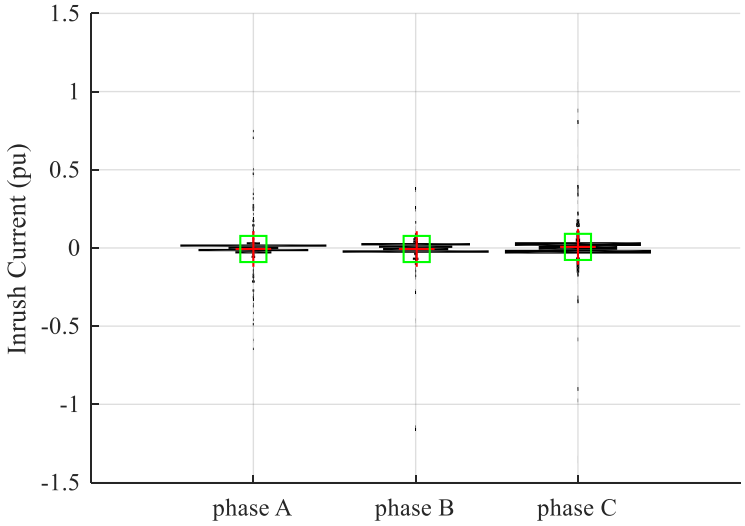

(b) Inrush current violin plot

Figure 5.28 Statistical analysis of inrush current
(controlled switching with OLTC & CB scatter effects)

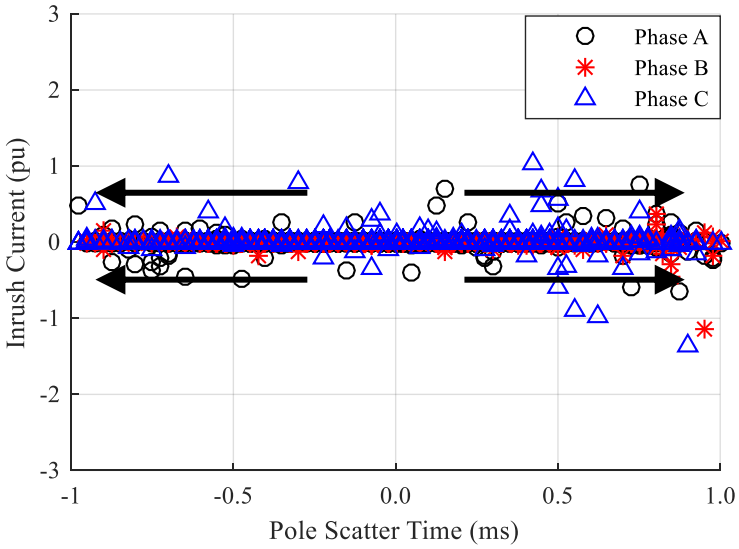

(a) Inrush current pattern

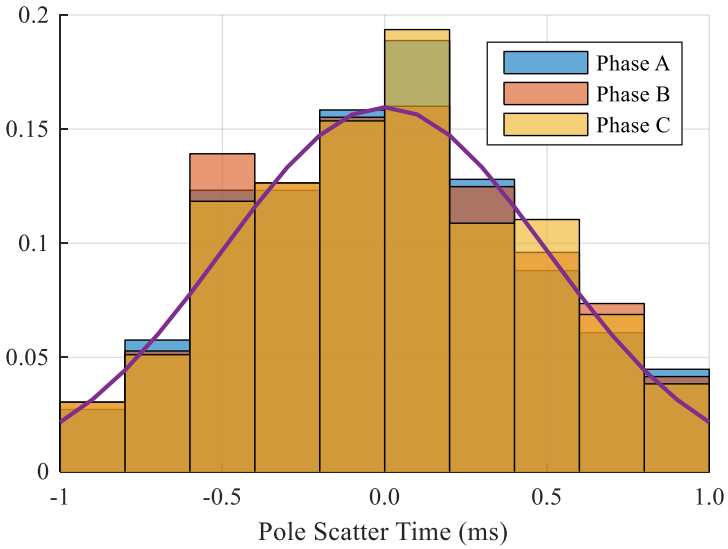

(b) Breaker pole scatter Gaussian distribution

Figure 5.29 Inrush peaks and breaker pole statistic patterns
(controlled switching with OLTC & CB scattering effects)

5.3 Concluding Remarks

In this chapter, feasibility and performance aspects of controlled switching energization that accounts for remanence flux of a parallel-operated five-limb converter transformer pair is investigated by an extensive systematic inrush current analysis in PSCAD/EMTDC.

A controlled switching with delayed closing strategy has been developed in PSCAD that is capable of estimating remanence fluxes and correctly predicts optimal closing instants during unloaded transformer energization. An exhaustive systematic analysis of inrush current reduction by controlled switching technique and breaker PIR is conducted with considerations of breaker scatter effects and impacts of OLTC movements due to HVDC protection tripping. In-depth analysis of study results has concluded that controlled switching yields an overall superior performance on inrush current reduction in comparison to the limited reduction ability by breaker PIR. It is shown that the single delta winding in the parallel-operated converter transformer pair can be perceived as a virtual winding connection commonly shared by both transformers. This ensures flux equalization as required by controlled switching delayed closing strategy. It was suspected that the virtual delta connection was adequate in creating flux equalization effect but it was not perfect. Study results have also shown that it is beneficial to adjust OLTC to the lowest tap position of the highest winding turns during energization of the converter transformer pair for the purpose of additional inrush current reduction.

Chapter 6

Conclusions and Contributions

This chapter presents conclusions of this research work, highlights main contributions, and make suggestions on future research directions.

6.1 Conclusions

In this thesis, viability and performance of controlled switching using a delayed closing strategy on parallel-operated three-phase five-limb converter transformer pair were thoroughly investigated. As accurate representation of transformer ferromagnetic core behavior is critically important for this study, the research started by reviewing J-A hysteresis model, which is commonly use in EMT simulation models of transformers. The review revealed variations in J-A model mathematical expressions published in different literature, and the origins of the discrepancy. Then an optimization based intelligent technique was proposed to improve the overall accuracy of model parameters identification. Additional efforts were made to improve the computational efficiency of numerical solution of J-A model embedded in transformer models.

Initial effort of this thesis reported in Chapter 2 was devoted to illustrate the derivation of inverse J-A model that was in accordance with the original J-A theory. Potential benefits of this inversely formulated J-A model with magnetic induction B as the dependent

variable in power transformer models in EMT programs were explained. Measures to prevent non-physical solutions by the derived inverse J-A model were proposed and incorporated. Inverse J-A model was only an alternative formulation of the original equations and therefore model parameters and their identification processes remained identical to the original model.

In Chapter 3, a novel constrained multi-objective PSO process was developed for J-A model identification and optimization. Special attention was given to the initial search boundary range specifications that respected intrinsic physical properties of Si-Fe GOES. For improved convergence, a constrained initialization process was proposed to replace ill-defined parameters that produced non-physical J-A solutions by more promising values. Condition requirements of Annakkage anhysteretic function parameters were also enforced. A universal fitness function was proposed to comprehensively evaluate separate fitness objectives. These individual fitness objectives were designed for reducing errors between calculated and measured quantities of hysteresis loops, hysteresis enclosed areas, and magnetization curve. In PSO main search routine, measures were implemented to rectify any outbound particles and violation of anhysteretic function parameters requirements. A dynamically adjusted weight factor was adopted to maximize global exploration ability of each particle at start to rapidly identify potential global optimums and then to mainly concentrate on local exploitation to refine the global optima.

Published measurements of hysteresis loops at 1.0T, 1.3T, 1.5T and 1.7T and magnetization curve of AK Steel 23mm M3 grade DR GOES specimen were extracted and prepared for validating this novel multi-objective PSO technique in Chapter 3. Excellent agreement between measured and calculated quantities was obtained for each single

hysteresis loop together with magnetization curve. A new process was developed to simultaneously identify and optimize J-A modal parameters for all four hysteresis loops and magnetization curve using the constrained multi-objective PSO. Deviation between the measured and calculated hysteresis loops was observed, especially in characterizing the widths of minor and major hysteresis loops. The investigations revealed that original J-A model was only capable of describing magnetic behavior within limited magnetic flux density range.

Close inspection of the deficiency of the J-A model calculations suggested that a variable pinning parameter k could be introduced to replace the constant parameter in the model presented in Chapter 3. A novel methodology was created with constrained multi-objective PSO embedded in order to identify the functional relation between the pinning parameter k and the relative magnetization M/M_s. An empirical function of variable k was incorporated into the J-A model. The constrained multi-objective PSO procedure was again utilized for a simultaneous determination of model parameters using all hysteresis loops and magnetization curve. The modified J-A model with parameters found with the new procedure showed a substantial improvement in representing both minor and major hysteresis loops as well as magnetization curve, thus validating the proposed modification. The model was augmented to incorporate classic and excess eddy current losses, but due to limitations of available measurements and time domain information, model parameters could not be identified. Instead, a trial and error technique was later introduced in PSCAD model for identifying the parameters.

In Chapter 4, a brief review of controlled switching theory while taking remanence flux into account on unloaded power transformer energization was presented. Such technique

on optimal inrush current elimination was limited only to transformers with a three-phase three-limb core or with a delta winding connection. This limitation due to flux equalization phenomenon was explained. Given the practical implementation considerations, controlled switching using the delayed closing strategy was selected for study, and a brief background of such strategy was provided.

Uncertainties on feasibility of controlled switching with delayed closing strategy on parallel-operated three-phase five-limb converter transformers were elaborated in Chapter 4. Extensive literature review revealed no publications with comprehensive investigation on such research topic. A controlled switching component was developed in PSCAD that was capable of estimating remanence fluxes during transformer de-energization and correctly calculating and issuing the optimal breaker closing signals in the subsequent energization.

The modified inverse J-A model with variable k was incorporated into a duality principle based hybrid transformer model in PSCAD/EMTDC. A novel J-A model numerical solution algorithm was developed and shown to significantly improve the computation efficiency over the existing approach. Frequency dependent effects of classic and excess eddy currents were implemented. Using values of a M4 grade GOES, these eddy current related parameters were tuned and adjusted against a collection of hysteresis loops with 1.0T, 1.5T and 1.7T peaks measured at 50Hz. Comparison of measured and calculated by the modified inverse J-A model showed overall satisfactory agreements on all the hysteresis loops and magnetization curve.

In Chapter 5, systematic analysis of inrush current transients during the parallel-operated converter transformer energization was conducted in PSCAD. It was concluded

that controlled switching of such transformer configuration was feasible and effective using the delayed closing strategy. The single delta connection in YNd1 transformer could be perceived as a virtually shared delta winding to the pair due to magnetic and electrical interaction. This virtually shared winding provided a conduit for sufficient but perhaps not perfect flux equalization process. Simulation results showed that in general controlled switching provided superior inrush current suppression capability than breaker PIR with or without considering breaker pole scatter effects. Breaker scatter effect was seen to impact controlled switching in such a way that deteriorated inrush reduction was seen as the actual closing instants move further away from the optimal closing instants. On the contrary, a longer effective PIR insertion time due to breaker scatter was observed to be in favor of PIR performance.

Considerations of converter OLTC position movements during HVDC protection initiated transformer de-energization were also investigated. If OLTC position information was used in controlled switching, optimal closing instants could be compensated accordingly and no disruption to its performance was expected. If controlled switching devices had no prior knowledge of OLTC maneuver, an elevated flux asymmetry would occur due to the error between the presumed perspective flux and the actual perspective flux. Despite this subtle flux offset, energizing with OLTC positioned at Tap 1 (lowest tap with the largest number of winding turns) would still be beneficial to controlled switching as the actual perspective flux at this position was only 79% of the perspective flux peak at Tap 26.

6.2 Contributions

The main contributions of this thesis are summarized below:

1. Review of J-A hysteresis model and derivation of mathematical equations for inverse J-A model.
2. Development of a novel constrained multi-objective PSO procedure that is capable of identification of J-A model parameters using a single hysteresis loop and magnetization curve or simultaneously using several hysteresis loops and magnetization curve. This yielded a J-A model which is accurate in describing both unsaturated and heavily saturated magnetic regions.
3. Development of a methodology using constrained multi-objective PSO to define a functional relation of pinning parameter k with respect to magnetization level M/M_s.
4. Development and validation of a new modified inverse J-A model with a variable pinning parameter k against published measurements of AK Steel 23mm M3 grade DR GOES.
5. Incorporation of a modified dynamic inverse J-A hysteresis model with frequency-dependency into a hybrid three-phase five-limb transformer model in PSCAD/EMTDC. With proper tuning and adjustment, this model showed a satisfactory precision in comparison to a set of measured hysteresis loops at 50Hz.
6. Development of a novel computationally efficient numerical solution algorithm for the modified inverse J-A model.
7. Systematic inrush current analysis that confirms feasibility and performance of controlled switching using delayed closing strategy on a parallel-operated three-phase

five-limb converter transformer pair with considerations of breaker scatters and OLTC effects.

6.3 Suggestions for Future Research

In this thesis, the constrained multi-objective PSO was developed to identify J-A model parameters based on magnetic characteristics of AK Steel 23mm M3 grade DR GOES specimen. Default J-A model parameters for other GOES grade, such as regular M3, M4, M5, and etcetera, could be optimized and included as options in PSCAD/EMTDC for users.

A new methodology was proposed to determine variable pinning parameter based on this material. A set of more generic functional relations for variable J-A model parameters could be defined using this methodology and multi-objective PSO for other GOES grades. A modified J-A model with full variable parameters has been successfully implemented and validated for M3 grade DR GOES.

The magnetization curve was considered for the identification of Annakkage anhysteretic function parameters, but this aspect could be further refined. Sampling of measurements at equal intervals on the B-H loops and B-H magnetization curve may be considered to further improve PSO convergence.

Constrained initialization was adopted in PSO to regenerate ill-defined parameters as this technique did not have mutation or elimination mechanisms. A hybrid PSO technique could be implemented to incorporate such mechanisms to recreate new particles if ill-defined particles are identified during the main PSO search routine.

A novel numerical solution algorithm was developed to significantly improve the computational efficiency of the modified inverse J-A model with variable pinning

parameter k. However, there was room for further optimization and computation expense reduction, and possibility of implementation on Real Time Digital Simulator (RTDS).

The hybrid five-limb transformer model was deemed robust but further improvements could be made to segregate its winding presentation. Besides early efforts by [51] and [52], extensive validation and improvement of this model could be continued in a laboratory environment. Auxiliary supporting routines should be developed to facilitate the fine tuning of key parameters based on typical RMS measurements of three phase averages from transformer factory acceptance tests (FAT). On the other hand, development of ideal coupling transformer and J-A hysteretic saturable reactor components in PSCAD/EMTDC could offer flexibility and liberty that empower advanced users to freely construct single-phase and three-phase transformer models with three-limb or five-limb core and up to three windings based on duality principle.

Appendix A

A.1 Extended Annakkage Anhysteretic Function with Five-Parameter

$$M_{an} = \frac{a_1 H_e + a_2 H_e^2}{a_3 + a_4 H_e + a_5 He^2} \tag{A.1}$$

$$\frac{dM_{an}}{dH_e} = M_s \frac{a_1 a_3 + b a_2 a_3 H_e^{b-1} + (b-1)(a_2 a_4 - a_1 a_5) H_e^b}{a_3 + a_4 H_e + a_5 H_e^b} \tag{A.2}$$

where a_1, a_2, a_3, a_4, a_5 are anhysteretic function form parameters,

b is a constant value and here is set $b = 2$.

Appendix B

B.1 PSCAD/EMTDC Simulation Waveforms

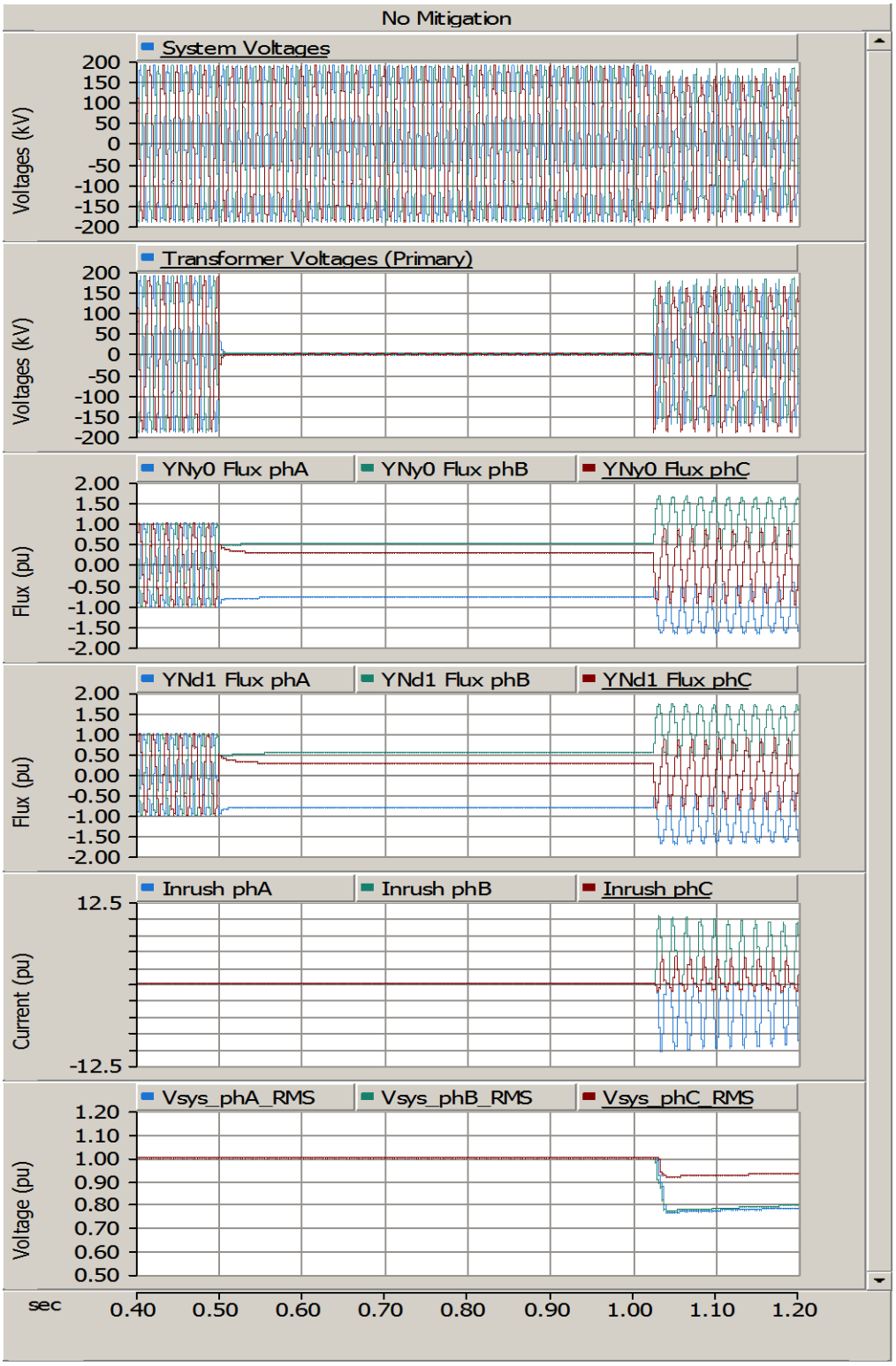

Figure B.1 Inrush currents of five-limb converter transformer pair (no mitigation)

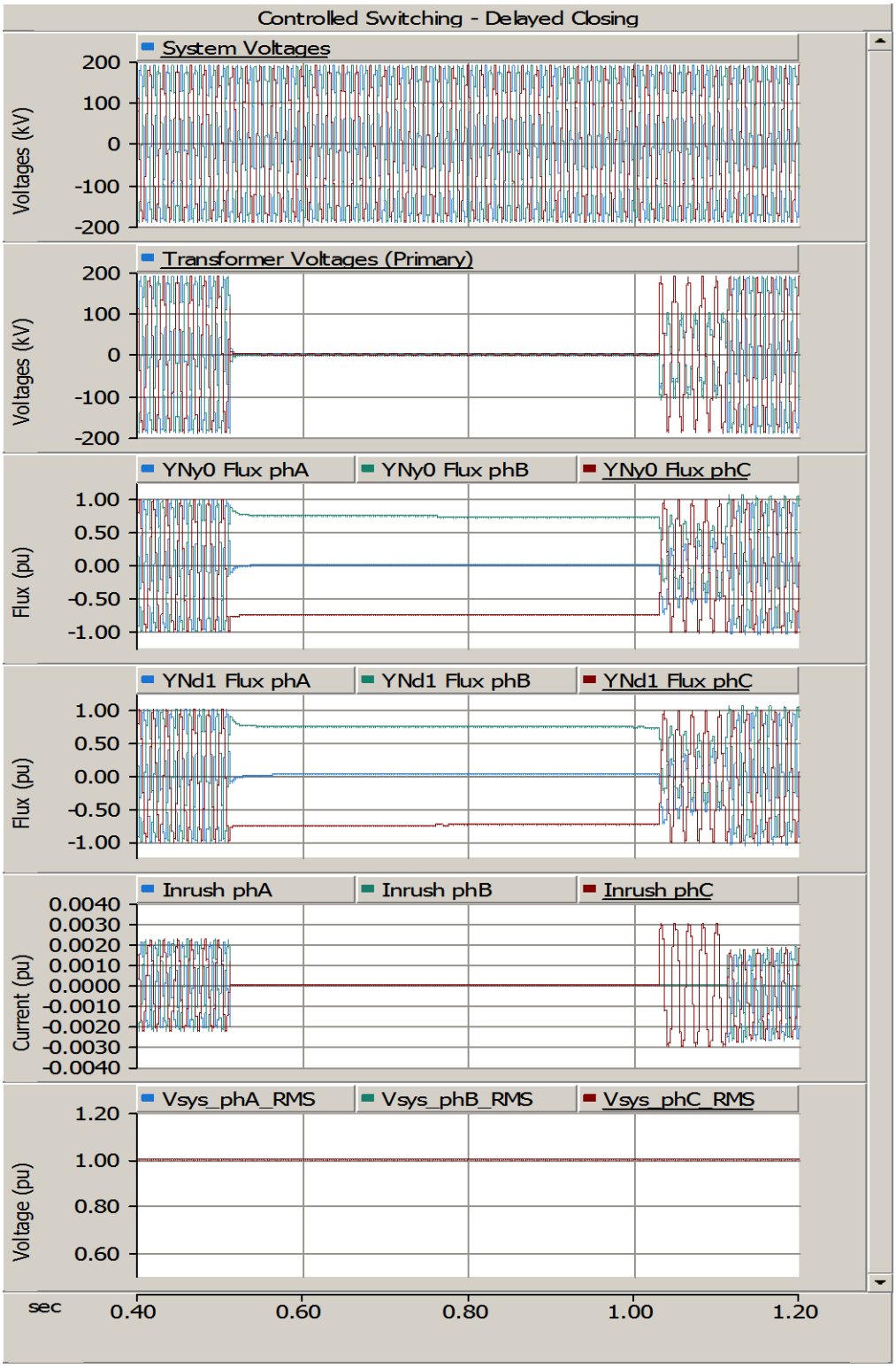

Figure B.2 Inrush currents of five-limb converter transformer pair (controlled switching with 4.5 cycle delayed closing strategy)

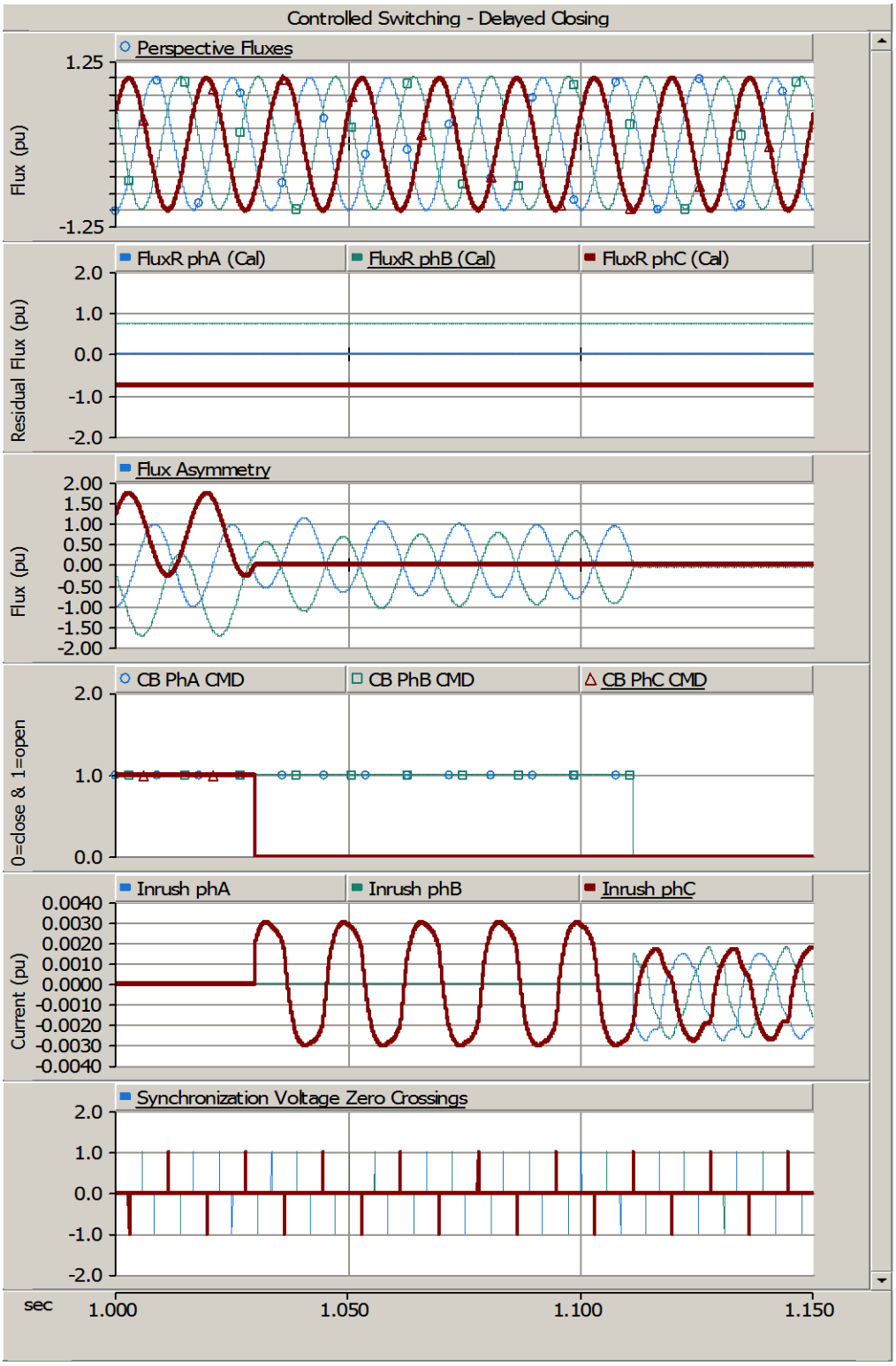

Figure B.3 Transformer core fluxes and inrush currents
(controlled switching with 4.5 cycle delayed closing strategy)

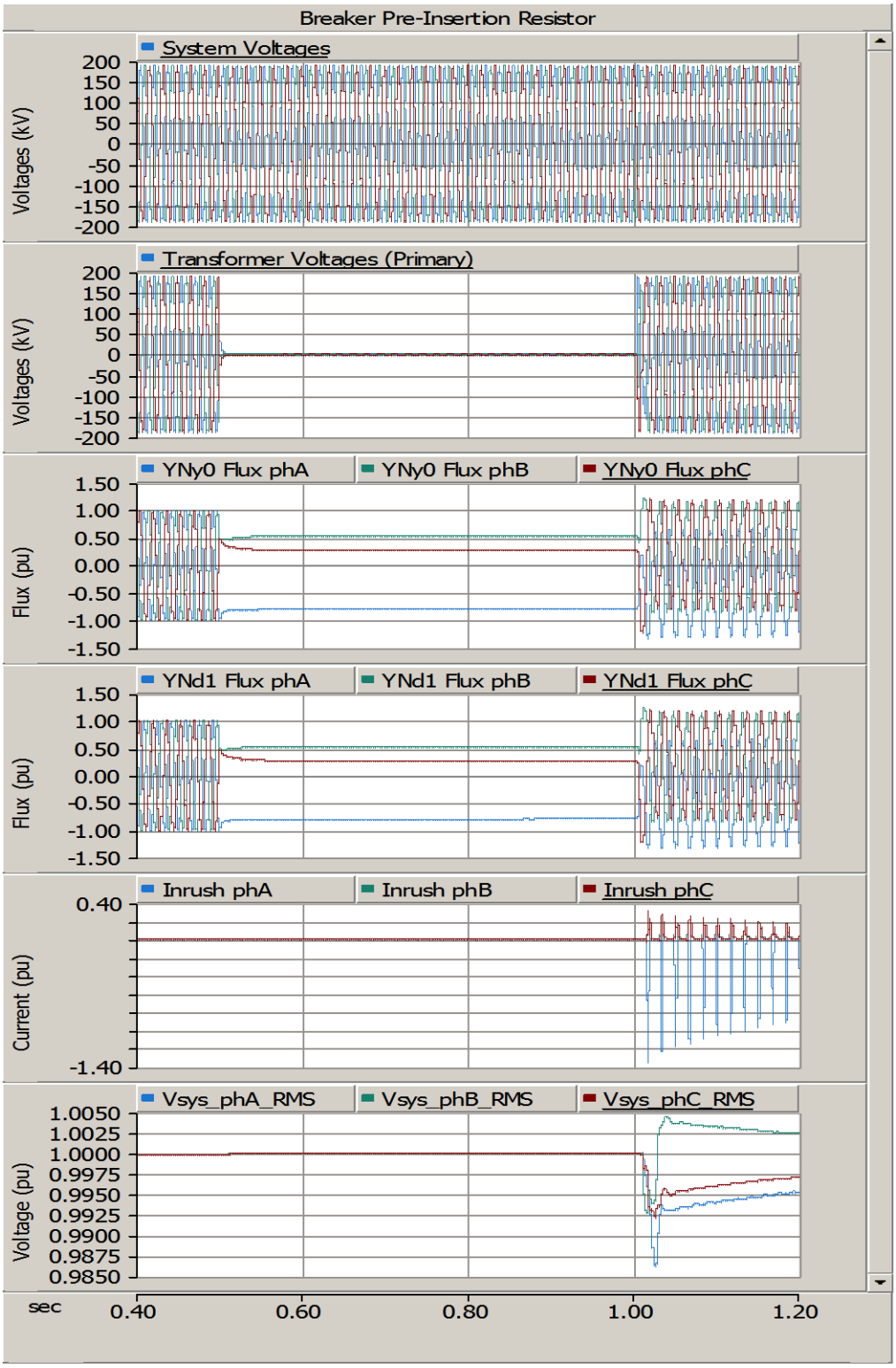

Figure B.4 Inrush currents of five-limb converter transformer pair

(breaker pre-insertion resistor with 400 ohms and 10ms)

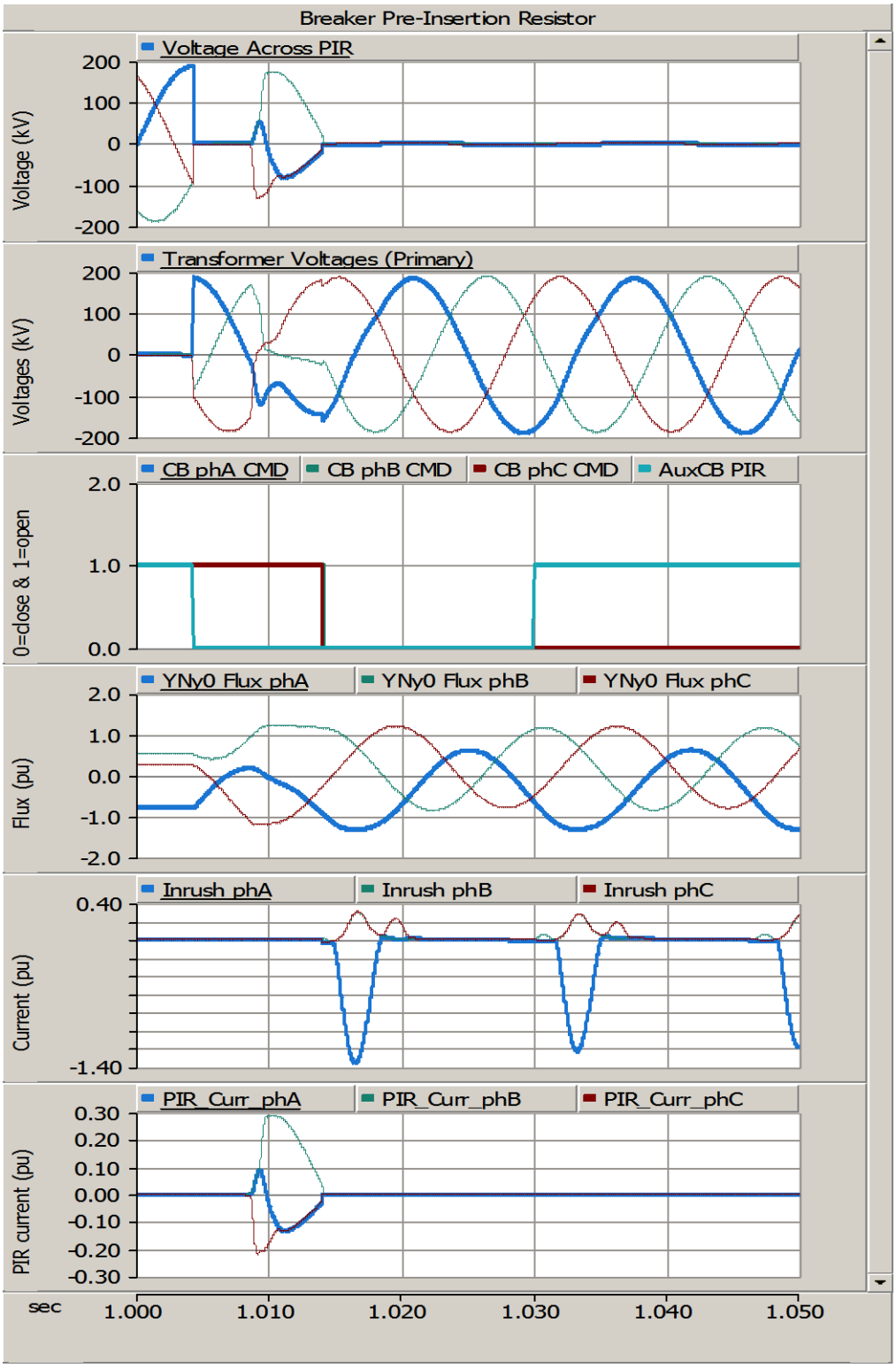

Figure B.5 PIR and transformer voltages, core fluxes and inrush currents (breaker pre-insertion resistor with 400 ohms and 10ms)

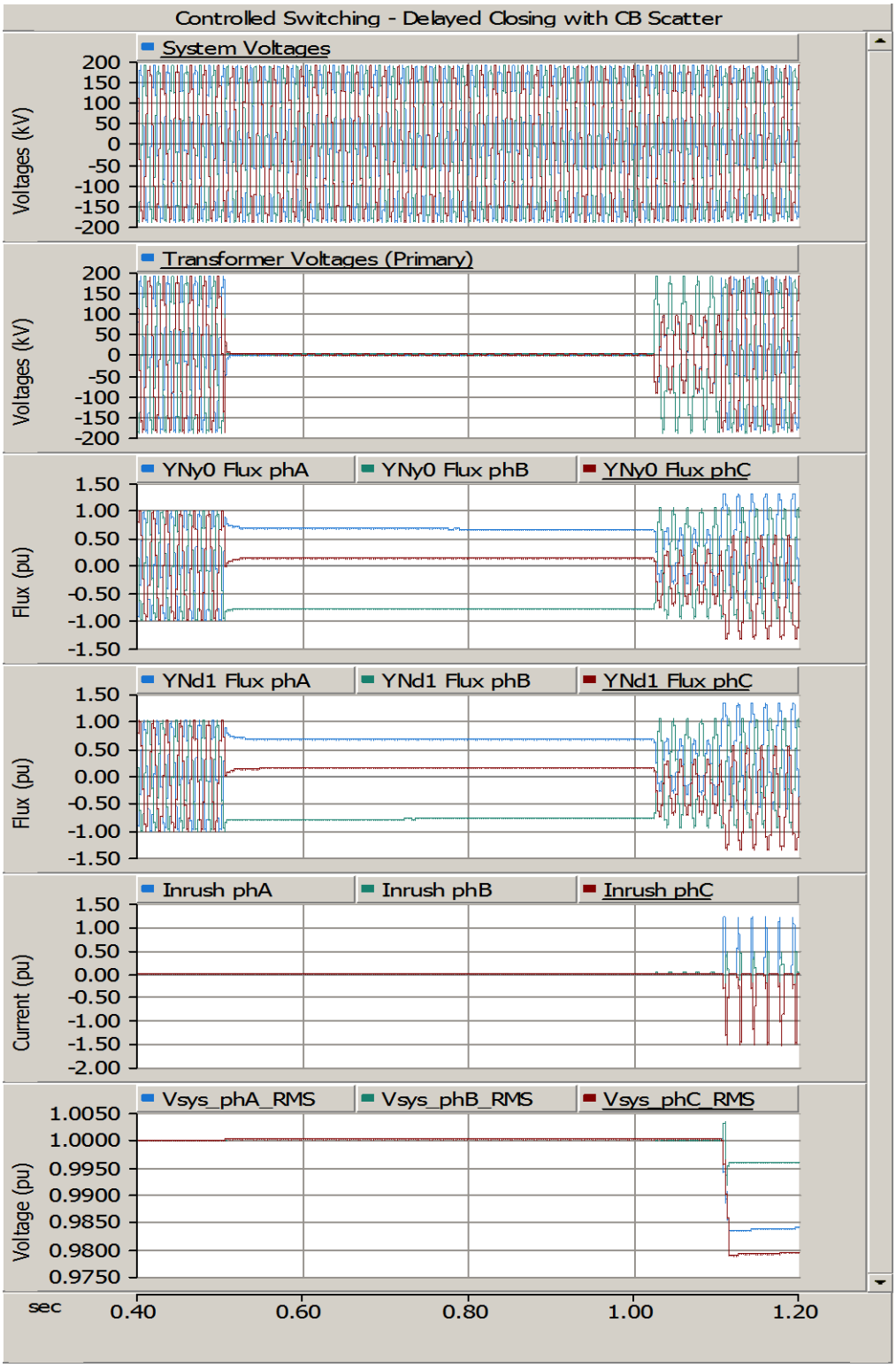

Figure B.6 Inrush currents of five-limb converter transformer pair

(controlled switching with 4.5 cycle delayed closing strategy and breaker scatter)

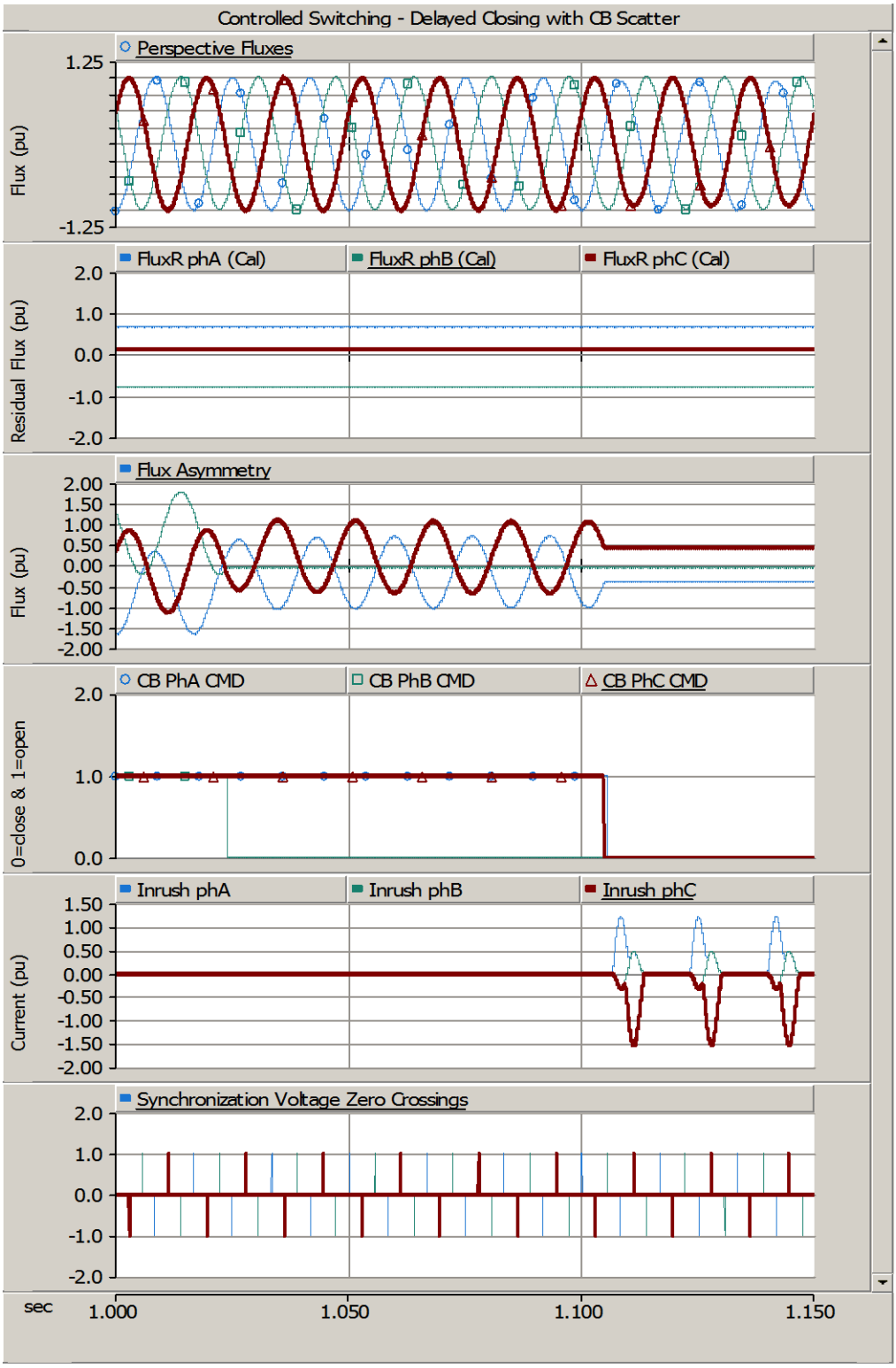

Figure B.7 Transformer core fluxes and inrush currents

(controlled switching with 4.5 cycle delayed closing strategy and breaker scatter)

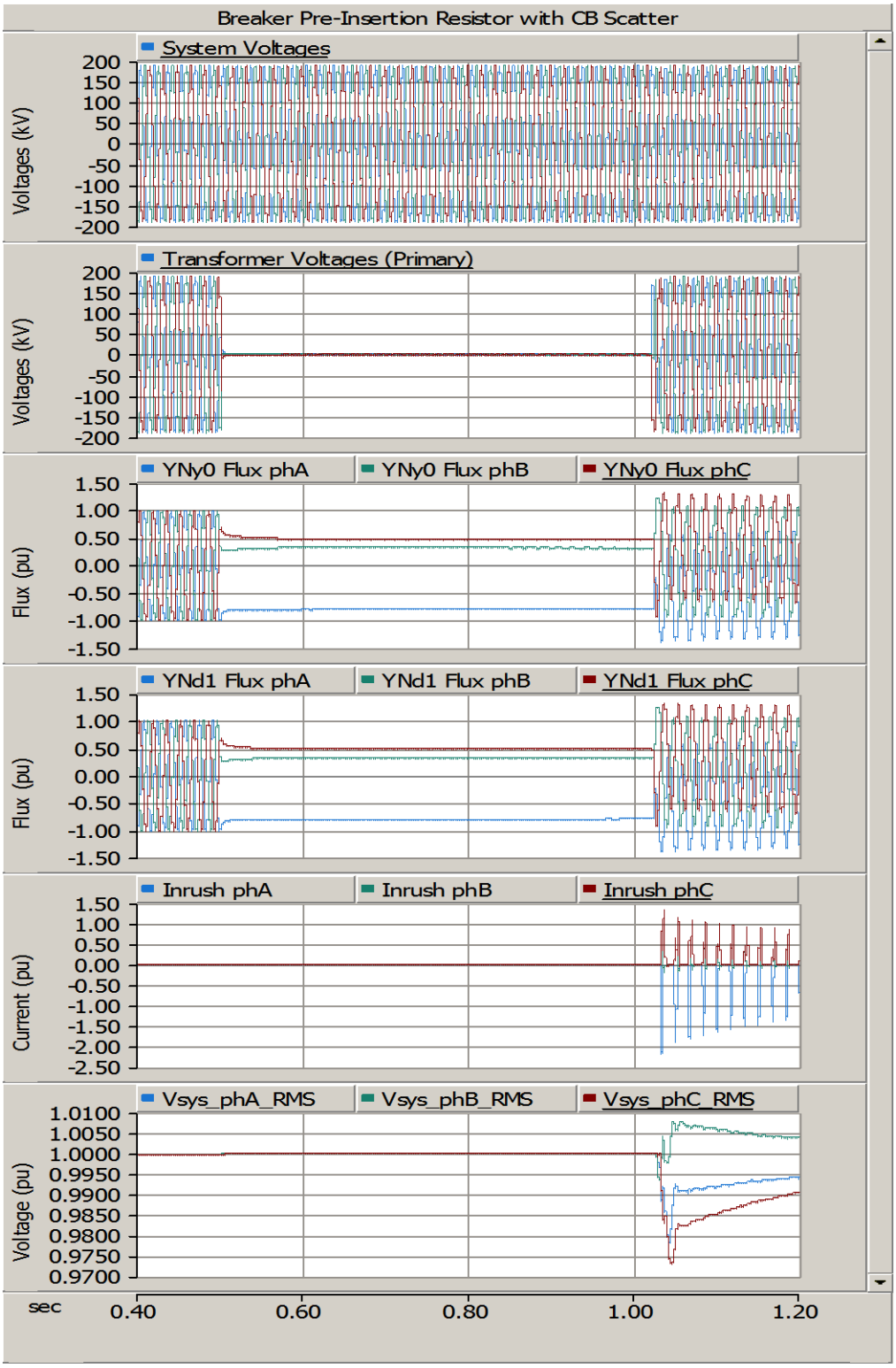

Figure B.8 Inrush currents of five-limb converter transformer pair

(breaker pre-insertion resistor with 400 ohms and 10ms with breaker scatter)

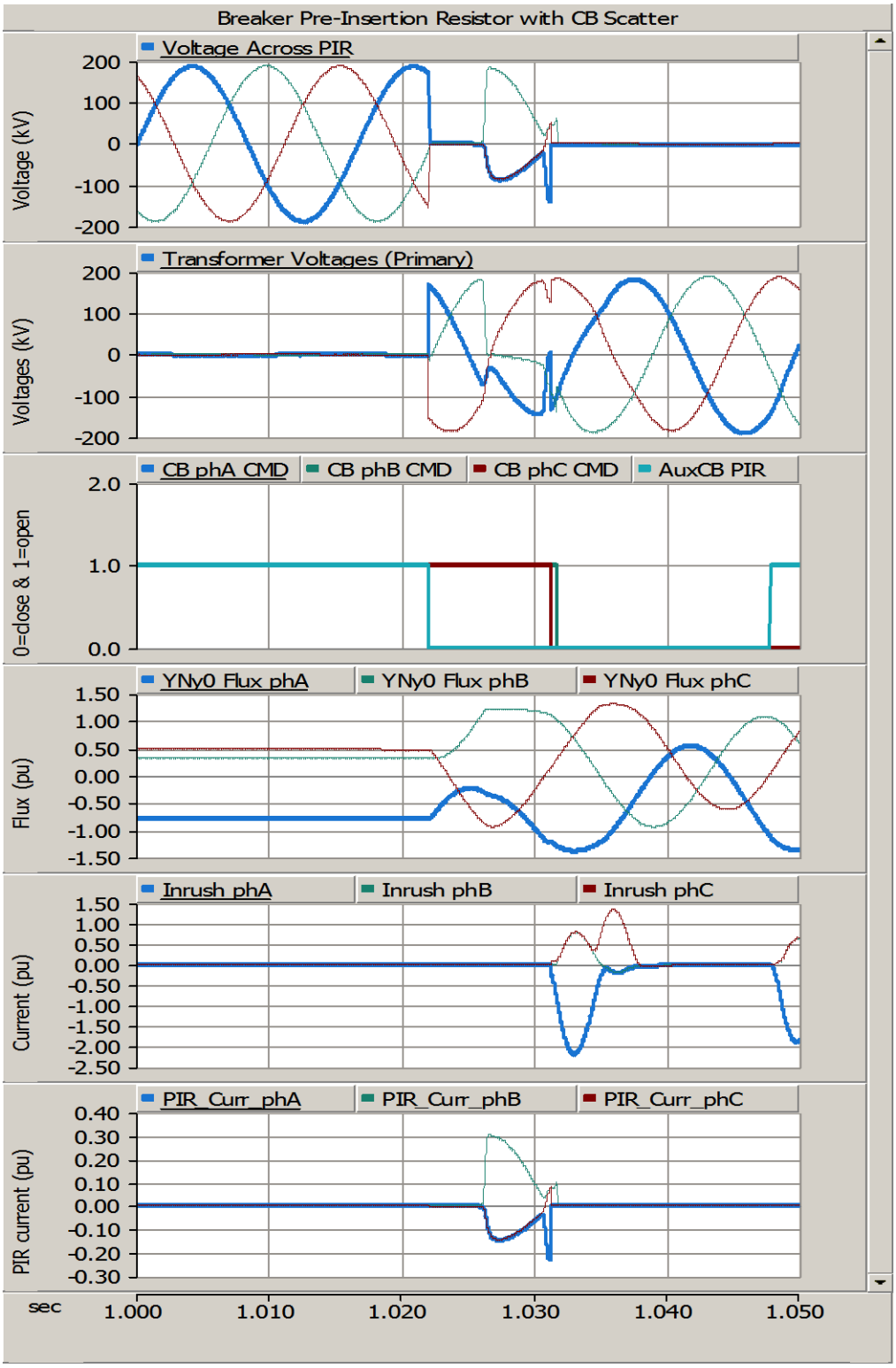

Figure B.9 PIR and transformer voltages, core fluxes and inrush currents (breaker pre-insertion resistor with 400 ohms and 10ms with breaker scatter)

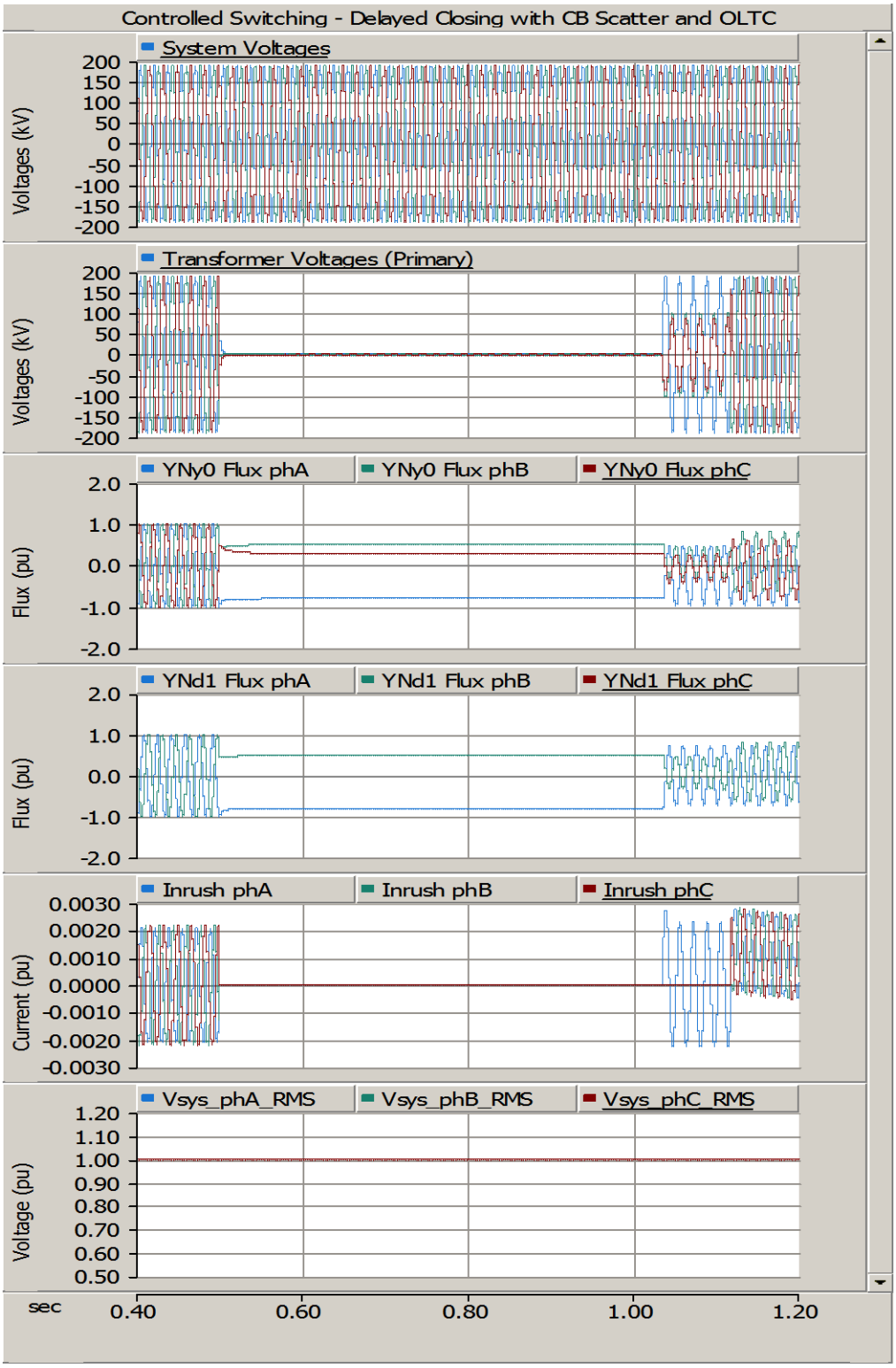

Figure B.10 Inrush currents of five-limb converter transformer pair

(controlled switching with 4.5 cycle delayed closing and breaker scatter & OLTC)

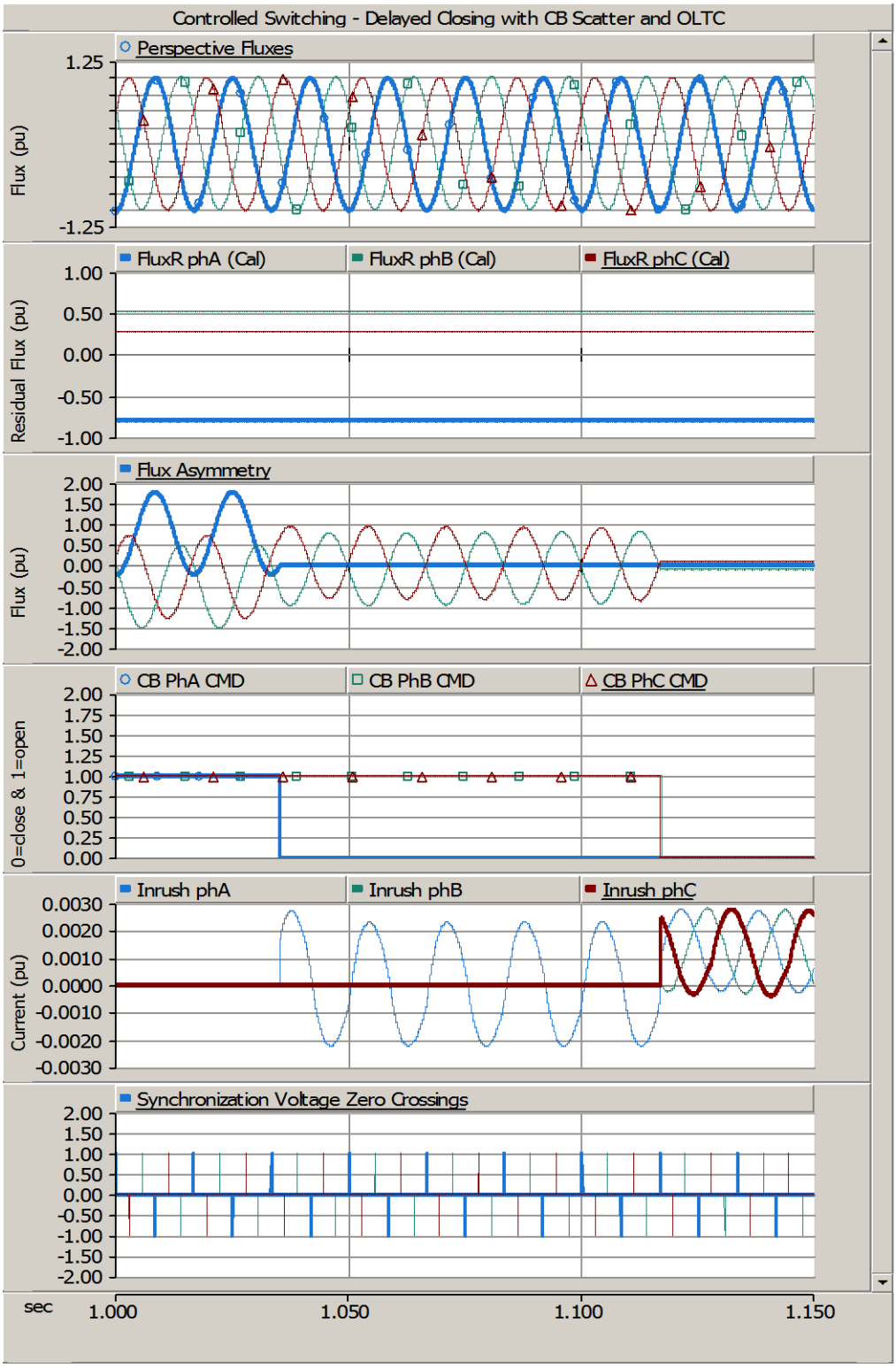

Figure B.11 Transformer core fluxes and inrush currents

(controlled switching with 4.5 cycle delayed closing and breaker scatter & OLTC)

References

[1] U.S. Department of Energy, "Large power transformers and the U.S. electric grid report update (April 2014)," April 2014. [Online]. Available: https://energy.gov/oe/downloads/large-power-transformers-and-us-electric-grid-report-update-april-2014. [Accessed 1 March 2017].

[2] U.S. Department of Energy, "Assessment of large power transformer risk mitigation strategies," October 2016. [Online]. Available: https://energy.gov/epsa/downloads/assessment-large-power-transformer-risk-mitigation-strategies. [Accessed 1 March 2017].

[3] J. Peng, "Assessment of transformer energisation transients and their impacts on power systems - PhD Thesis," University of Manchester, Manchester, 2013.

[4] C. V. Thio, J. B. Davies, and K. L. Kent, "Commutation failures in HVDC transmission systems," *IEEE Transactions on Power Delivery*, vol. 11, no. 2, pp. 946-958, 1996.

[5] CIGRE Working Group C4. 307, "Transformer energization in power systems: a study guide," CIGRE, 2014.

[6] S. V. Kulkarni, and S. A. Khaparde, Transformer engineering: design, technology, and diagnostics, New York: CRC Press, 2013.

[7] CIGRE W.G. A3.07, "Controlled switching of HVAC circuit breakers – guidance for future applications including unloaded transformer switching, load and fault interrupting and circuit breaker uprating," CIGRE Working Group A3.07, Paris, 2004.

[8] J. H. Brunke, and J. Frohlich, "Elimination of transformer inrush currents by controlled switching – part I: theoretical considerations," *IEEE Transactions on Power Delivery*, vol. 16, no. 2, pp. 276-280, 2001.

[9] J. Hu, B. Bisewski, D. Maki and M. B. Marz, "Mitigation of voltage drop using pre-insertion resistor during large transformer energization in weak system: simulation and field verification," in *IPST international conference on power system transients*, Delft, 2011.

[10] R. Yacamini, and A. Abu-Nasser, "Transformer inrush currents and their associated overvoltages in HVDC schemes," *IEEE proceeding C - generation, transmission and distribution*, vol. 133, no. 6, pp. 353-358, 1986.

[11] B. Kasztenny, and A. Kulidjian, "An improved transformer inrush restraint algorithm increases security while maintaining fault response performance," in *53rd Annual Conference for Protective Relay Engineers*, College Station, Texas, 2000.

[12] A. Wiszniewski, W. Rebizant, D. Bejmert, and L. Schiel, "Ultrasaturation phenomenon in power transformers - myths and reality," *IEEE Transactions on Power Delivery*, vol. 23, no. 3, pp. 1327-1334, 2008.

[13] S. Hodder, B. Kasztenny, N. Fischer, and Y. Xia, "Low second-harmonic content in transformer inrush current - analysis and practical solutions for protection security,"

in *67th Annual Conference for Protective Relay Engineers*, College Station, Texas, 2014.

[14] M. Steurer, and K. Frohlich, "The impact of inrush currents on the mechanical stress of high voltage power transformer coils," *IEEE Transaction on Power Delivery*, vol. 17, no. 1, pp. 155-160, 2002.

[15] J. Faiz, B. M. Ebrahimi, and T. Noori, "Three- and two-dimensional finite-element computation of inrush current and short-circuit electromagnetic forces on windings of a three-phase core-type power transformer," *IEEE Transaction on Magnetics*, vol. 44, no. 5, pp. 590-597, 2008.

[16] C. V. Thio, J. R. McNichol, W. M. McDermid, D. Povh, and W. Schultz, "Switching overvoltages on the Nelson river HVDC system - studies, experience and field tests," in *IEEE Conference on Overvoltages and Compensation on Integrated AC-DC Systems*, Winnipeg, 1980.

[17] CIGRE W.G. A3.07, "Controlled switching of HVAC circuit breakers – benefits & economic aspects," CIGRE Working Group A3.07, Paris, 2004.

[18] J. Hu, B. Bisewski, R. Sherry, M. Dalzell, M. Zavahir, and C. Bartzsch, "Converter transformer inrush control using hybrid pre-insertion resistors and point-on-wave switching in the New Zealand HVDC system," in *CIGRE*, Paris, 2016.

[19] H. S. Bronzeado, and J. C. D. Oliveira, "The influence of tap position on the magnitude of transformer inrush current," in *International Conference on Power Systems Transients (IPST)*, Budapest, Hungary, 1999.

[20] W. Chandrasena, D. Jacobson, P. Wang, "Controlled switching of a 1200 MVA transformer in Manitoba," *IEEE Transactions on Power Delivery*, vol. 31, no. 5, pp. 2390-2400, 2016.

[21] R. Nordin, A. Holm, and P. Norberg, "Ten years of service experience with controlled circuit breaker switching in the Swedish regional network," in *CIGRE Paris*, Paris, 2002.

[22] P. C. Fernandez, P. C. V. Esmeraldo, J. A. Filho, and C. R. Zani, "Use of controlled switching systems in power system to mitigate switching transients. Trends and benefits – Brazilian experience," in *CIGRE Paris*, Paris, 2002.

[23] A. Mercier, S. D. Carufel, and P. Taillefer, "Long-term reliability of controlled switching systems: observations from two decades of development and experience," in *CIGRE Paris*, Paris, 2014.

[24] E. Portales, Y. Filion, and A. Mercier, "Transformer-controlled switching taking into account residual flux – modelling transformers for realistic results in system studies," in *CIGRE Paris*, Paris, 2011.

[25] H. S. Bronzeado, E. Saraiva, M. L. R. Chaves, and J. C. D. Oliveira, "A comparative investigation on three-phase transformers modeling with and without magnetic coupling between phases," in *IEEE Transmission and distribution conference and exposition Latin America*, Bogota, 2008.

[26] N. Chiesa, "Power transformer modeling for inrush current calculation," Ph. D. dissertation, NTNU, Norwegian University of Science and Technology, Norwegian, 2010.

[27] N. Chiesa, B. A. Mork, and H. K. Hoidalen, "Transformer model for inrush current calculations: simulations, measurements and sensitivity analysis," *IEEE Transaction on Power Delivery*, vol. 25, no. 4, pp. 2599-2609, 2010.

[28] X. Wang, D. W. P. Thomas, M. Summer, J. Paul, and S. H. L. Cabral, "Characteristics of Jiles-Atherton model parameters and their application to transformer inrush

current simulation," *IEEE Transaction on Magnetics,* vol. 44, no. 3, pp. 340-345, 2008.

[29] J. L. Ribas, E. M. Loureco, J. Leite, and N. Batistela, "Modeling ferroresonance phenomena with a flux-current Jiles-Atherton hysteresis approach," *IEEE Transactions on Magnetics,* vol. 49, no. 5, pp. 1797-1800, 2013.

[30] A. Rezaei-Zare, M. Sanaye-Rasand, H. Mohseni, S. Farhangi, and R. Iravani, "Analysis of ferroresonance modes in power transformers using Preisach-type hysteretic magnetizing inductance," *IEEE Transactions on Power Delivery,* vol. 22, no. 2, pp. 919-929, 2007.

[31] W. Chandrasena, P. G. McLaren, U. D. Annakkage, and R. P. Jayasinghe, "An improved low-frequency transformer model for use in GIC studies," *IEEE Transactions on Power Delivery,* vol. 19, no. 2, pp. 643-651, 2004.

[32] F. Liorzou, B. Phelps, and D. L. Atherton, "Macroscopic models of magnetization," *IEEE Transactions on Magnetics,* vol. 36, no. 2, pp. 419-428, 2000.

[33] F. D. Leon, and A. Semlyen, "A simple representation of dynamic hysteresis losses in power transformers," *IEEE Transactions on Power Delivery,* vol. 19, no. 2, pp. 315-321, 1995.

[34] D. C. Jiles and D. L. Atherton, "Ferromagnetic hysteresis," *IEEE Transactions on Magnetics,* vol. 19, no. 5, pp. 2183-2185, 1983.

[35] D. C. Jiles, and D. L. Atherton, "Theory of ferromagnetic hysteresis," *Journal Magazine of Magnetics Materials,* vol. 61, no. 1, pp. 48-60, 1986.

[36] D. A. Philips, L. R. Dupre, and J. A. Melkebeek, "Comparison of Jiles and Preisach hysteresis models in magnetodynamics," *IEEE Transactions on Magnetics,* vol. 31, no. 6, pp. 3551-3553, 1995.

[37] A. P. S. Baghel, K. Chwastek, and S. V. Kulkarni, "Modelling of minor hysteresis loops in rolling and transverse directions of Grain-Oriented laminations," *IET Electric Power Application,* vol. 9, no. 4, pp. 344-348, 2015.

[38] R. A. Naghizadeh, B. Vahidi, and S. H. Hosseinian, "Modelling of inrush current in transformers using inverse Jiles-Atherton hysteresis model with a neuro-shuffled frog-leaping algorithm approach," *IET Electric Power Application,* vol. 6, no. 9, pp. 727-734, 2012.

[39] K. Chwastek, and J. Szczyglowski, "Estimation methods for the Jiles-Atherton model parameters - a review," *Przeglad Elektrotechniczny,* vol. 84, no. 12, pp. 145-148, 2008.

[40] D. C. Jiles, and J. B. Thoeike, "Theory of ferromagnetic hysteresis: determination of model parameters from experimental hysteresis loops," *IEEE Transactions on Magnetics,* vol. 25, no. 5, pp. 3928-3930, 1989.

[41] D. C. Jiles and D. L. Atherton, "Numerical determination of hysteresis parameters for the modeling of magnetic properties using the theory of ferromagnetic hysteresis," *IEEE Transactions on Magnetics,* vol. 28, no. 1, pp. 27-35, 1992.

[42] J. H. B. Deane, "Modeling the dynamics of nonlinear inductor circuits," *IEEE Transactions on Magnetics,* vol. 30, no. 5, pp. 2795-2801, 1994.

[43] U. D. Annakkage, P. G. McLaren, E. Dirks, R. P. Jayasinghe, and A. D. Parker, "A current transformer model based on the Jiles-Atherton theory of ferromagnetic hysteresis," *IEEE Transactions on Power Delivery,* vol. 15, no. 1, pp. 57-61, 2000.

[44] J. Izydorczyk, "A new algorithm for extraction of parameters of Jiles and Atherton hysteresis model," *IEEE Transactions on Magnetics,* vol. 42, no. 10, pp. 3132-3134, 2006.

[45] R. Marion, R. Scorretti, R. Siauve, M. A. Raulet, and L. Krahenbuhl, "Identification of Jiles-Atherton model parameters using Particle Swarm Optimization," *IEEE Transactions on Magnetics,* vol. 44, no. 6, pp. 894-897, 2008.

[46] M. Lambert, "Transformer modeling for low- and mid-frequency electromagnetic transients simulation," Ph. D. dissertation, University of Montreal, Montreal, 2014.

[47] S. A. Mousavi, "Electromagnetic modelling of power transformers for study and mitigation of effects of GICs," Ph. D. dissertation, Royal Institute of Technology (KTH), Sweden, 2015.

[48] W. G. Enright, "Transformer models for electromagnetic transient studies with particular reference to HVdc transmission," Electrical and Electronic Engineering University of Canterbury, Christchurch, 1996.

[49] W. Chandrasena, "Development of an improved low frequency transformer model for use in GIC studies," Ph.D dissertation, Electrical and Computer Engineering, University of Manitoba, Winnipeg, 2003.

[50] E. Colin Cherry, "The duality between interlinked electric and magnetic circuits and the formation of transformer equivalent circuits," *Physical Society,* vol. 16, no. 2, pp. 101-111, 1949.

[51] B. A. Mork, F. Gonzalez, D. Ishchenko, D. L. Stuehm, and J. Mitra, "Hybrid transformer for transient simulation - part I: development and parameters," *IEEE Transactions on Power Delivery,* vol. 22, no. 1, pp. 248 - 255, 2007.

[52] B. A. Mork, F. Gonzalez, D. Ishchenko, D. L. Stuehm, and J. Mitra, "Hybrid transformer model for transient simulation - part II: laboratory measurements and benchmarking," *IEEE Transactions on Power Delivery,* vol. 22, no. 1, pp. 256 - 262, 2007.

[53] J. P. A. Bastos and N. Sadowski, Magnetic Materials and 3D Finite Element Modeling, New York: CRC Press, 2013.

[54] D. Ribbenfjard, "Electromagnetic transformer modelling including the ferromagnetic core - PhD Thesis," Kungliga Tekniska Hogskolan (KTH) Electrical Engineering, Stockholm, 2010.

[55] G. Bertotti, Hysteresis in magnetism: for physicists, materials scientists, and engineers 1st ed, San Diego: Academic Press, 1998.

[56] D. C. Jiles, Introduction to magnetism and magnetic materials, New York: Chapman & Hall, 1991.

[57] P. R. Wilson, "Modelling and simulation of magnetic components in electric circuits - PhD Thesis," University of Southampton, Electrical Engineering, Southampton, 2001.

[58] R. Venkataraman, "Modeling and adaptive control of magnetostrictive actuators," Ph.D dissertation CDCSS, University of Maryland, Baltimore, 1999.

[59] K. Chwastek, and J. Szczyglowski, "An alternative method to estimate the parameters of Jiles-Atherton model," *Journal of Magazine Magnetics Material,* vol. 314, no. 1, pp. 47-51, 2007.

[60] J. V. Leite, S. L. Avila, N. J. Batistela, W. P. Carpes, N. Sadowski, P. Kuo-Peng, and J. P. A. Bastos, "Real coded genetic algorithm for Jiles-Atherton model parameters identification," *IEEE Transactions on Magnetics,* vol. 40, no. 2, pp. 888-891, 2004.

[61] C. D. Graham, Jr., "Physical origin of losses in conducting ferromagnetic materials," *Journal of Applied Physics,* vol. 53, no. 11, pp. 8276-8280, 1982.

[62] J. W. Shilling and G. L. Houze, Jr., "Magnetic properties and domain structure in grain oriented 3% Si-Fe," *IEEE Transactions on Magnetics,* vol. 10, no. 2, pp. 195-223, 1974.

[63] G. Bertotti, "General properties of power losses in soft ferromagnetic materials," *IEEE Transactions on Magnetics*, vol. 24, no. 1, pp. 621-630, 1988.

[64] J. Kennedy and R. Eberhart, "Particle swarm optimization," in *IEEE International Conference on Neural Networks (ICNN95)*, Perth, 1995.

[65] J. Kennedy and R. Eberhart, "A new optimizer using particle swarm theory," in *Micro Machine and Human Science*, Japan, 1995.

[66] L. D. S. Coelho, F. A. Guerra, and J. V. Leite, "Multiobjective exponential particle swarm optimization approach applied to hysteresis parameters estimation," *IEEE Transactions on of Magnetics,* vol. 48, no. 2, pp. 283-286, 2012.

[67] AK Steel Corp., "TRAN-COR H grain oriented electrical steels product data bulletin," 7 June 2013. [Online]. Available: http://www.aksteel.com/pdf/markets_products/electrical/AK%20TRAN-COR%C2%AE%20H%20PDB%2020130607.pdf. [Accessed 10 Jan 2016].

[68] J. Doke, "GRABIT – extract data off image files, MATLAB Central File Exchange," 1 September 2016. [Online]. Available: https://www.mathworks.com/matlabcentral/fileexchange/7173-grabit. [Accessed 2 January 2016].

[69] G. Shirkoohi, "Dependence of magnetization near saturation on alloying content in ferromagnetic steel," *IEEE Transactions on Of Magnetics*, vol. 51, no. 7, p. 2002010, 2015.

[70] A. Kaur and M. Kaur, "A review of parameters for improving the performance of particle swarm optimization," *International Journal of Hybrid Information Technology*, vol. 8, no. 4, pp. 7-14, 2015.

[71] M. Clerc, and J. Kennedy, "The particle swarm - explosion, stability, and convergence in a multidimensional complex space," *IEEE Transactions on Evolutionary Computation*, vol. 6, no. 1, pp. 58-73, 2002.

[72] J. J. Liang, and P. N. Suganthan, "Dynamic multi-swarm particle swarm optimizer with local search," *IEEE Congress on Evolutionary Computation*, vol. 1, no. 1, pp. 522-528, 2005.

[73] Y. Shi, and R. Eberhart, "A modified particle swarm optimizer," in *IEEE ICEC*, Anchorage, 1998.

[74] F. V. D. Bergh, and A. P. Engelbrecht, "A study of particle swarm optimization particle trajectories," *Information Science*, vol. 176, no. 8, pp. 927-971, 2006.

[75] J. C. Bansal, P. K. S. M. Saraswat, A. Verma, S. S. Jadon, and A. Abraham, "Inertia weight strategies in particle swarm optimization," in *IEEE NBIC*, Spain, 2011.

[76] H. L. Lu, X. S. Wen, L. Lan, Y. Z. An, and X. P. Li, "A self-adaptive genetic algorithm to estimate JA model parameters considering minor loops," *Journal of Magnetism and Magnetic Materials*, vol. 374, no. 1, pp. 502-507, 2015.

[77] D. Lederer, H. Igarashi, A. Kost and T. Honma, "On the parameter identification and application of the Jiles-Atherton Hysteresis model for numerical modelling of measured characteristics," *IEEE Transactions on Magnetics*, vol. 35, no. 3, pp. 1211-1214, 1999.

[78] P. R. Wilson, J. N. Ross, and A. D. Brown, "Optimizing the Jiles-Atherton model of hysteresis by a genetic algorithm," *IEEE Transactions on Magnetics,* vol. 37, no. 2, pp. 989-993, 2001.

[79] Z. Wlodarski, "The Jiles-Atherton model with variable pinning parameter," *IEEE Transactions on Of Magnetics,* vol. 39, no. 4, pp. 1990-1992, 2003.

[80] M. Toman, G. Stumberger, and D. Dolinar, "Parameter identification of the Jiles-Atherton hysteresis model using differential evolution," *IEEE Transactions on Of Magnetics,* vol. 44, no. 6, pp. 1098-1101, 2008.

[81] P. R. Wilson, and J. N. Ross, "Definition and application of magnetic material metrics in modeling and optimization," *IEEE Transactions on Magnetics,* vol. 37, no. 5, pp. 3774-3780, 2001.

[82] L. Prikler, G. Banfai, G. Ban, and P. Becker, "Reducing the magnetizing inrush current by means of controlled energization and de-energization of large power transformers," in *IPST*, New Orleans, 2003.

[83] HVDC Research Centre, "Magnetic electric equivalent circuit (MEEC) transformer model help description," unpublished by HVDC Research Centre, Winnipeg, 2014.

[84] S. D. Cho, "Parameter estimation for transformer modeling," Michigan Technological University, Michigan, 2002.

[85] R. D. Garzon, High voltage circuit breakers: design and applications, New York: Marcel Dekker, 2002.

[86] J. H. Brunke, and J. Frohlich, "Elimination of transformer inrush currents by controlled switching – part II: application and performance considerations," *IEEE Transactions on Power Delivery,* vol. 16, no. 2, pp. 276-280, 2001.

[87] J. A. Martinez, R. Natarajan, and E. Camm, "Comparison of statistical switching results using Gaussian, uniform and systematic switching approaches," in *Power Engineering Society Summer Meeting*, USA, 2000.

[88] N. Mabunda, P. Bokoro, and D. Nicolae, "Statistical analysis of operating times of high voltage SF6 circuit breakers," in *IEEE 16th International Conference on Environment and Electrical Engineering (EEEIC)*, Florence, Italy, 2016.

[89] D. C. Jiles, "Frequency dependence of hysteresis curves in conducting magnetic materials," *Journal of Applied Physics*, vol. 76, no. 10, pp. 5849-5855, 1994.